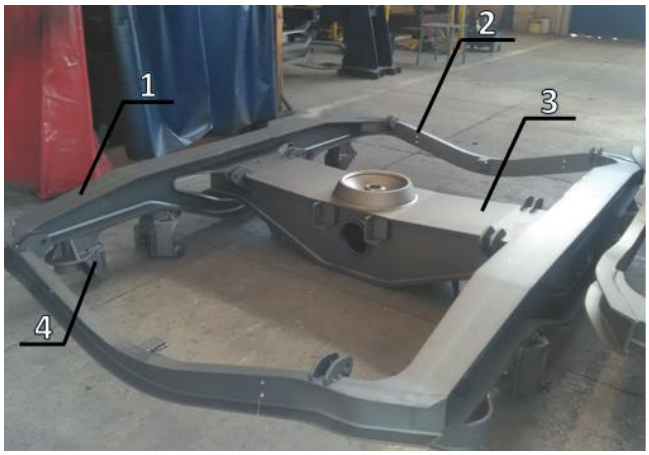
International journal
for science, technics and
innovations for the industry

MACHINES TECHNOLOGIES MATERIALS

YEAR XIII Issue 11 / 2019 ISSN PRINT 1313-0226
ISSN WEB 1314-507X



Published by
Scientific technical
Union of Mechanical Engineering

MACHINES. TECHNOLOGIES. MATERIALS

INTERNATIONAL SCIENTIFIC JOURNAL

PUBLISHER

SCIENTIFIC TECHNICAL UNION OF MECHANICAL ENGINEERING "INDUSTRY 4.0"

108, Rakovski Str., 1000 Sofia, Bulgaria
tel. (+359 2) 987 72 90,
tel./fax (+359 2) 986 22 40,
office@stumejournals.com
www.stumejournals.com

ISSN PRINT 1313-0226, ISSN WEB 1314-507X, YEAR XIII, ISSUE 11 / 2019

EDITOR-IN-CHIEF

Prof. D.Sc. DHC Georgi Popov,
President of Bulgarian Scientific and Technical Union of Mechanical Engineering

EDITORIAL BOARD

MEMBERS	SCIENTIFIC COMPETENCE
Prof. Dimitar Damyanov	Automatisation of production
Prof. Dimitar Karaivanov	Mechanics of machines
Prof. Dimitar Stavrev	Technologies and materials
Prof. Dimitar Yonchev	National and industrial security
Prof. Galina Nikolcheva	Machines tools and technologies
Prof. Hristo Shehtov	Automatisation of production
Prof. Idilija Bachkova	Automatisation of production
Prof. Ivan Kralov	Mechanics of machines
Prof. Ivan Parshorov	Technologies and materials
Prof. Ivan Yanchev	Machines and technologies
Prof. Ivo Malakov	Automatisation of production
Prof. Kiril Angelov	Industrial Management
Prof. Lilo Kunchev	Transport Equipment and Technology
Prof. Lubomir Dimitrov	Machines and technologies
Prof. Miho Mihov	Agricultural machinery
Prof. Miroslav Denchev	Ergonomics and design
Prof. Mladen Velev	Economics and Marketing
Prof. Nikolay Diulgerov	Technologies and materials
Prof. Ognyan Andreev	Production management
Prof. Petar Kolev	Transport Equipment and Technology
Prof. Roman Zahariev	Robotics
Prof. Sasho Guergov	Robotic systems and technology
Prof. Tsanka Dikova	Technologies and materials
Prof. Vitan Galabov	Mechanics of machines

MACHINES. TECHNOLOGIES. MATERIALS

INTERNATIONAL SCIENTIFIC JOURNAL

ISSN PRINT 1313-0226, ISSN WEB 1314-507X, YEAR XIII, ISSUE 12 / 2019

EDITORIAL BOARD FOREIGN MEMBERS			
Prof. Adel Mahmoud	IQ	Prof. Marian Tolnay	SK
Prof. Ahmet Ertas	TR	Prof. Mark Easton	AU
Prof. Andonaq Londo	AL	Prof. Mart Tamre	EE
Prof. Andrei Firsov	RU	Prof. Maryam Ehteshamzade	IR
Prof. Andrzej Golabczak	PL	Prof. Michael Evan Goodsite	DK
Prof. Anita Jansone	LV	Prof. Mihail Aurel Titu	RO
Prof. Aude Billard	CH	Prof. Movlazade Vagif Zahid	AZ
Prof. Bojan Dolšak	SI	Prof. Natasa Naprstkova	CZ
Prof. Christian Marxt	LI	Prof. Oana Dodun	RO
Prof. Dale Carnegie	NZ	Prof. Oleg Sharkov	RU
Prof. Emilia Abadjieva	BG	Prof. Páll Jensson	IS
Prof. Ernest Nazarian	AM	Prof. Patrick Anderson	NL
Prof. Esam Husein	KW	Prof. Paul Heuschling	LU
Prof. Ewa Gunnarsson	SW	Prof. Pavel Kovac	RS
Prof. Filipe Samuel Silva	PT	Prof. Per Skjerpe	NO
Prof. Francisco Martinez Perez	CU	Prof. Péter Korondi	HU
Prof. Franz Haas	AT	Prof. Peter Kostal	SK
Prof. Genadii Bagliuk	UA	Prof. Juan Alberto Montano	MX
Prof. Georg Frey	DE	Prof. Raul Turmanidze	GE
Prof. Gregory Gurevich	IL	Prof. Renato Goulart	BR
Prof. Haydar Odinaev	TJ	Prof. Roumen Petrov	BE
Prof. Hiroyuki Moriyama	JP	Prof. Rubén Darío Vásquez Salazar	CO
Prof. Dr. Ilir Doci	Ko	Prof. Safet Isić	BA
Prof. Iryna Charniak	BY	Prof. Sean Leen	IE
Prof. Ivan Svarc	CZ	Prof. ShI Xiaowei	CN
Prof. Ivica Veza	HR	Prof. Shoirdzan Karimov	UZ
Prof. Jae-Young Kim	KR	Prof. Sreten Savićević	ME
Prof. Jerzy Jedzejewski	PL	Prof. Stefan Dimov	UK
Prof. Jean-Emmanuel Broquin	FR	Prof. Svetlana Gubenko	UA
Prof. Jordi Romeu Garbi	ES	Prof. Sveto Cvetkovski	MK
Prof. Jukka Tuhkuri	FI	Prof. Tamaz Megrelidze	GE
Prof. Katia Vutova	BG	Prof. Tashtanbay Sartov	KG
Prof. Kazimieras Juzėnas	LT	Prof. Teimuraz Kochadze	GE
Prof. Krasimir Marchev	USA	Prof. Thorsten Schmidt	DE
Prof. Krzysztof Rokosz	PL	Prof. Tonci Mikac	HR
Prof. Leon Kukielka	PL	Prof. Vasile Cartofeanu	MD
Prof. Mahmoud El Gammal	EG	Prof. Yasar Pancar	TR
Prof. Manolakos Dimitrios	GR	Prof. Yurij Kuznetsov	UA
Prof. Marat Ibatov	KZ	Prof. Wei Hua Ho	ZA
Prof. Marco Bocciolone	IT	Prof. Wu Kaiming	CN

C O N T E N T S

MACHINES

CHARGING STATIONS FOR ELECTRIC VEHICLES – TECHNICAL FEATURES AND TRENDS
Assoc. Prof. PhD Rachev S. R., Assist. Prof. PhD Koeva D. Y., Assist. Prof. PhD Dimitrov L. D. 474

RESEARCH WORK ABOUT THE TROUBLE-FREE OPERATION OF A ROBOTIC CELL FOR THE WELDING OF THE BOGIE FRAME ON A FREIGHT WAGON
M. Sc. Edrev St., Assos. Prof. Topalova M. PhD 481

IMPROVEMENT OF GROUND PUMPS FOR TRANSPORT OF SLURRY
Doct. student Seitkhanov A., Prof. dr. eng. Povetkin V., Dr. phd Bukayeva A., Prof. dr. eng. Ivanov S. 484

TECHNOLOGIES

KINETIC MODELS OF NICKEL LATERITE ORE LEACHING PROCESS
Petrovski A., Načevski G., Dimitrov A. T., Paunović P. 487

OPTIMIZATION OF CUTTING PARAMETERS FOR MINIMIZING SPECIFIC CUTTING ENERGY AND MAXIMIZING PRODUCTIVITY IN TURNING OF AISI 1045 STEEL
Assis. Prof. Sredanović B. PhD., Asoc. Prof. Čiča Đ. PhD., M.Sc. Tešić S., Asoc. Prof. Kramar D. PhD 491

ENERGY HEAT EXCHANGE IN THE ZONE OF CONTACT OF THE PROBE OF AN ATOMIC FORCE MICROSCOPE WITH THE SURFACE UNDER STUDY
Andriienko O., Ralchenko S., Doctor of Science Bondarenko M., PhD Bondarenko Yu. 495

EXAMPLES OF SOFTWARE CONFIGURATION MANAGEMENT
M.Sc. Ivanova Milka 500

MATERIALS

MICROSTRUCTURE AND MECHANICAL PROPERTIES OF A HYPEREUTECTIC ALLOY AlSi18, MODIFIED BY A NANODIAMOND AND PHOSPHORUS
Assistant Dochev B. eng., Head Assistant Velikov A. PhD, Head Assistant Panov Iv. PhD, Head Assistant Diakova V. PhD, Head Assistant Kuzmanov P. PhD, Associate Professor Manolov V. PhD 504

AN ALLOY FOR ACCUMULATION OF HYDROGEN WITH STRUCTURE OF LAVES PHASE AND BCC SOLID SOLUTION FOR THE NEEDS OF ALTERNATIVE ENERGY
PhD Dekhtyarenko V., PhD Pryadko T., PhD Bondarchuk V., PhD Mogylnyy G., PhD. Khranovskaya E. 507

ON THE EFFECT OF INTERMEDIATE PRESSING OF PREFORMS ON THE FORMATION OF A DEFECT-FREE STRUCTURE OF FINISHED PRODUCTS FROM CARBON FIBER-FILLED POLYTETRAFLUOROETHYLENE
Assoc. Prof. Voropaev V.V. PhD, Assoc. Prof. Skaskevich A.A. PhD, Senior lecturer Lesun A.N., Assoc. Prof. Sarokin V.G., PhD Yankov E. 511

QUALITY MANAGEMENT OF NEW CERAMIC MATERIALS BY USING STATISTICAL EXPERIMENTAL DATA PROCESSING PROGRAMS
Sadenova M. Ph.D., M.Ec. Utegenova M., Anuarbekov T. 511

CHARGING STATIONS FOR ELECTRIC VEHICLES – TECHNICAL FEATURES AND TRENDS

Assoc. Prof. PhD Rachev S. R., Assist. Prof. PhD Koeva D. Y., Assist. Prof. PhD Dimitrov L. D.
Technical University of Gabrovo, Republic of Bulgaria

sratchev@mail.com

Abstract: *One of the prerequisites for achieving the long-term goal of better atmospheric air quality is the transition to a low carbon economy and more sustainable transport through the increased use of electric vehicles. Statistics show that transport generates over 14% of global greenhouse gas emissions and is the main sector in the EU where this indicator is still increasing.*
Electric vehicle technology is constantly evolving and they are gaining in efficiency. Generally, electromobility is about charging, managing and using energy. The success of the automotive industry in the future will be determined by how quickly the development of traction motors and batteries will continue, as well as the charging infrastructure.
In order to ensure the normal operation of electric vehicles, it is necessary to build an adequate infrastructure of charging stations.
The paper deals with the technical features and trends of charging stations for electric vehicles. The results are a summary and assessment of extending the boundaries of electromobility, contributing to a more sustainable future. Relevant conclusions have been done.
KEYWORDS: *ELECTRIC VEHICLES, CHARGING STATIONS, ELECTROMOBILITY*

1. Introduction

In March 2018, the European Parliament approved proposals for new binding targets at European Union (EU) level for a 35% improvement in energy efficiency, a minimum 35% share of final energy from renewable sources and a 12% share from renewable energy sources (RES) in transport by 2030. The energy efficiency target should be met on the basis of estimated energy consumption for 2030 according to the *PRIMES* model. With regard to the new target for the share of renewable energy, Member States should introduce national targets that will allow a maximum deviation of 10% under certain conditions. In 2030, 12% of the energy consumed in transport must be generated by RES. Also, by 2022, 90% of the petrol stations on the trans-European networks should be equipped with high-power charging stations for electric vehicles (EVs). The European Parliament also endorsed the proposal to ensure that consumers producing electricity on their own territory can use it and install storage systems without having to pay any taxes and fees.

Transport is responsible for almost 30% of total EU CO2 emissions, while land transport accounts for 72% of transport emissions, according to European Parliament data. CO2 emissions from passenger transport vary greatly depending on the type of vehicle. Passenger cars are the major pollutant responsible for 60.7% of Europe's total land transport emissions. The problem is largely due to the fact that passenger cars carry a small number of people – an average of 1.7 passengers.

The introduction of mass-market EVs is mainly driven by the need to reduce the high percentage of greenhouse gases emitted by large cities and its impact on climate change. In addition, under good governance, the development of electricity mobility can be one of the key technologies for securing employment and growth for industry. The public benefits of electromobility as a fast-growing industry are beyond creating new jobs and motivating them to think more environmentally and effectively in improving the quality of life.

The environmental benefits of using EVs have been proven, but without using fully RES such as solar and wind, their carbon footprint is to some extent simply displaced by internal combustion engines (ICE) of vehicles to production of fossil fuel electricity. The use of a renewable energy charged EVs guarantees both economical and environmentally friendly transport.

Over the years, current restrictions on the use of ICE vehicles in major cities are likely to increase. The main factor is the low energy efficiency of the ICE – for a 100 km run a vehicle with an ICE consumes 66 kWh at a consumption of 6 liters/100 km. EVs require 15-17 kWh per 100 km (energy cost for generating electricity from power plants is not included here). As with conventional vehicles, the consumption of EVs depends on the technical parameters, the atmospheric and road conditions, and the driving style. *PwC* (*PricewaterhouseCoopers*) predicts that 'between 2025 and 2030, the cost of battery EVs will fall below the cost of ICE cars'. At this stage, the initial price of an EV is higher than the price of a car with an ICE on the same coupe, which is a serious deterrent to its mass demand – potential buyers often only look at the starting price. This is compounded by the unknown at this stage of the operation of EV and the lack of a developed charging infrastructure.

In order to encourage the purchase of EVs, various financial and tax incentives are offered in many countries in Europe, US, Canada and Australia, as well as non-monetary benefits for EV users. Government subsidy on purchase of new EV in Europe (not everywhere in the individual countries) and North America reaches 10 to 30% of its price. In Germany, as of November 1, 2019, the subsidy for the purchase of an EV reached € 6,000 (with a previous subsidy of € 4,000), following an agreement between Chancellor Angela Merkel and the German Automobile Industry Association *VDA*. This applies to EVs with prices up to € 40,000, and for those with prices between € 40,000 and € 60,000, the subsidy is € 5,000. For plug-in hybrids, the subsidy is € 4500 (compared to a previous subsidy of € 3000). The plans are for the subsidy to be given by 2025, with the expectation that between 650 and 700 thousand EVs will be purchased during this period. In Romania, the bonus is more serious – the Government gives € 10,000 when buying an EV, adding another € 1,500 if a car older than 8 years is scrapped.

The eco-norms are becoming more serious, and if they have so far sounded like an abstract recommendation, they will soon have a noticeably strong impact. The reason is that from 2020 in Europe, carmakers should have maximum emissions for their entire range of an average of 95 g/km. If they are exceeded, they will be fined by 2021 depending on the excess and the number of cars sold. Exactly electrification is the step of entering the new order. The road to full electromobility goes through the transient period of the different types of hybrids. From now on, due to the aforementioned draconian measures, almost every new model, if not an EV, would be at least a hybrid.

There are currently 1 billion vehicles in use worldwide. About 165,000 vehicles are produced every day. According to the German Solar Energy and Hydrogen Research Center (*ZSW*), at the beginning of 2019, EVs on the roads around the world are 5.6 million. China and the US are the largest markets, with 2.6 and 1.1 million EV respectively. In China, in terms of sales, EVs are already ahead of gasoline models. According to estimates, by 2020, the number of EVs is expected to reach 10% of annual production worldwide. According to the German government's plan for climate protection by 2030, the number of EVs should increase to 10 million. In any case, this is a very ambitious plan. At least so far as nothing in this world is certain. In Germany, statistics reported at the beginning of 2019 the presence of 420,000 electric cars in the

country (including hybrids), with a total fleet of more than 47 million vehicles. In Sweden – the Government has announced the most ambitious strategy, involving all cars in the country by 2030 to be independent of coal and oil. The Norwegians set a goal in 2040 to have no gasoline and diesel cars on the country's roads. The state-appointed consulting firm *Poyry* claims that there will be about 1.9 million electric cars on the roads in Norway by 2040.

Currently, all automakers are seeing an increasing effort to electrify product lines to reduce emissions across the range.

Governing body of *Toyota Motor Corporation* (global leader in sales) announced in August 2019 that the company had decided to take forward to electromobility and focus primarily on developing electric vehicles for European markets. Currently, half of their sales in the EU come from hybrids. The logic of the Japanese is that once Europeans buy their hybrids, they will quickly reorient themselves to purely electric cars. So *Toyota* will gradually replace its conventional models for Europe with electric ones. *Honda Motor Co.* unveiled news of its electric future in September 2019 – the strategic plan for Europe's *Electric Vision*, which envisages 100% of European brand sales of EVs by 2025. In October 2019, *Volvo Cars* unveiled the *XC40 Recharge*, the company's first all-electric car and the first model of the latest *Recharge* concept for cars. The company's ambition is that 50% of global sales by 2025 be entirely electric cars and the rest are hybrids. *Recharge* will be the all-inclusive name for all electric and hybrid *Volvo* cars. *Volvo*'s strategy is to make a super fast transition to EVs, which means adding a new model of electricity every year from now on for the next few years.

In November 2019, *PSA Groupe* (manufacturer of *Peugeot*, *Citroen* and *Opel*) and Italian carmaker *FIAT - Chrysler* agreed to a $ 48 billion merger. According to *CNN*, the merger will form the third largest automaker in the world and help to distribute the huge costs of developing electric and autonomous cars. The new venture will be able to meet the challenges of vehicle electrification, Internet connectivity and unmanned cars steering.

There are 262 million registered vehicles in the EU in 2018. About 2 million or less than 1% of them are classified as electric or hybrid vehicles. In Bulgaria in August 2019, the Ministry of the Interior reported 984 EVs and 6,631 hybrids registered, i.e. 7615 in total, with all registered vehicles exceeding 3.8 million. In percentage terms, most EVs are sold in Norway. This is a well known fact. There, 49.14% of new cars sold in 2018 were electric, to date, out of a total of 2.7 million vehicles on the move, over 220,000 are electric. Iceland ranks second with 19.14% and Sweden with 8.01%. Next in this ranking are the Netherlands, Finland and "barely" in sixth place comes China with 4.44%. But these nearly 4.5% are equivalent to 1,053,000 EVs. Today, the leader in the EV market in China is the *BAIC Group* (officially *Beijing Automotive Industry Holding Co., Ltd.*), followed by *BYD Auto Co., Ltd.* US ranks 15th with 2.09% but real 361,000 sales (about 3 times less than China), while Norway's leader sold 73,000 EVs – Figure 1 [1].

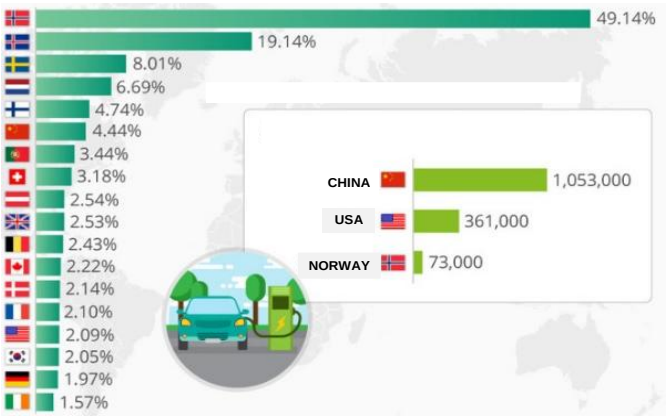


***Fig. 1** Number of EVs sold.*

Battery makers are working to improve the chemistry of lithium batteries so they don't require as much toxic material, and to enhance energy density to make batteries lighter. These developments will lessen the environmental impacts of EVs and improve their efficiency. The following parameters explain why EVs are becoming more attractive every day. A *Bloomberg Inc.* study says the average cost of batteries (with an inflation index) dropped from $1,160 per 1 kWh in 2010 to $176 in 2018. That is, eight years ago, a *Tesla Model 3* battery (75 kWh) would cost nearly $90,000. Today, such a battery costs about $13,000. This continues to be a very high price, but its downward trend continues. The future of EVs depends on the development and introduction of cheap, compact and efficient batteries. The battery will become the core of mobility. The battery supplies various types of motors as well as all electronics on board [2].

The other deterrent to the decision to buy an EV continues to be infrastructure. But there are already countries that have built the necessary infrastructure to switch the entire fleet of electricity. The Netherlands is the leader here, with an average of 19.3 charging points per 100 km. Local *Vattenfall Nuon* has announced that it will equip each *McDonald's* with at least two charging stations. For comparison, in the US there are only 0.9 stations per 100 km. In these statistics, the second place is for China, where there are 3.5 charging stations per 100 km. They look small, but let's not forget that 10,000 km (!) of highways are built annually in the Celestial Empire.

There are over 100,000 available charging stations in Europe to date. They are located in parks, on the streets, in hotels, in supermarkets, in public buildings and more. Construction on the road network is governed by the general rule that a high-speed charging station must be accessible every 120 km. In Germany, for example, the charge points are around 17,000, excluding those in everyday life. European statistics say that 70% of all charges are made at or around the workplace, so expanding the public charging network is an important but not critical factor.

In order to promote the use of hybrid and fully EVs, it is necessary to build charging station infrastructure. According to a number of studies, one of the main problems for potential consumers of EVs is precisely the lack of a well-developed charging infrastructure. Building charging infrastructure is a powerful factor in accelerating the entry of electric and hybrid (grid-powered) vehicles. This process should be stimulated, especially at the initial stage of development. However, charging EVs can create significant additional energy needs that can be met in a practical and cost-effective way through RES, including the supply of solar and wind power to the electricity grid.

Increasing the use of EVs is also an opportunity for the development of the energy system, with the potential to add the necessary flexibility to the power grids and maintain the integration of high RES shares. Electric vehicles promise to play a crucial role in the global transition to the use of sustainable energy, and in particular to the generation of renewable energy. There are several reasons for this, but the most important is that in addition to transforming the transport sector, EVs also provide an excellent opportunity to significantly increase RES shares in the overall energy mix.

Such approaches offer an attractive perspective especially for cities to decarbonise transport and at the same time reduce atmospheric and noise pollution, reduce dependence on fuel imports and introduce new urban mobility models.

2. Technical considerations

What is an Electric Vehicle – An electric vehicle is any vehicle driven solely by an electric motor powered by a rechargeable battery. Together with a voltage converter, energy distributor and/or gearbox/transmission, these components make up an electric drive module. Technically, the concept of driving an EV is like that of conventional cars – a power unit generates traction

with the help of energy. For EVs, the drive unit is an electric motor that operates through electricity stored in an onboard traction battery. The electric motor transmits the movement of the wheels through a gearbox or transmission, usually single-stage. There are also built-in electric motors that are mounted directly into the wheels. In this way, the drive is direct, without any couplers/converters, thereby achieving an even higher level of energy efficiency.

The charging topic is usually a subject of great interest and discussion. With a somewhat average approach to AC charging, *Volvo* launches in 2020 with an 11 kW on-board charger. *Hyundai Kona*, by comparison, comes with 7.4 kW single-phase on-board charger and will also receive 11 kW three-phase from 2020. It's an average approach because the 'gold' standard of 22 kW, available in several EVs, is a goal that more and more carmakers are moving toward. *Audi e-tron* and *Porsche Taycan* also have an 11 kW base on-board charger and a 22 kW as an option. The *Renault ZOE* 22 kW on-board charger has been standard equipment since 2013. With the electric *Smart* it is also an option. And this is important in terms of usability.

In Europe, EVs are not exotic for a long time, but there are still prejudices, myths and real inconveniences when using them: the charge lasts too long; charging stations are few and inconvenient; expensive rechargeable batteries. With the last generations of EVs, these problems have been practically solved. Many carmakers claim the ability to charge 5-10 minutes for a run of 100 km, and for a full charge of the battery – 30 minutes. However, these exceptional indicators are only possible for heavy duty charging stations (for example, 270 or 350 kW) and in household networks the charge lasts 4-5 times longer. The main reason for this situation is the rapid development of technologies related to EVs: autonomous mileage and the ability to charge fast. The trend is that by the end of 2019, 10% of all vehicles sold will be EVs, by 2020 – 12% and by 2025 – 20%, but there remains a concern that reliable battery life will be beyond the warranty for EVs. Usually, during the warranty period, the only operating cost is for fuel - this applies to both ICE cars and EVs. Servicing an electric motor is much simpler than that of a gasoline or diesel engine, and in general the reviews are based on software checks, calibration and other electronics settings. The battery may be subject to more detailed service tests over a period of time and to maintain its good condition, the rules and recommendations for use must be followed.

EVs retain a lower percentage than their original value after three years compared to a traditional ICE cars. This is largely related to the capacity of the battery, which gradually decreases over the life cycle. It is very important what the battery management system (BMS) is and gives them cooling and heating control. Without such a system, the battery can fall by half its capacity for several hours (this is a case with a *Nissan Leaf* battery, for example).

Given that the average European travels 40 to 80 km per day, EVs with a mileage (under the conditions of the new European cycle of movement *WLTP* – Worldwide Harmonized Light Vehicle Test Procedure, introduced from September 1, 2017) of 200 km or more are ideal for daily use.

Battery manufacturing and charging and maintenance infrastructure are the second key (after refinement for the motor part in the first place) direction in the electromobile industry. The construction of a new charging station takes into account the energy consumption of the EVs available in the region, the stability of the energy network, accessibility and investment costs. Infrastructure for the maintenance of EVs and battery charging is a sector that is about to develop at a rapid pace.

Charging stations are classified as Level 1, 2 and 3 stations. Charging stations Level 1 and 2 are conventionally called conventional and accelerated charging stations. They are not AC/DC voltage converters. These charging stations provide the required AC voltage for the on-board EV charger with a maximum load of 15 A for Levels 1 and 3, and 2A for Level 2.

Level 1 charging stations are mainly intended for home (garage) use. Slow charging stations, typically 22 kW, are mainly used for charging in households and the workplace. Because of their slow charging, the EV's battery is connected to the network for a longer period of time, which increases the ability to provide services to improve the flexibility of the energy system. Level 2 includes charging stations intended for general use which, in addition to adapting the electrical parameters of the power supply network to the electrical and structural parameters of the EV, also provide the performance of additional functions such as power consumption and cost estimates; accepting orders for recharging EVs; security functions; information on the EV and the condition of the battery; communication dialogue with the electricity provider or charging station operator, etc. Level 2 charging stations are suitable for public charging, e.g. public parking lots, supermarket parking lots, airports, stations, metro stations, corporate parking lots and more. Levels 1 and 2 do not require investment in the transmission network and the available reserves in the transmission network can provide the necessary power for the power supply. Level 3 charging stations are designed for fast charging. The duration is 10 to 30 minutes. The main difference between Level 2 and Level 3 is that Level 3 provides a DC voltage for recharging the battery of an EV. The power required to supply such a charging station is approximately 50 to 400 kW, depending on the functional electrical architecture of the charging station – for one or many subscribers. However, this cannot be ensured by the available electricity grid and the construction of this type of charging station is accompanied by new design and construction. Level 3 charging stations are equipped with buffer batteries to absorb peak loads. To provide additional electricity and reduce the power supply to these charging stations, systems for the supply of electricity from RES are also in operation. Characteristic of Level 3 charging stations is the bidirectional flow of energy - from the power grid to the battery and vice versa. This technical capability allows the charging station to become a smart grid cell. Level 3 charging stations replace 8 to 20 Level 2 stations. They are designed to absorb large flows of users [3].

Figure 2 presents the types of charging stations [10].



Fig. 2 *Types of charging stations.*

Many consider EVs as the technology of the future, but it is not so simple. The supply networks of the charging stations, which are low-voltage, at this rate of development of the production of EVs, will be loaded with about 30% more in 5-10 years. In most European countries, EVs are powered by low voltage 0.4-1 kV, from private or public charging stations. This low-voltage network is not designed for as many EVs (as one in every three cars is supposed to be an EV). In a single local power network for 120 households, charging 36 EVs would cause overload at the connection points.

To avoid this problem, €11 billion is needed to be invested by electricity providers in order to rebuild the grid infrastructure to provide 50% of the power supply to EVs. From an economic point of view, it is recommended that instead of this costly investment, take action is to make the charging process more flexible: charging to take place in the evening after 10 pm and to implement smart software solutions to manage the process. If this is achieved for about 90-92.5% of all EVs, then the peak of the network load will decrease significantly and this is a real alternative to the expensive expansion of the conventional network.

As many as 120 million EVs could be up and running by 2030, and the more EVs are on the road, the greater the collective fleet's appetite for energy. Today charging energy demand amounts to around 20 billion kilowatt-hours, with forecasts calling for it to rise to 100 billion kilowatt-hours by 2025 and 280 billion kilowatthours by 2030 [4]. This is a tall order to fill – 2030 is just ten years down the road. More efficient EV chargers could help meet rising energy demands and deliver more power.

Today's DC charging stations for EVs commonly work on about 400 V. With a typical charging power of about 50 kW, this equates to a charging time for a 400 km range of about 80 minutes. While it is possible to increase the output power of a 400 V charging station, the capacity of the conductive pins in the charging plug would still restrict the output power to roughly 100 kW. Under these conditions, it would take about 40 minutes to transfer the energy for 400 km worth of driving. The limited power capacity of the pins can be improved significantly by cooling the charging plugs, which then extends the power of the 400 V charger to the point where the target range can be achieved with a charging time of approximately 30 minutes.

The rationale behind this move is explained by the formula for electrical energy: E = U x I x t, where U is the voltage, I the current and t the time. The charging time t = E / (U x I) can thus be achieved with a constant current I by increasing voltage U. By switching to a two-fold higher voltage of approximately 800 V, the charging time can theoretically be reduced to about 15 minutes with the same electrical load on the charging pins. It should be noted that the charging speed may drop to avoid overheating the battery cells.

The first mass production OEM to capitalize on the benefits of 800 V electrification will be *Porsche* with its first fulltime EV, the *Taycan*, scheduled for launch in 2019. The first fast charging park equipped with *Porsche*'s *800 V Turbo Chargers* is located at the Berlin-Adlershof Technology Park [5]. This EV park has four customer parking spaces that are equipped with *Porsche* charging technology. Of those four spaces, two of them have *800 V Turbo Chargers* developed by *Porsche Engineering Services GmbH*. This technical concept can even work with *Teslas* with an adapter [6].

Both *Volkswagen* (with the *Budd-e* all electric van concept) and *Mercedes* (with the launch of Generation *EQ*) have confirmed that their vehicles will be capable of charging at power levels up to 150 kW for fast charging. Both OEMs have also confirmed that they envisage a future step-up to 300+ kW and 800 V.

Obviously with more carmakers adopting the 800 V standard the network will need to expand to service the needs of the consumer. This is exactly what pioneering technology provider *ABB* intends to do with its *Terra HP High Power Charge system* [7]. Ideally suited for use at highway rest stops and petrol stations, *Terra HP*'s high capacity has the ability to charge both 400 V and 800 V EVs at full power, with a charge time as little as 8 minutes for a range of 200 km [8].

Another operator focused on the expansion of the fast-charger network is *ChargePoint* who, with the roll out of their ultra-fast DC *Express Plus* charging solution, will be able to support an output of up to 400 kW accommodating charging voltages from 200 V to 1000 V; including today's 400 V EVs and 750 V buses, and tomorrow's 800 V EVs. *Express Plus* can charge the current generation of EVs, such as the *Chevy Bolt* and *Tesla*'s *Model 3*, at their maximum rate. What's more, the system is also capable of delivering the maximum charging speed to future EVs running off 800 V and delivering 350+ kW.

With consumer convenience top-of-mind, another supplier, *Continental*, developed its *'AllCharge'* technology as a 'universal charger' system capable of supplying a maximum of 350 kW at up to 800 V via the EV's powertrain [9]. *Continental* has turned the existing electric powertrain into a 'charger,' dubbed the *'AllCharge'*, capable of both AC and DC modes, using a single cable connector:

- In the case of AC current, the current flows from the charging station via the electric motor to the inverter, where it is converted into DC current before being supplied to the battery.
- In the case of DC current, the current from the charging station flows directly through the inverter to the battery.

In twenty years' time the industry may just look back at this early roll out of 800 V electrification as one of the defining moments of electromobility.

Different brands of EVs with different technical characteristics are manufactured worldwide. Air pollution from the emissions for the production of electricity needed to charge the batteries depends on the consumption of electricity per unit of road (kWh/km). For each vehicle in the technical specification, this indicator, experimentally determined when driving on a specific test cycle, is indicated. At the same mass and aerodynamics of EVs, this indicator depends on the type of battery and electric motor, the electronic control system and the use of different auxiliary systems (lighting, signaling, air-conditioning, etc.).

Here, too, as with conventional cars, traffic, driving style, temperature, power consumers in the passenger compartment, load, etc. have a great influence. It is also necessary to add that regenerative braking is a source of charge for the batteries – the regenerative braking system recharges the battery every time it slows down (often without applying the brakes), capturing the kinetic energy that is lost in conventional cars in the form of brake heat.

For EVs, a maximal consumption of 20 kWh/100 km can be assumed.The mileage is good to calculate according to the *WLTP* standard. For their part, lithium battery manufacturers typically give a guarantee of 8 years or 160,000 km for 70% of the charging capacity.

Manufacturers make EVs, as well as those with ICEs, more and more complex wheeled machines, whose computers perform millions of calculations per minute and implement connectivity to various systems within kilometers. For many operations, vehicles collect, store, process and transmit different types and volumes of data. Specifically for EV, the possible information is: travel mode selected, how long the charging plug was plugged in, where and how the charging was (fast, partial, etc.) and how low the battery was, charging mileage readings, quality of the electrical system, the position of the last charging stations used,

and about 100 last EV shutdown positions. Each trip sends a data packet that contains the date, time, GPS position, temperature and battery charge. All of these data can be inferred from driving style, EV usage profile and running time and rest.

How far can EVs travel between two charges? This is one of the most frequently asked questions by those interested in zero-emission vehicles. A new test showed the real distance that some of the most popular EVs can travel. Published data show that actual results are lower than those reported by carmakers. The test, according to the organizers, aims to determine really how far EVs can go with a single charge to help people make the right choice when buying an EV. The results of tests involved 12 of the most popular EVs in the world are presented in Table 1 [11].

Cars, including electric ones, are usually parked for 95% of their service life. These downtime, combined with adequate battery storage capacity, can make EVs an attractive solution for additional flexibility in the power grid.

Table 1: *Results from tests carried out.*

EV	Mileage declared, km	Real mileage, km	Full charge price, $
Hyundai Kona Electric	470	417	11.27
Jaguar I-Pace	470	407	15.46
Kia e-Niro	484	407	11.39
Tesla Model S 75D	489	328	13.15
Hyundai Kona Electric 39 kWh	312	254	6.87
Renault Zoe R110	299	235	7.86
Nissan Leaf	270	206	7.04
BMW i3 94 Ah	254	195	6.08
Volkswagen e-Golf	232	188	5.56
Hyundai Ioniq Electric	280	188	4.65
Smart Fortwo EQ	159	95	3.17
Smart Forfour	159	92	3.15

Any EV can play the role of a storage microsystem with the potential to provide a wide range of network services. According to analyzes by the *IRENA* (International Renewable Energy Agency), the battery capacity of EVs in the future may exceed that of stationary batteries. The analysis also shows that in 2050, there will be a capacity of about 14 TWh of EVs batteries to connect to the grid, compared to 9 TWh of stationary energy storage batteries.

At the same time, uncontrolled charging can increase peak network pressure, which will necessitate corresponding upgrades at the power level. Uncontrolled charging of EVs has led to an increase in electricity production and consumption, several studies show. However, the impact on peak consumption can sometimes be much greater. According to a study from the United Kingdom, if the number of EVs reaches 10 million by 2035, evening peak consumption will increase by 3 GW for uncontrolled charging and by only 0.5 GW if charging is smart. If more than 160 million EVs are in use by 2030, a large number of them are concentrated in certain geographical areas and their charging is uncontrolled, the local electricity grid will be congested. In order to avoid such a situation, it will be necessary to strengthen and update the network in these areas. However, with smart charging, these investments can largely be avoided. It is typically used with slow charging infrastructure in low voltage distribution networks. For example, the operator of the Hamburg electricity distribution system analyzes and concludes that a 9% share of EVs would result in insufficient capacity of 15% of the power lines. To prevent this, a smart charging solution is being implemented and devices are being monitored for loading at different points in the charging infrastructure.

If the use of the charging stations is subject to a preliminary annual subscription and the electricity consumed is paid at nominal prices, the charging station may be profitable. The technology of manufacturing charging stations is well known and many are commercially available as finished products. What is missing are uniform agreed international standards to which charging stations and their components such as plugs, cables, colors, voltage specifications, and more, meet. In addition, there is often a lack of regulations for the sale of electricity from such stations, uncertainty about municipal investment in such (charger) infrastructure, unknown government policy regarding investment in charger infrastructure, a cumbersome and costly licensing process for chargers.

With regard to the production and operation of charging stations, it is necessary to establish uniform global standards for the physical attachment of rechargeable batteries to charging stations; for a communication protocol between the charging station and the electricity providers and the EV owner; for communication protocol between the charging station and the EV, and for switching on and monitoring the operation and management of the charging station when networked to a 'smart grid' system in perspective. At this stage, there are many technological uncertainties about the development prospects of rechargeable batteries. Now there is a process of intense search, accompanied by huge financial investments in research and development. This is also catalyzed by the search for oil substitutes and finding ways to store electricity produced. There is evidence of the development of lithium batteries based on nanotechnologies with an energy density of 2000 Wh/l and 45000 charge/ discharge cycles.

According to expert analyzes, the massive entry of EVs into the EU, which will begin in the next 5 years, will lead to the emergence of new technologies, industries and professions, EU Member States failing to keep up with new technologies and their information and infrastructure security will suffer significant commercial losses and will be subject to amercements for the use of gas and diesel transport and the insufficient capacity of national charging station networks [12].

ACEA, *Eurelectric* and *Transport & Environment* (*T&E*) issued a joint statement in September 2019 calling on the European institutions to support the rapid creation of smart charging infrastructure for EVs. *ACEA* is the European Automobile Manufacturers Association, of which *BMW Group*, *CNH Industrial*, *DAF Trucks*, *Daimler*, *Fiat Chrysler Automobiles*, *Ford of Europe*, *Honda Motor Europe*, *Hyundai Motor Europe*, *Jaguar Land Rover*, *Groupe PSA*, *Renault Group*, *Toyota Motor Europe*, *Volkswagen Group*, *Volvo Cars* and *Volvo Group* are members. *Eurelectric* represents the interests of more than 3,500 companies in the European electricity industry, and *Transport & Environment* (*T&E*) is a leading European clean transport campaign group, with over 60 member organizations in 25 countries.

The three associations unite on the importance of lawmakers and policymakers reforming important regulations, such as the upcoming *Alternative Fuel Infrastructure Act* (*AFID*) and the *EU Buildings Directive* (*EPBD*), to allow EVs to reach every home, workplace and road .

This will require a massive deployment of strategically located smart charging infrastructure across the European Union. Intelligent (or smart) infrastructure means that charging systems are designed to provide convenient and easy access and use, communication with centralized computer systems with interactive features and technical solutions designed to avoid power grid congestion. To this can be added the *V2G* (*Vehicle to Grid*) functionality by which the battery energy of EVs can be fed back through charging stations to the grid. *Automotive News Europe* notes that *Nissan Leaf* is certified as an energy source in Germany, Denmark and the UK, allowing it to connect as a *V2G*.

According to the three associations, such developments will provide clear benefits for consumers, the electrical system, the automotive industry and the public at large.

Where to charge

The average charging price varies depending on the astronomical charging time, charging speed, and point selected. In the UK, the *Compare The Market* app allows you to choose your charging point while traveling in Europe and how much it will cost you – Table 2 [13]. In Germany, where the share of RES is 41% of the generated energy, electricity costs € 0.2/kWh. In Denmark, which has long been proud of its highest share of wind energy, the *NewMotion* app is worth € 0.3/kWh.

Some countries allow consumers to choose electricity providers. *UKPower* is an energy benchmarking service that helps UK consumers compare charging prices between energy providers and possibly save money by switching. There are similar opportunities in Germany. According to the *North Rhine-Westphalia Consumer Association*, customers can choose from at least 20 different providers that cover the whole country, potentially saving up to 20-30% of their electricity bills.

The lack of a sufficiently developed network of charging stations for now makes plug-in cars more convenient for urban environments. In this case, electromobility means freedom of movement in urban centers and green areas with limited traffic.

However, the larger the battery of an EV, the longer it will take to charge a standard outlet. There are sites like international *plugshare.com* that indicate where public charging stations are.

On October 12, 2017, *Shell* acquired *NewMotion* – Europe's largest network of charging stations with 170,000 registered users and over 100,000 available charging points, in Bulgaria they are 11. The convenience of charging an EV is a request to visit a gas station, which is completed in a smartphone application. This makes driving comfortable and time-saving and well-planned. It is no coincidence that *NewMotion*'s ambitious motto is: "We will break down the concept of charging EVs for the different 'levels' of charging and help you understand how to use them.".

At the end of 2017, one of the leading markets, the Netherlands, has a total of 107,000 charging stations registered public and private. At Europe level, charging stations are already several hundred thousand – if we are talking about smaller stations. Higher power DC charging stations are up to 15-16% of the total 17,000 in Germany, for example, according to data from a branch organization quoted by the *DPA* (German National News Agency). The government plans to encourage electric mobility in Germany envisage increasing the number of charging stations to 50,000 within two years.

In October 2018, *Google Maps* has already called the charging stations for EVs. One of the main features of *Googlé Maps* is to help the users to arrive at a designated location without significance for this type of vehicle.

That is why, the information about the closest charging stations for EVs would have been raised in time. Now you can find similar information for the closest electric charging stations. Detailed information can now be found on the nearest electric charging stations by offering a route to them that matches the battery charge remaining in the electric vehicle's batteries. For picking up the nearest electric charging station, it is sufficient in Search field to be filled in *EV charging* or *EV charging stations*. Online service offers geographical coordinates, type of connectors, free charging places for EVs, prices for charging, etc. For all stations, the data from the previous users - pictures, ratings, opinions and answers to the most frequently asked questions - are available.

To date, *Google Maps* maintains a network of *Tesla* and *Chargepoint* charging stations (worldwide, including Bulgaria), *SemaConnect*, *EVgo*, *Blink* (for the United States), *Chargemaster*, *PodPoint*, *Chargefox* (for the territory of Europe). The list will gradually increase and complete.

Table 2. *Prices according EV charging* [13]

Country	Price, €/kWh	Charge price, €	Price for 100 km
ESTONIA	0.12	11.57	2.78
HUNGARY	0.12	11.57	2.78
CZECH REPUBLIC	0.12	12.46	2.99
LITHUANIA	0.12	12.46	2.99
ICELAND	0.13	13.35	3.20
TURKEY	0.13	13.35	3.20
POLAND	0.14	14.24	3.42
FINLAND	0.15	15.13	3.63
SLOVAKIA	0.15	15.13	3.63
LATVIA	0.16	16.02	3.85
NETHERLANDS	0,16	16.02	3.85
SLOVENIA	0.16	16.02	3.85
FRANCE	0.17	16.91	4.06
GREECE +	0.17	16.91	4.06
LUXEMBOURG	0.18	17.80	4.28
NORWAY	0.18	17.80	4.28
SWITZERLAND	0.18	17.80	4.28
SWEDEN	0.19	18.69	4.50
UNITED KINGDOM	0.2	19.58	4.50
AUSTRIA	0.2	20.47	4.92
SPAIN	0.21	21.36	5.14
IRELAND	0.23	23.14	5.56
PORTUGAL	0.23	23.14	5.56
BULGARIA	0.09	7.08	2.36
ITALY	0.24	24.03	5.77
BELGIUM	0.25	24.92	5.99
GERMANY	0.29	29.37	7.06
DENMARK	0.3	30.26	7.28

Groupe PSA (a carmaker of *Peugeot*, *Citroen* and *Opel*) has been active in the field of electric mobility this year and, in addition to launching several new EVs, also purchased the English *ChargePoint* network through the French operator *ENGIE*.

In August 2019, *TomTom* announced that it was updating the list of charging stations and their data in the navigation of EVs. This is true of the automakers *TomTom* works with.

ABB has been selected as a major technology partner and supplier in a pilot project to build a network of EVs charging stations across Europe. The project is the work of *IONITY*, the first service station has been opened in Neuenkrach, Switzerland, on the *A2* motorway. *IONITY* is a joint venture of *BMW Group*, *Daimler AG*, *Ford Motor Company* and *Volkswagen Group* with *Audi* and *Porsche*. The enterprise project includes six of *ABB*'s most advanced high-speed charging stations, *Terra High Power*, with a power of 350 kW and a 200 km mileage in just 8 minutes. By 2020, *IONITY* plans to operate a network of approximately 400 fast charging stations in 24 European countries [3].

The *Volkswagen Group* has announced its intention to significantly expand the company's investment in EV charging infrastructure, with plans to install 36,000 charging points in Europe by 2025. *Volkswagen* is already involved in the deployment of some charging networks, such as *IONITY*, but the German carmaker plans to expand its own direct involvement in EV charging. *Volkswagen* is aiming for a rapid breakthrough in the world of electromobility and is redoubling its efforts in the charging infrastructure. Across Europe by 2025, the *Volkswagen Group* will install a total of 36,000 charging points; 11,000 of these will be developed by the *Volkswagen* brand. They will be

installed at *VW*'s factories and at around 3,000 *Volkswagen* dealerships in all major cities.

New obstacle in the way of electric vehicles

The high prices for EVs and the shortage of charging stations have already added another barrier to the massive entry of electric cars for everyday use. In Germany, Europe's largest overall car market, starting from April 1, 2019, there is a new mandatory requirement for each charging station to have meters installed to show drivers how much electricity is being charged. A similar measure is under consideration across the European Union. However, one of the conditions is to find manufacturers for these meters. And although in Germany the measure has already been introduced and has been in force since April 1, 2019, similar charger adaptations are still not being manufactured, according to industry experts cited by the *DPA* [14].

Charging stations now show EV owners how many minutes they can drive in a single charge. However, it turns out that there are currently no measuring devices available for DC charging stations, and the union of *BMW Group*, *Daimler AG*, *Ford Motor Company* and *Volkswagen Group*, is working to install such devices on German highways. *IONITY* noted that they are in talks with the German authorities and expect the necessary technology to be adapted to the current charging stations will be available in the next months. The charging stations already installed will be upgraded, not dismantled.

3. Conclusions

It is well known that the optimal solution never depends on one component only, but on the exact coordination of all components. Therefore, it is important to always analyze and evaluate the overall solution, both from a technical standpoint and in terms of costs and benefits.

For each country at this stage, the entry of EVs is at different rates. There is still a lack of awareness among the population of how electronics and propulsion developments are changing the world of transport, as well as the lack of enough companies to supply EVs with the corresponding approved quotas from carmakers. Soon new EVs will emerge, capable of traveling more serious distances in a single charge. Diversity is already there and will be much greater. A well-organized awareness campaign is needed, accompanied by a real presence on the roads of EVs, engaging companies with the supply of new and companies to convert vehicles with ICE into EVs, offering financial instruments for leasing batteries and/or the entire EV, as well and local or national incentives for EV users. There is a need for a specific legal framework with appropriate measures, which would create additional opportunities for more intensive use of EVs.

Generally speaking, despite the many breakthroughs, one thing stands out and that is that it often takes decades for people to understand and to perceive something.

References

1. https://auto.mail.ru/
2. www.emic-bg.org/
3. www.tllmedia.bg/
4. Baran Özbakir, and Gábor Manhertz. Benchmarking System Architectures and Topologies for DC-to-DC Converters, the Heart of Off-Board Chargers. May 2019 www.bodospower.com
5. Nicolas Zart; Clean Technica; Porsche Inches Into Superfast Charging 800 Volt Chargers; July 2018, https://cleantechnica.com/2018/07/17/porsche-claims-400-voltsfor-400-kilometers-with-superfast-800-volt-chargers/
6. Fred Lambert; Electrek; Porsche's ultra-fast charging infrastructure for the Mission E will also work with Tesla, says CEO; October 2017, https://electrek.co/2016/10/03/porsches-ultra-fast-charging-infrastructure-for-themission-e-will-also-work-with-tesla-says-ceo/
7. ABB; ABB powers e-mobility with launch of first 350 kW high power car charger; October 2017, http://www.abb.com/cawp/seitp202/c2ed43a8ef2e1de2c12581ae002d26b8.aspx/
8. Nancy Owano; Tech Explore; ABB unveils EV charger can add 200 km of range in 8 minutes; May 2018, https://techxplore.com/news/2018-05-abb-unveils-ev-chargerkm.html
9. Mark Kane; Inside EVs; Continental AllCharge enables 800 V, 350 kW Charging; June 2017, https://insideevs.com/continental-allcharge-enables-800v-350-kw-charging/
10. https://new.abb.com/ev-charging/bg
11. http://thisismoney.co.uk
12. http://dnes.bg
13. https://www.comparethemarket.com/car-insurance/content/cost-of-charging-an-electric-car-globally/
14. http://www.infostock.bg

RESEARCH WORK ABOUT THE TROUBLE-FREE OPERATION OF A ROBOTIC CELL FOR THE WELDING OF THE BOGIE FRAME ON A FREIGHT WAGON

M. Sc. Edrev St. [1], Assos. Prof. Topalova M. PhD[2]
University "Prof. D-r Asen Zlatarov" – Burgas, Bulgaria [1]
Faculty of Engineering and Pedagogy – Sliven, Technical University – Sofia, Bulgaria [2]
stancho.edrev@abv.bg[1] m_topalova@tu-sofia.bg[2]

Abstract: *This research work presents the results of the monitoring on a robotic cell operation for welding the bogie frame on a freight wagon for two months. The structure of the robotic welding cell is revealed and a register of the occurred failures was formed. A statistical processing of the received information has been made and an analytical expression about the trouble-free operation has been determined. Recommendations for increasing trouble-free operation are suggested.*
Keywords: RELIABILITY, ROBOTIC WELDING CELL, FAILURE, TROUBLE-FREE OPERATION PROBABILITY

1. Introduction

The trouble-operation of a technical system is determined by one of the private properties of reliability – faultless work. Quantitative reliability has been assessed by criteria: probability of faultless work, probability of failure, flow refusals parameter, etc. The realistic design standardization is especially important because it participates in the determination of the project performance and at the production stage is demonstrated the prognosis of probability.

A robotic welding cell (RWC) on the frame of the bogie on freight wagon is part of a robotic complex where the frame components have been welded.

In RWC industrial robot Motoman-6 HP welds the frame components (Fig. 1) that consists of two longitudinal beams (1), connected in the middle by centralbolt beam (2), and ends with two transverse beams (3). To this frame construction four axel jaws (4) are aggregated for the suspension of the frame to the axles and a number of strips for mounting the braking system elements. The components of the frame have been set manually before entering the RWC, where the set frame have been put in two coordinate devices. The program cycle duration of the frame components welding is 82 min [2].

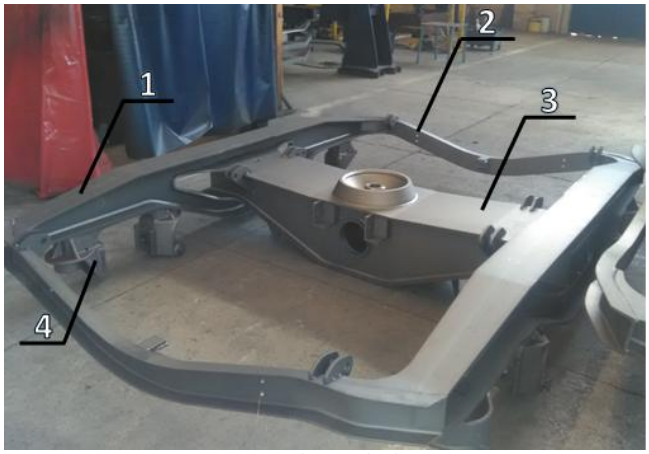


Fig. 1. *The bogie frame of a freight wagon*

During operation, faults arise of different physical nature that disrupt the normal functioning of RWC and reduce its performance. Both internal and external factors are influencing the working capacity.

The purpose of this study is to discover emerging failures, their physical nature and their distribution law.

2. Structure of the robotic welding cell

The Fig. 2 schematically presents the structure of RWC.

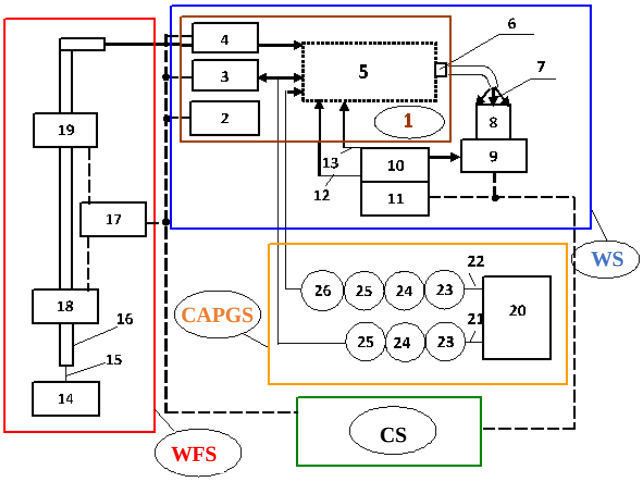


Fig. 2. *Block-diagram of the robotic welding cell*

The following set systems and their components are distinguished based on a functional principle in the RWC:

Workflow System (WS) – welding robot (1), welding machine control unit (2), cleaning station (3), main wire feeder (4), hose (5), welding burner (6), welding arc (7), welded part (8), adjusting device (9), welding machine (10), welding machine control unit (11).

Wire Feeder System (WFS) – a roller with additional wire (14), additional wire (15), core (16), wire feeder blocks control (17), wire feed units (18, 19).

Compressed Air and Protective Gas System (CAPGS) – factory trunk line (20), shut-off valve (23), filter (24), pressure gauge (25), flowmeter (26).

Computer system (CS).

The welding burner (Fig. 3) and the welding machine are the main functional elements of the work process. The relationship between them is made by means of a hose that secures the bulk cable (13), the cooling piping (12) and the elements of the compressed air systems (21), protective gas (22) and wire feeding. The elements of the welding burner work under extreme conditions and have a short technical resource. They are defined as consumables and are always spare parts for quick removal of related faults. For the same purpose are a spare burner and a spare hose have been provided.

The large size of the work area necessitated the construction of an additional wire feeder system to support the main feeder block mounted on the welding robot. Its structure is shown in Fig. 4. Supplementary wire feed units (18 and 19) include quick couplers (4), electric motor (1), gearbox (2) and friction rollers (3). The positions in brackets correspond to the positions in Fig.2.

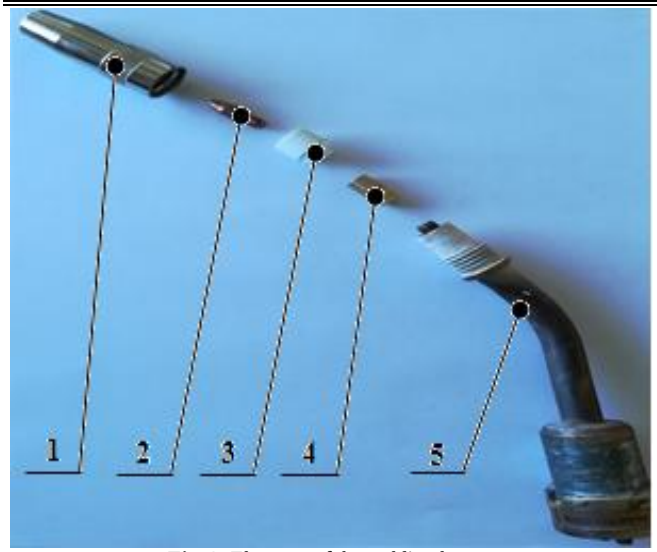


Fig. 3. *Elements of the welding burner*
1 - gas nozzle; 2 - current nozzle; 3 - insulator sleeve;
4 - gas distributor; 5 - body;

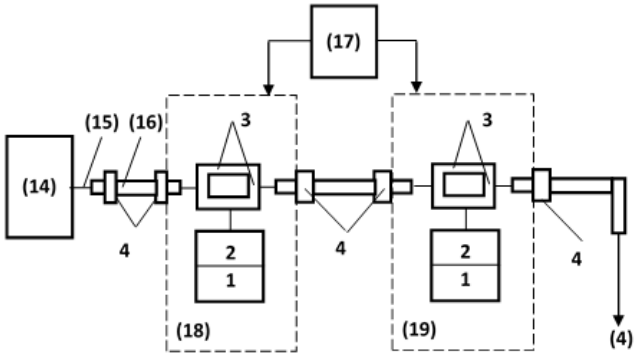


Fig. 4. *Flowchart of the supplementary feeder system*

The cleaning station removes stuck metal and slag particles on the inside of the gas nozzle, which reduce the diameter of the orifice and reduce the effectiveness of weld seam protection. At present, the cleaning station is not functioning and the operators performs its functions (limited in scope).

3. Statistical study of the robotic welding cell operation

The monitoring on the RWC's operation continued for two months (40 working days) under two-shift mode. During this period, 167 program cycles (articles) were completed and 66 failures were registered, the type of which is given in Table 1.

When collecting the necessary statistical information, the method of the observed operation is applied – the information in an advance prepared forms for each working day is filled by the instructed operators of the welding robot. As a result of their processing, a register of failures was formed, which clearly shows the type and the moment of the origin of the failures, the minimum and maximum duration of the periods of the trouble-free operation, etc.

An excerpt from the failure log is given in Fig. 5.

Failures occurred by reasons outside of RWC, such as lack of protective gas and or compressed air in the factory trunk line; damaged crane, blocked transport system.

4 . Processing of monitoring results

The subsequent processing of the obtained statistical information is related with the determining of the statistical function of the trouble-free operation of the RWC and finding an analytical expression for its presentation. Using the Sturges formula [3] the width (***t***) of the intervals is determined at which the trouble-free cycles taken from the failure register have been grouped.

Table 1. *Types of failures*

Code	Type of failure
1	Movement without welding with wire feed
2	Current Nozzle Failure
3	Refusal to gas nozzle
4	Insulator bushing failure
5	Gas distributor failure
6	Impossible welding start
7	Holding the torch in the milling cutter
8	A group of pores in a welded joint
9	Weld seam cut
10	Large protrusion of weld
11	Restart of the welding machine
12	Lack of search
13	Lack of protective gas
14	Charging with extra wire
15	Absence of compressed air
16	Hose leakage
17	Break the fast connection
18	Blocked transport system

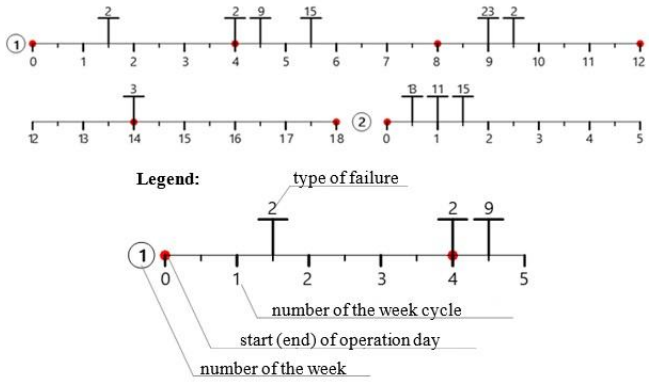


Fig. 5. *Excerpt from the register of failures*

(1) $$t = \frac{x_{max} - x_{min}}{1 + 3{,}322 \log N} = \frac{7{,}5 - 0{,}5}{1 + 3{,}322 \log 167} = \mathbf{0,99}$$ cycles

x – maximum (minimum) number of cycles of trouble-free operation;
N – total number of failures.

A width of one-cycle intervals was adopted, resulting in eight intervals (see Table 2).

Formula (2) [1] determines the average number of trouble-free cycles.

(2) $$t_{cf} = \frac{\sum_1^n f_i t_i}{\sum f_i} = \mathbf{2,5}$$ cycles

According to the data in Table 2 and the dependence (3) [5] the values of the statistical function for trouble-free operation have been determined (see Table 2) and its graphical interpretation is shown in Fig. 6.

(3) $$P^*(t_i) = \frac{(N - \sum_1^i f_i)}{N}$$

The hypothesis for an exponential law of the probability of the failure-free operation of the RWC has been put forward, which at $t_{cf} = 2,5$ cycles yields the form (4) [4]:

(4) $$P(t) = e^{-\frac{t}{2,5}}$$

Table 2. *Results of the statistical processing of the monitoring data on the work of the RWC*

№		1	2	3	4	5	6	7	8
Link intervals		0-1	1-2	2-3	3-4	4-5	5-6	6-7	7-8
Middle intervals, t_i		0,5	1,5	2,5	3,5	4,5	5,5	6,5	7,5
Frequency of refusals	Statistic f_i^*	21	13	9	8	5	5	3	2
	Theoretical f_i	22	17	13	9	7	5	4	3
Probability of trouble-free operation	Statistic $P_i^*(t)$	68,2	48,5	34,8	22,7	15,2	7,6	3,0	0
	Theoretical $P_i(t)$	67,0	44,9	30,1	20,2	13,5	9,1	6,1	4,1
Cumulative failure rate	Statistic $\sum f_i^*$	21	34	43	51	56	61	64	66
	Theoretical $\sum f_i$	22	37	47	54	59	62	64	66
Difference between cumulative frequencies $\left\|\sum f_i^* - \sum f_i\right\|$		1	3	3	3	3	1	-	-

The probability values for the failure-free operation are shown in Table 2 and Fig. 6.

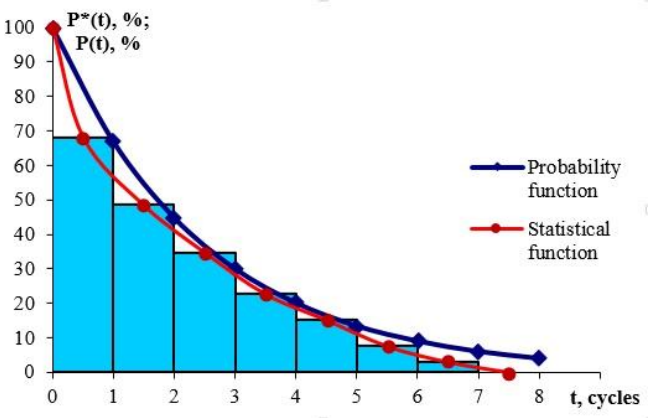


Fig. 6. *Theoretical and statistical functions of reliability*

Statistical verification of the hypothesis of an exponential probability distribution law for failure-free operation was performed according to Kolmogorov's criterion [3]:

(5) $$\lambda = D/\sqrt{N}$$

D – maximum difference between the cumulative frequencies of the statistical and theoretical distributions.

Ehen there is a maximum difference between cumulative frequencies $D = 4$ is obtained $\lambda = 0,492$ and the probability $P(\lambda) = 0,96998$. Therefore, it can be assumed that the exponential distribution is an adequate statistical model.

The conducted statistical observation and analysis of the obtained results allow us to formulate the following recommendations for trouble-free operation of RWC:

✓ Welded parts must be regularly cleaned of corrosion and grease stains to reduce the number of failures with codes 2, 3, 6 and especially 8.

✓ It is necessary to repair the cleaning station in order to eliminate: the breach of the technology for cleaning the elements of the welding burner; the increasing probability of part of the failures; loss of time from manual lubrication of the gas nozzle; increased operator workload.

✓ The timing of the change of wire must be strictly observed in order to prevent prolonged stays of the RWC.

✓ The nomenclature and the quantity of spare parts, as well as the inventory of purchased items, should be optimized to reduce the duration of RWC stay.

5. Conclusions

- The physical nature of emerging failures in the RWC has been discovered and analyzed to formulate sound recommendations for increasing trouble-free operation.

- An analytical term has been found describing the true work of the RWC to develop a mathematical model for the investigation of the reliability of the RWC.

- An exponential distribution of the probability of failure-free operation has been proven to create the opportunity to conduct adequate simulation studies of RWC.

References

1. Chakarski D., T. Vakarelska, Vl. Stankov, A. Raykov, Industrial robots, robotic cells and systems, Sofia, Technical University – Sofia, 2003.

2. Edrev St. Operational reability of a Motoman welding robotic complex, Announcement Union of Scientists - Sliven, vol. 33, book 1, 2018, pp. 65-69.

3. Gatev K., D. Koseva, A. Spasov, General Theory of Statistics, Science and Art, Sofia, 1991.

4. Petrov N. Operational reliability of risky technical systems, Yambol, Publishing Complex "Zhelyo Uchkov", 2002.

5. Vochkevich L., Automation of production processes, Moskva, Mechanical Engineering, 2007.

IMPROVEMENT OF GROUND PUMPS FOR TRANSPORT OF SLURRY

Doct. student Seitkhanov A.[1], Prof. dr. eng. Povetkin V.[2], Dr. phd Bukayeva A.[3], Prof. dr. eng. Ivanov S.[4]
Department of Industrial Engineering - Satbayev University[1], Department of Thermal Physics and Technical Physics - Al-Farabi Kazakh National University[2], Department of Mechanical Engineering and Transport - Yessenov University[3], Kazakhstan,
Department of Mechanical Engineering - St. Petersburg Mining University[4], Russia

Abstract: *The analysis on improvement of soil pumps which are used in the ore-dressing enterprises of the Republic of Kazakhstan is provided in article. As a result of the analysis of operation of soil pumps it is revealed that soil pumps, don't meet modern requirements in reliability and power consumption, and possibility working parameters adjustment. The main shortcomings of soil pumps is low life cycle of flowing part components. At the moment the main solutions to increase operational resource of soil pumps are — decreasing of cavitation processes; reduction of hydro abrasive mixture flow in the impeller cavity, that will reduce surface wear of impeller elements and increase pump inlet capability; For pulp pumping - reduction of vibration influence both of hydro abrasive mixture and pump overall; Slurry solids extraction prior to its inflow into the cavity of the impeller and its blades. The following Innovative technologies for improvement of soil pump operational life and wear reduction of impeller parts surfaces were provided.*
KEYWORDS*: SOIL PUMPS, PULP, PIPELINE, IMPELLER, THREADED CONNECTION, HYDRO TRANSPORT, MAIN PIPE, COVER PLATE, SEALING, BOWL.*

1. Introduction

Kazakhstan ore-dressing enterprises mainly utilize hydraulic conveying for hard materials transportation. Hydraulic conveying considered as an effective and cost-effective way of mainline transportation. The hydraulic conveying unit applies centrifugal soil pumps for abrasive slurry fluid transportation. Due to reliability and life span of such pumps depends not only the operation of equipment applied in a process flow but also the quantity and quality of a resulting product.

Currently, nonferrous metallurgy enterprises utilize thousands of soil pumps, 80-90% of which are obsolete and exceeded their lifespan. Soil pumps, with which concentrating mills are mainly equipped, do not meet present-day requirements on reliability, energy output and ability to adjust operating parameters. Owing to the low service life of impellers and bowls, 100% reserve of such components is required.

Analysis of soil pumps maintenance charges demonstrates that the major part of such expenses related to worn-out parts replacement. As a result of worn-out parts, maintenance charges composed of spare parts price, dismounting cost and expenses due to equipment downtime if there is no pumps reserve. Equipment downtime and additional expenses on pumps mounting and dismounting also related to clogging of pumps flow part channels.

Therefore when assessing pumps performance, such parameters as reliability, wearability and flow section sizes will be of paramount importance.

To date, in a result of soil pumps maintenance problems analysis, it has been identified that soil pumps with which mining and concentration enterprises are equipped do not meet present-day requirements on reliability, energy output and ability to adjust operating parameters. The major disadvantage of soil pumps is the low life span of flow parts as a result of hydro abrasive and cavitation wear [1-3].

Thus, in order to improve the operating efficiency of soil pumps, research of operation, design, and wear is the most pressing challenge.

2. Preconditions and means for resolving the problem

Patent analysis of inventions related to soil pumps up to the 2015 year indicated that the focus area for quality and reliability improvement of soil pumps is upgrading flow part design and application of wear-resistant materials.

Proposed design decisions for developing efficient soil pumps are as follows:

- Increase of disc thickness in the max. wear area;
- Presence of vibrating elastic tape in flow channel;
- Presence of grooves in impellers;
- Application of protective cover from a highly rigid material;
- Local turbulent flows formation, laminar flows displacement from the periphery to axis flow;
- Vibration reduction through intermediate bearings;
- Reduction of hydrodynamic friction through the influence of variable electromagnetic field on boundary liquid layer;
- Presence of asymmetric wear bushing of pump housing for stabilization of medium flow;
- Use of double-lead flexible screw;
- Impeller design (submersible multistage pump) – monolithic, cast-iron;
- Change of inner pipe design – the presence of longitudinal ribs with fixed cylindrical slots in order to decrease aerodynamic friction resistance and reduction of boundary layer thickness;
- Presence of friction and wear rings in order to restraint liquid film between them, as a result – wear reduction during Impeller rotation;
- Technological solutions, in most cases, are related to the implementation of different materials for the production of the main components of soil pumps;
- Production of pump components from carbon fiberfill, pyrocarbonazing and siliconizing;
- Application of iron, carbon, molybdenum, copper, and chromium based powder material to increase friction pair wearability;
- Use of elastomer as wear-resistant material for cover plate production;
- Use of composite material for impeller production.

Basic design solutions are related to design modification of main components of soil pumps, application of various coverings in hydro abrasive wear areas, use of advanced materials both for pump components production and for coverage.

Key factors for determination of soil pumps operational characteristics are: hydro abrasive wear of flow part that leads to rotor unbalance and vibration increase, flow loses; cavitation wear resulting in intermittent vibration growth and flow part destruction of soil pumps; soil pumps operation in substandard vibration area which was caused by design features and flow parts unbalance, imperfection of assembly.

To increase the endurance of soil pumps we propose to implement the following actions:

1) Decreasing of cavitation processes;
2) Reduction of hydro abrasive mixture flow in the impeller cavity, that will reduce surface wear of impeller elements and increase pump inlet capability;
3) For pulp pumping - reduction of vibration influence both of hydro abrasive mixture and pump overall;
4) Slurry solids extraction prior to its inflow into the cavity of the impeller and its blades.

To meet these challenges technical solutions that will improve operational characteristics of soil pumps are purposed.

In invention № 24120 [4] and № 23554 [5] construction solution for improvement of soil pumps parts – impeller and cover plate, is applied. That will result in a life span of soil pumps.

A number of inventions № 30467 [6] and № 30468 [7] include innovative technologies, such as antivibration system (vibration damper) for softening pumping action caused by impeller vibrations in an increasing unbalance conditions.

The first concerns pump case (fig.1) installed on a base plate (spring-loaded base) that connected with springs, connecting rods, cranks, and motor, and impeller speed $co_к$, equals one half of crank $co_к$, speed, and crank radius is determined using the formula r = l/8R, where R – impeller radius.

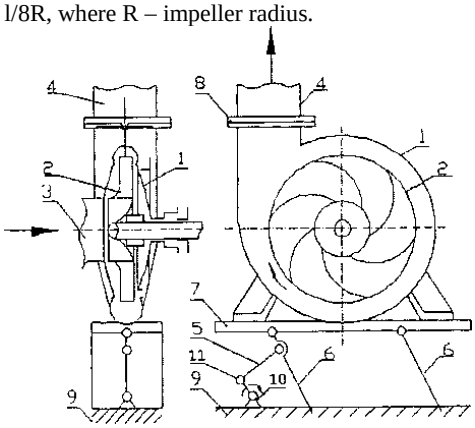


Figure 1. *Ground pump design*

1-housing, 2-wheel, 3-pipe suction, 4-pipe discharge, 5-coupling eccentric drive, 6-spring, 7-support plate (spring-loaded base), 8-seal, 9-bottom plate (base), 10 - centric drive, 11 - curved bearing

Case of soil pump on fig.2 installed on springing elements which are vibration dampers mounted at 90º in supporting casing relative to one another, and inlet and outlet pipelines for hydro abrasive mixture connected to the pump with flexible connectors.

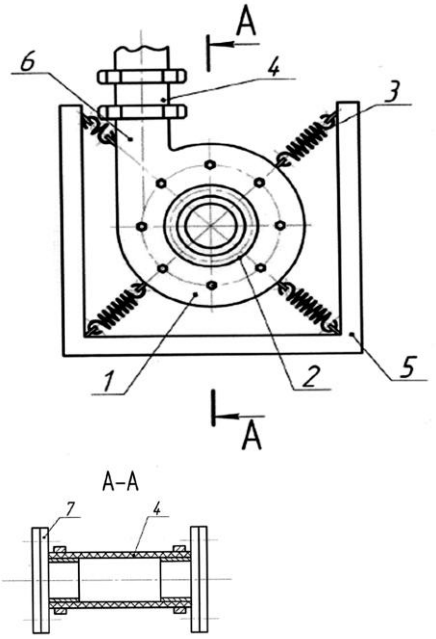


Figure 2*. Ground pump*

1 - pump casing, 2- impeller, 3 - spring dampers, 4 - flexible inserts, 5 - pump hanger casing, 6 - halves,

7 - pipelines for the supply and discharge of the waterjet mixture

In invention № 28727 [8] improvement of soil pump operational life and wear reduction of impeller parts surfaces is made through the installation of impeller at a certain angle to drive axis shaft, e.g. 1—3°, which provide pulp cross-motion on impeller blade in the axial direction from impeller disk walls in two opposite directions per one rotation, and in gaps between impeller disks and cover plates cups are installed that provides air-tightness of the connection when moving the impeller disk walls due to their elastic properties. Besides, to prevent solid particles entering into a gap between the external wall of the impeller and cover plates, clear water piped under pressure exceeding pipe outlet pressure at least at 0.05 MPa.

Fig. 3 illustrates soil pump design.

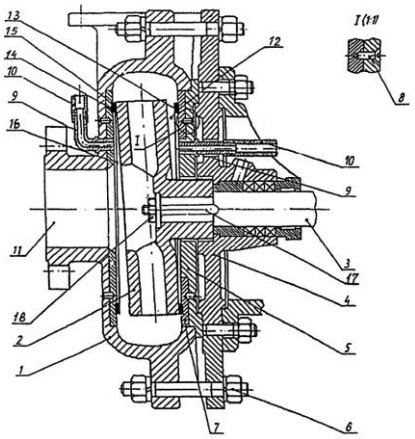


Figure 3. *Ground pump design with impeller inclination*

1 - casing, 2 - impeller, 3 - shaft, 4 - flange, 5, 14, 16 - flange, 6 - stud, 7 - change ring, 8 - threaded connections, 9 - inlet line, 10 - hose, 11 - pump cavity, 12 - gap, 13,15 - elastic cuff, 17 - key, 18 - nut

Inventors of technical solution № 28600 [9] applied a comprehensive approach – installation of the cryogenic device on input manifold that can reduce the temperature of supplied flow. Screw, installed on the impeller shaft on the same manifold, provide continuous pulp feed to impeller and reduction of impeller rotation.

In invention № 28601 [10] where the main task was to increase the life span of centrifugal soil pump for pulp transportation, a set of equipment is used. The device equipped with an ejector soil pump installed on the pump main for pulp pumping-over. Ejector soil pump designed with removable nozzles located in «turret» swivel head.

The object of the technical solution № 29439 [11] was to make a design that will increase the life span of the pump and simplify its construction. To solve this problem, in the casing of soil pump impeller located together with cover plates and gap wash system that used clear water for flushing gaps between the impeller and cover plates. Screw installed in a pressure chamber to provide additional pressure in interblade blades of the pump impeller, thereby suction value grows. In addition, a pump is equipped with a hydraulic cyclone in the form of a tubular design located in inlet manifold enabling to extract solid abrasive particles from pulp.

Pulp feeds to hydrocyclone separator through a manifold that designed tangential to cyclone circle for flow swirl and further transfer to each of the hydrocyclone separator cavities. Slide gate located at the hydrocyclone separator bottom for pulp solid particles discharge and it's further conveying outside the workshop. The conveying system consists of screw and belt conveyor (fig. 4).

Technical solution № 30949 [11] proposed a gritty liquid pumping system that will increase pump operational life, provide high-efficiency and automation of the pumping process. With the use of a control system, which electrically connected to a pulp level limit sensors, the present system can provide automation for working fluid (pulp) pumping process. In addition, a spring-loaded adjustable valve installed for pulp continuous feed to a tank during suction and for pipeline sealing in case of pulp displacement from the tank.

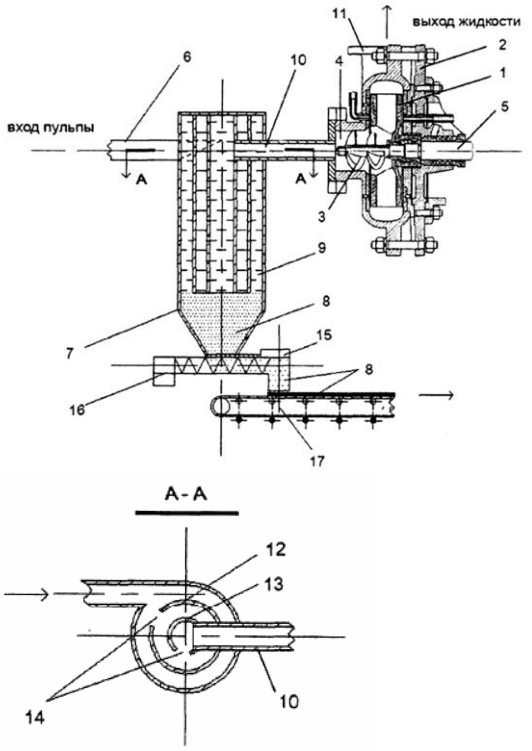


Fig. 4. *Pump ground with hydrocyclone*
1 - impeller, 2 - pump, 3 - screw, 4 - falling cavity, 5 - drive shaft, 6 - falling line, 7 - hydrocyclone phase-separator, 8 - solid particles, 9 - liquid, 10 - line, 11 - volute, 12 and 13 - pipelines, 14 - windows, 15 - slide gate, 16 - screw feeder, 17 - belt conveyor

Operational life improvement of gritty liquid pumping system achieved by the design of contralateral service tanks with systems for supply vacuum and pneumatic pressure from compressor, and control system for automation of pulp pumping process that can provide pulp continuous feed and service tanks sequence (fig. 5).

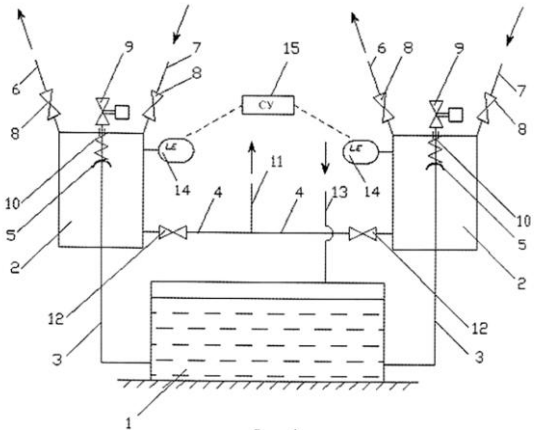


Fig. 5. *Fluid transfer system*
1-capacity, 2-tank, 3,6,13-pipeline, 4-pump line, 5-valve, 7-air supply, 8-valve, 9-actuator, 10-spring, 11-way pipe, 12-ctuator, 14-electric sensor

Conclusion

As a consequence of the analysis of operational issues of centrifugal soil pumps for hydro abrasive mixture fluid transportation in ore-dressing and other enterprises, the main criteria's of soil pump components and main pipeline wear was established.

The following Innovative technologies for improvement of centrifugal soil pumps, with the use of modern physical and design solutions were proposed:

1) Reduction of hydro abrasive mixture flow in the impeller cavity that will reduce surface wear of impeller elements;
2) For pulp pumping - reduction of vibration influence both of hydro abrasive mixture and pump overall. That will reduce impeller components wear;
3) Slurry solids extraction prior to its inflow into the cavity of the impeller and its blades.

Literature

1. *Povetkin V. V., Lem V.P.* Hydroabrasive wear soil and Peskov of pumps//Messenger of KAZNTU. - Almaty, 2008. - No. 6(69). – pp. 51 – 54.

2. *Lem V.P.* Analysis of wear of surfaces of working details of soil pumps//International scientific and practical conference. Architecture and construction in the new millennium. - Almaty, 2008. – pp. 227-231.

3. *Povetkin V.V., Lem V.P.* Problem of a hydroerosion of working details of soil pumps//First international scientific and technical conference. New in machine-tool construction, materials science and the automated design of machine-building production, - Almaty, 2010. - Volume 1. – pp. 53-55

4. *Povetkin V.V., Lem V.P.* Soil pump. RK innovative patent No. 24120. Publ. 15.06.2011, bulletin No. 6.

5. *Povetkin V.V., Lem V.P.* Soil pump. RK innovative patent No. 23554. Publ. 15.12.2010, bulletin No. 12.

6. *Povetkin V.V., Ermekbayeva A.O., Kerimzhanova M.F., Andryushchenko E. S.* Device of the soil pump. RK innovative patent No. 30467. Publ. 15.10.2015, bulletin No. 10

7. *Povetkin V.V., Ermekbayeva A.O., Kerimzhanova M.F., Andryushchenko E.S.* Soil pump. RK innovative patent No. 30468. Publ. 15.10.2015, bulletin No. 10.

8. *Povetkin V.V., Kovalenko I.V., Kerimzhanova M.F., Tatybayev M.K.* Soil pump. RK innovative patent No. 28727. Publ. 15.07.2014, bulletin No. 7.

9. *Povetkin V.V., Lem V.P., Kerimzhanova M.F., Kovalenko I.V.* Soil pump. RK innovative patent No. 28600. Publ. 16.06.2014, bulletin No. 6.

10. *Ermekbayeva A. O., Alpeisov A.T. Povetkin V.B. Kerimzhanova M.F.* Pumping unit. RK innovative patent No. 28601. Publ. 16.06.2014, bulletin No. 6.

11. *Povetkin V.V. Kerimzhanova M.F., Andryushchenko E.S., Ibragimova Z.A.* Soil pump. RK innovative patent No. 29439. Publ. 25.12.2014, bulletin No. 1.

12. *Povetkin V.V., Kerimzhanova M.F., Povetkin A.V., Andryushchenko E.S.* Installation for pumping of liquid with solid inclusions. RK innovative patent No. 30949. Publ. 15.03.2016, bulletin No. 3.

KINETIC MODELS OF NICKEL LATERITE ORE LEACHING PROCESS

Petrovski A., Načevski G., Dimitrov A. T., Paunović P.
Faculty of Technology and Metallurgy –University Ss Cyril and Methodius, Skopje
Rudjer Bošković str., 16, R.N. Macedonia

pericap@tmf.ukim.edu.mk

Abstract: *The subject of this study is leaching process of nickel-bearing laterite ore from Ržanovo, R. Macedonia. The influence of sulfuric acid concentration (0.5, 1 and 3 M H2SO4) on the extracted Ni (%, wt.) was studied. The leaching process intensified by magnetic stirring at different temperatures (298, 323, 348 and 363 K) in the time interval of 120 min. was performed. The results were used for kinetic analysis of the leaching process. It was found that for 3 M H_2SO_4, the best fitting has shown the Jander and Ginstling-Braunshtein models, which point out that limiting step of the process is diffusion. Activation energy was calculated to be 42,67 kJ·mol^{-1} (Jander model) 40,28 kJ·mol^{-1} (Ginstling – Brousthein model), which confirm the diffusion controlled process.*

Keywords: NICKEL LATERITE ORE, LEACHING, KINETIC MODELS, ACTIVATION ENERGY

1. Introduction

Nickel is a silver white metal, with face centered cubic cell (FCC) showing good mechanical properties and corrosive resistance. Due to this, it is used as alloying element in steels as an austenitic stabilizer, forming variety of stainless steel with excellent mechanical properties [1, 2]. Nickel-bearing ores significant for industrial production are classified as sulfides and laterites (oxide) ores. Laterite ores are the major source of nickel (72 % of the reserves), much lower negative impact to environment and lower mining cost. But their contribution in the world's nickel production is only 42 % [3]. Industrial nickel production from laterite ores is based on both pyro- and hydrometallurgical processes. The pyrometallurgical processes are based on ferronickel smelting in the rotary kiln-electric furnace and nickel matte smelting. There are two main hydrometallurgical processes: high pressure acid leaching (HPAL) and the Caron process. HPAL technique needs expensive leaching aggregates – autoclaves, while in the Caron process, high-temperature reductive roasting is included before the leaching. Hydrometallurgical processes could be acid or alkaline [3].

This research work is focused on development of leaching method under atmospheric pressure (atmospheric leaching, AL). According to the periodic literature data, research studies of AL are oriented to use different acid solvents such as sulfuric acid [4], nitric acid [5], hydrochloric acid [6], acetic, citric and oxalic acid [7, 8]. The aim of this work is to optimize the AL process in sulphuric acid using magnetic stirring, with modeling the kinetic of the process at different temperatures.

2. Materials and methods

Ore

Low-grade nickel laterite ore from Ržanovo mining area in R. Macedonia was subject of leaching. It belongs to intermediate type Saprolitic ores (class C), with increased content of MgO (12–16 %, wt.) and Fe in the range of 25–33 %, wt.. Mechanical preparation of the ore with Ni content of 0.85 %,wt., was performed within the production line of the FENI INDUSTRI, Kavadarci. After sieving (0.200 mm, 0.104 mm, 0.074 mm, 0.043 mm and 0.037 mm) the major fraction with the highest content of Ni (0.92 %, wt.) was chosen for further study. Before the leaching, magnetic separation of this fraction was done in order to reduce the amount of Fe, and to increase the Ni content. Ni content was increased to 1.04 %, wt. According to the XRD analysis [9], dominant mineral is hematite (Fe_2O_3), while less, but considerable amount have shown talc ($Mg_3Si_4O_{10}(OH)_2$) and clinochlore ($(Mg_5Al)(Al,Si)_4O_{10}(OH)_8$). Quartz ($SiO_2$), magnetite ($Fe_3O_4$) and stilpnomelane ($Fe_2(Si_3O_9)$) have been shown as minor phases.

Leaching`

Sulfuric acid with different concentration (0.5, 1 and 3 M) was used as a solvent. The ratio of solid vs. liquid phase was 1:50 (5g ore in 250 ml aqueous solution 25 of H_2SO_4). The leaching was performed under atmospheric pressure, using magnetic stirring with 600 rpm, at different temperatures: 298, 323, 348 and 363 K. For each leaching experiment, the samples of 5 ml were taken at the following time interval: 15, 30, 60 and 120 minutes. Concentration of the leached Ni was determined by atomic absorption spectroscopy (AAS) using a spectrometer, model PinAAcle 900F (PINAACLE900F).

3. Results and discussions

Leaching process

The first step in the study of the nickel laterite ore leaching process was determination of the influence of solvent (H_2SO_4) concentration at the ambient temperature (298 K). In Fig. 1 is shown dependence of yield of the leached fraction (α) on the time. As can be seen, the yield of the leached fraction increases during the time. Diffusion region of the curve is not reached within the experimental time. Also, with the increasing of the solvent concentration, the maximum yield of the leached fraction increased from 16.37 % (wt.) in 0.5M H_2SO_4, 22 % in 0.5M H_2SO_4 to 28 % in 3M H_2SO_4.

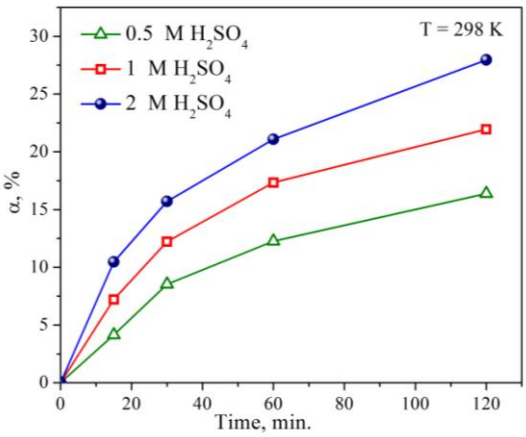


Fig. 1 *Diagram of yield of leached fraction (α) – time dependence for different concentrations of H_2SO_4 at 298 K.*

In Fig. 2, the dependence of the yield of the leached fraction (α) on the temperature is shown, for 3 M H_2SO_4. It is obvious that the temperature considerably intensifies the leaching process. After 120 minutes leaching in the 3 H_2SO_4, the yield of the leached fraction increased from 28 % at 298 K to 84 % at 363 K.

In Fig. 3, the change of the relative leaching rate (the yield of the leached fraction per time unit) during the experimental time is shown. During the time of leaching, as the yield of the leached fraction increases, the relative leaching rate decreases. The relative

leaching rate is higher at higher temperatures, but after 2 h, the leaching rates for all temperatures approach each other. At lower temperatures, the change of the relative leaching rate with time is slight, pointing out that the leaching process is limited by the chemical reaction. As the temperature of the process increases, the chemical reaction rate increases causing intensive change of the relative leaching rate indicating that reaction zone of the process occurs in the middle of the reacting ore particles. This points out on the diffusion control of the leaching process.

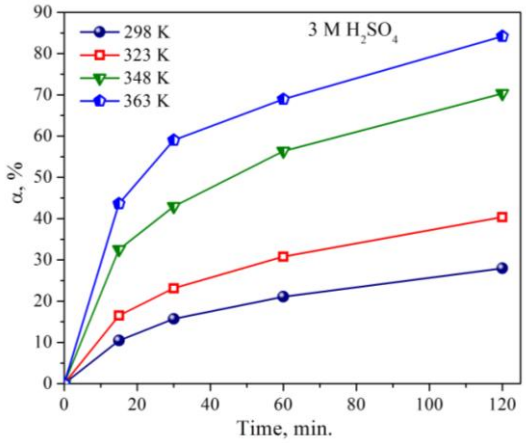


Fig. 2 *Diagram of yield of leached fraction α – time dependence for different temperatures in 3 M H_2SO_4.*

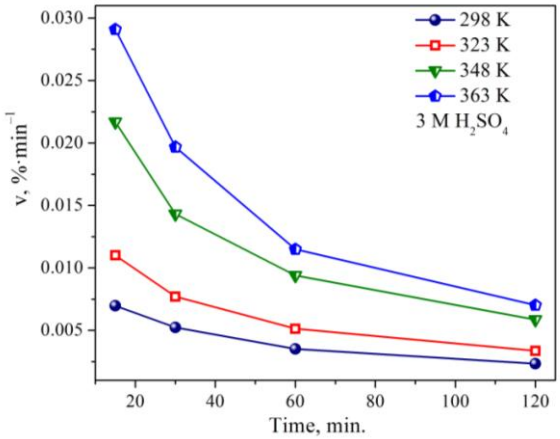


Fig. 3 *Diagram of relative leaching rate – time dependence for different temperatures in 3 M H_2SO_4.*

Kinetic models of the leaching process

The leaching process of nickel laterite ores can be expressed by the shrinking core model (Fig. 4), where the rate-determining step could be the chemical reaction on the core surface or diffusion process [10]. The model analysis was performed for leaching process in 3M H2SO4, at different temperatures (298, 323, 348 and 363 K).

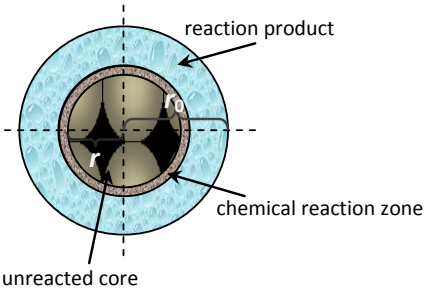


Fig. 4 *Schematic view of the shrinking core model: r_0- starting radius of the reacting ore particle; r- radius of the reacting ore particle after some time t.*

In the case when leaching process is limited by the chemical reaction, the process could be described by the Spenser-Topley-Kewan model [11]:

$$1-(1-\alpha)^{\frac{1}{3}} = k_S \cdot t$$

where α is yield of reacted fraction, k_S is Spenser-Topley-Kewan rate constant, defined by the following equation:

$$k_S = \frac{k \cdot C}{r_0 \cdot \rho}$$

where k is reaction rate constant, C is concentration of the solid reactant (ore particle), r_0 is a radius of the solid reactant, ρ is density of the solid reactant and t time of duration of the chemical reaction.

If the leaching process is limited by the diffusion, it can be described by the Ginstling-Braunshtein [12] or Jander model [13]. The Ginstling-Braunshtein model is given by the following equation:

$$1-\frac{2}{3}\cdot\alpha-(1-\alpha)^{\frac{2}{3}} = k_G \cdot t$$

where k_G is Ginstling-Braunshtein rate constant, defined as:

$$k_G = \frac{2 \cdot M \cdot D \cdot C}{a \cdot \rho \cdot r_0^2}$$

where M is molecular weight of the solid reactant, D is diffusion coefficient and a is a stoichiometric coefficient.

The Jander model is given by the following equation:

$$\left[1-(1-\alpha)^{\frac{1}{3}}\right]^2 = k_J \cdot t$$

where k_J is Jander rate constant, defined as:

$$k_G = \frac{2 \cdot S \cdot D \cdot K}{r_0^2}$$

where S is surface of the solid reactant layer and K is proportionality coefficient.

The experimental data from the diagram in Fig. 2 were included in the each model given above, and the corresponding straight-lines are shown in Fig. 5, 6 and 7, respectively.

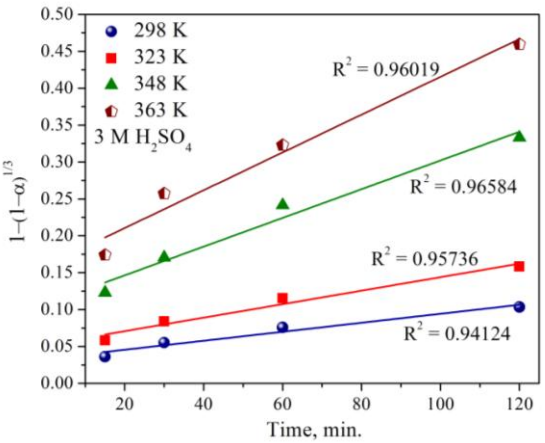


Fig. 5 *Linear fit of nickel leaching process in 3 M H_2SO_4 described by Spenser-Topley-Kewan model*

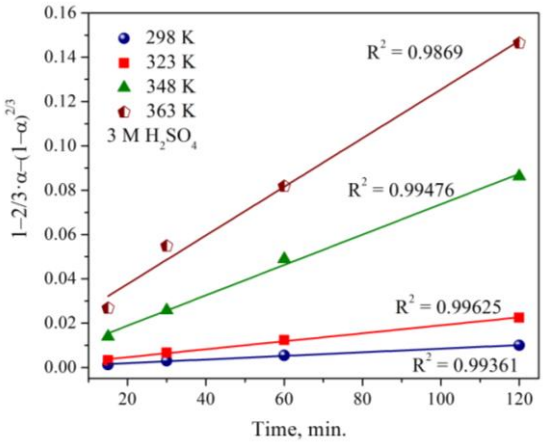


Fig. 6 *Linear fit of nickel leaching process in 3 M H_2SO_4 described by Ginstling-Braunshtein model*

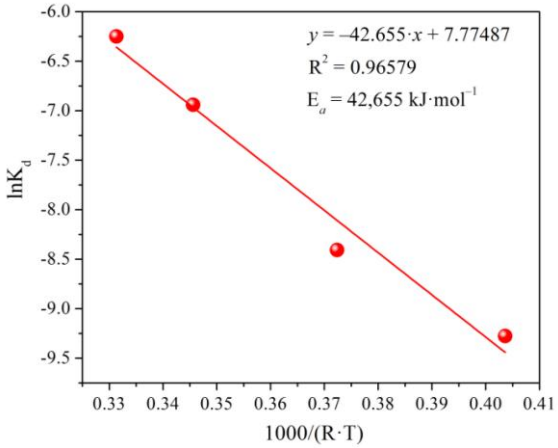


Fig. 8 *Arrhenius plots of nickel leaching processs in 3 M H_2SO_4 described by Jander model*

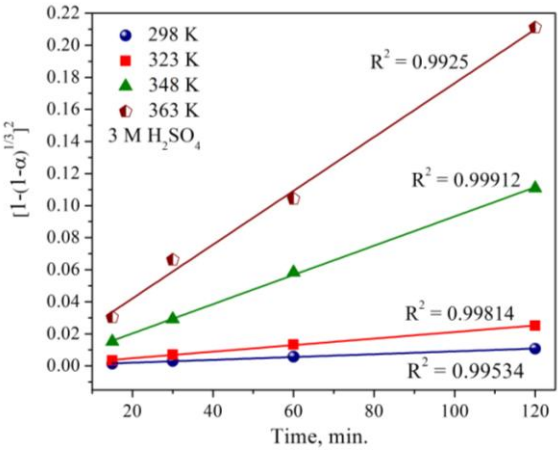


Fig. 7 *Linear fit of nickel leaching process in 3 M H_2SO_4 described by Jander model*

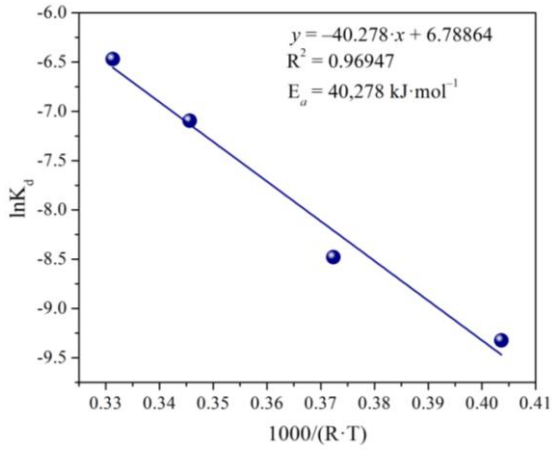


Fig. 9 *Arrhenius plots of nickel leaching processs in 3 M H_2SO_4 described by Ginstling-Braunshtein model*

It is obvious that diffusion-based models (Jander and Ginstling-Braunshtein) have shown much better fiting than the Spenser-Topley-Kewan model which assumes that the process is limited by the chemical reaction. The fitting of the Jander and Ginstling-Braunshtein models is very close, where Jander model describes the leaching process the best. This is an experimental proof that the leaching process of the nickel laterite ore is diffusionally controlled.

Activation energy analysis

Using the Arrhenius equation:

$$\ln k = -\frac{E_a}{R \cdot T} + \ln A$$

where k could be be Jander (k_J) or Ginstling-Braunshtein (k_G) rate constant, R is universal gas constant, T is temperature, A is the Arrhenius constant and E_a is an activation energy of the leaching process. E_a can be determined by further derivation of the previous experimental data and results with Arrhenius equation. The corresponding calculated values are shown in Fig. 8 and Fi. 9, for Jander and Ginstling-Braunshtein model, respectively. The calculated values of Ea of 42.65 kJ·mol^{-1} (by Jander model) and 40.28 kJ·mol^{-1} (by Ginstling-Braunshtein model) are in good mutual agreement, but also in good agreement with the literature data for activation energies characteristic for diffusion controled leaching processes [14-16].

4. Conclusions

According to the above presented results, we can draw the follow conclusions:

1. Increase of the temperature and concentration of the solvent (H_2SO_4) significantly intensifies the leaching process intenisfied with magnetic stirring.

2. The leaching process in 3M H_2SO_4 in the whole studied temperature range is the best described by Jander and Ginstling-Braunshtein model , which points out that the leaching process is diffusionally controled.

3. Activation energy for nickel laterite ore leaching process in 3M H_2SO_4 was determined to be 42.65 kJ·mol^{-1} (by Jander model) and 40.28 kJ·mol^{-1} (by Ginstling-Braunshtein model),which is in good agreement with similar leaching processes diffusionally controled.

References

[1] J.R. Davis (ed.) (2000) ASM Specialty Handbook: Nickel, Cobalt, and Their Alloys, ASM International®.

[2] F. Habashi (1997) Handbook of Extractive Metallurgy, Volume 1, WILEY-VCH.

[3] A. D. Dalvi, W. G. Bacon; R. C. Osborne (2004) PDAC 2004 International Convention,Trade Show & Investors Exchange.

[4] R.G. McDonald, B.I. Whittington (2008) Atmospheric acid leaching of nickel laterites review Part I. Sulphuric acid technologies, Hidrometallurgy, Vol. 91, p. 35-55.

[5] R.G. McDonald, B.I. Whittington (2008) Atmospheric acid leaching of nickel laterites review. Part II. Chloride and bio-technologies, Hidrometallurgy, Vol. 91 p. 56-69.

[6] B. Ma, C. Wang, W. Yang, B. Yang, Y. Zhang (2013) Selective Pressure Leaching of Fe (II)-rich Limonitic Laterite Ores from Indonesia Using Nitric Acid, Miner. Eng., Vol. 45, p. 151-158.

[7] S. Sahu, N. C. Kavuri, M. Kundu (2011) Dissolution kinetics of nickel laterite ore using different secondary metabolic acids, Braz. J. Chem. Eng., Vol. 28, p. 251-258.

[8] A. Pawlowska, Z. Sadowski (2017) Influence of chemical and biogenic leaching on surface area and particle size of laterite ore, Physicochem. Probl. Miner. Process., Vol. 53, p. 869-877.

[9] P. Paunović, G. Načevski, A. Petrovski, A. Tomova, A. Grozdanov, A. T. Dimitrov (2019) Kinetic analysis of ultrasound leaching of nickel laterite ore, Bul. Chem, Com., Volume 51, Special issue D, p.12-18.

[10] O. Levenspiel (1999) Chemical Reaction Engineering, John Wiley & Sons, Inc., New York.

[11] W. D. Spenser, B. Topley (1929) Chemical kinetics of the system $Ag_2CO_3 \rightleftharpoons Ag_2O + CO_2$, J. Chem. Soc., Vol. 27, p. 2633-2650.

[12] A. M. Ginstling, B. I. Braunshtein (1950) Concerning the diffusion kinetics of reaction in spherical particles, J. Appl. Chem. USSR, Vol. 23, p. 1327-1338.

[13] W. Jander (1927) Reaktionen im festen Zustande bei höheren Temperaturen. Reaktionsgeschwindigkeiten endotherm verlaufender Umsetzungen, Z anorg allg Chem (in German) Vol. 163 p. 1-30.

[14] G. Rinn, F. Fetting (1982) The leaching of a serpentinite with hydrochloric acid, Erzmetall, Vol. 35, p. 432-436.

[15] S. Stopić, B. Friedrich, R. Fuchs (2003) Sulphuric Acid Leaching of the Serbian Nickel Lateritic Ore, Erzmetall, Vol. 56, p. 198-203.

[16] T. Agacayak, V. Zedef (2012) Dissolution kinetics of a lateritic nickel ore in sulphuric acid medium, Acta Montanistica Slovaca, Vol. 17, p. 33-41.

OPTIMIZATION OF CUTTING PARAMETERS FOR MINIMIZING SPECIFIC CUTTING ENERGY AND MAXIMIZING PRODUCTIVITY IN TURNING OF AISI 1045 STEEL

Assis. Prof. Sredanović B. PhD.[1], Asoc. Prof. Čiča Đ. PhD.[1], M.Sc. Tešić S.[1], Asoc. Prof. Kramar D. PhD[2]
University of Banjaluka, Faculty of Mechanical Engineering, Bosnia and Herzegovina [1]
University of Ljubljana, Faculty of Mechanical Engineering, Slovenia [2]

branislav.sredanovic@mf.unibl.org

Abstract: *This paper presents an experimental study related to the optimization of cutting parameters in roughing turning of AISI 1045 steel under flooded conditions. The aim is to find a suitable combination of cutting parameters (cutting speed, depth of cut and feed rate) that minimize specific cutting energy and maximize material removal rate. The machining experiments were performed based on the Taguchi L27 full-factorial orthogonal array and response surface methodology (RSM) has been used to obtain the regression model for the specific cutting energy and material removal rate. Analysis of variance (ANOVA) was used to find out the significance of each cutting parameter. Finally, the developed models were interfaced with an artificial bee colony (ABC) to determine the optimal set of cutting parameters.*

Keywords: CUTTING PARAMETERS, TURNING, OPTIMIZATION

1. Introduction

In the last decade, energy related issues has been point of interest in miscellaneous manufacturing industries. In the metal cutting industry, energy consumption is an important metric in sustainability analysis since reducing energy consumption of machine tools can significantly improve the environmental performance of manufacturing processes and systems [1]. Thus, significant research has been conducted to study the energy consumption in machining with purpose to achieve sustainable manufacturing [2]. The turning is one of the most extensively used machining methods in modern manufacturing industry and many researchers have investigated realization of energy savings via parameter optimization. Aggarwal et al. [3] optimized power consumption in turning of AISI P-20 tool steel under different cutting environments. Neugebauer et al. [4] investigated the effects of cutting tool materials and geometry on the energy efficiency of hard turning processes. Guo et al. [5] optimize the energy consumption and the surface roughness in dry turning of steel and aluminum. Velcev et al. [6] devised an equation for determining the optimum cutting speed by applying the minimum energy criterion. Hanafi et al. [7] simultaneously optimized power consumption and surface quality in turning using TiN coated tools under dry conditions. Rajemi et al. [8] optimized the total energy of the turning process to derive an economic tool life. Camposeco-Negrete [9] determined the optimal levels of the turning parameters that lead to minimum energy consumption and minimum surface roughness. Bagaber and Yusoff [10] optimized machining parameters, including power consumption and the traditional quality characteristics of surface roughness and tool wear during the turning of AISI 316 under dry conditions. Suresh et al. [11] optimized cutting force, power, specific cutting force, tool wear and surface roughness in dry turning using coated carbide tool. Bhushan [12] simultaneously optimize energy consumption and tool life during turning of metal matrix composites. Park et al. [13] optimize the machining parameters of the turning process for hardened AISI 4140 steel to improve energy efficiency.

Growing energy demand push manufacturing industries to search for high energy efficiency and low cost solutions. At the same time, these industries are incessantly challenged for obtain higher productivity in order to continue to be competitive. Therefore, optimization of machining parameters is crucial to achieve sustainable and economic manufacturing processes. Nowadays, the optimization techniques based on artificial intelligence are becoming more popular in various engineering areas. In this paper, the artificial bee colony (ABC) algorithm, which mimics the intelligent foraging behavior of honey bees algorithm is employed to solve the parameter optimization problem of turning process. The specific cutting energy (SCE) and material removal rate (MRR) were selected as objective functions.

2. Experimentation

In order to observe the degree of influence of three process parameters including cutting speed, depth of cut and feed rate three levels of each factors were considered, and an L_{27} orthogonal array was selected. The selected parameters are listed in Table 1, along with their applicable units, symbols, and values.

Table 1: *Parameters, units, symbols, and level values used for the orthogonal array.*

Parameters	Unit	Symbol	Level 1	Level 2	Level 3
Cutting speed	[m/min]	v_c	210	320	400
Depth of cut	[mm]	a	1.5	2.0	2.5
Feed rate	[mm/rev]	f	0.224	0.280	0.355

Turning experiments have been carried out on the universal lathe VDF Boehringer Prvomajska. All the machining tests were realized under flooded conditions using cutting fluid with a 3% emulsion of vegetable oil. In this investigation, the workpiece material was the Ck45E (AISI 1045) carbon steel of diameter 150 mm and SUMITOMO SNMG 1204 08 NMX carbide cutting tool was used. The cutting forces are measured with a three component dynamometer Kistler 9259A.The measurement chain also includes a charge amplifier (Kistler 5001), a spectrum analyzer (HP3567A), and a personal computer for data acquisition and analysis.

At present, due to an easy concept to understand and calculate, most studies use specific cutting energy (*SCE*) to express energy efficiency of the machining processes. *SCE* is defined as the energy consumed to remove a unit volume of material and it is one of the best ways of quantitatively measuring the efficiency of the metal cutting process or the machinability of a workpiece [14]. The specific cutting energy was computed from the main cutting force and turning parameters by using following equation:

$$\mathrm{SCE} = \frac{P_c}{a \cdot f \cdot v_c} = \frac{F_c \cdot v_c}{a \cdot f \cdot v_c} \tag{1}$$

where P_c, F_c, a, f, and v_c represent the cutting power, main cutting force, depth of the cut, feed rate, and cutting speed, respectively.

The most common indicator of productivity of the metal cutting processes is material removal rate (*MRR*). The values of these two performance characteristic are given in Table 2.

Table 2: *Experimental data and results for specific cutting energy and material removal rate.*

Exp. No.	Process parameters			Responses	
	v_c [m/min]	a [mm]	f [mm/rev]	SCE [J/mm³]	MRR [cm³/min]
1.	210	1.5	0.224	2395.8	70.6
2.	210	1.5	0.280	2247.6	88.2
3.	210	1.5	0.355	2170.9	111.8
4.	210	2	0.224	2272.3	94.1
5.	210	2	0.280	2078.6	117.6
6.	210	2	0.355	2067.6	149.1
7.	210	2.5	0.224	2208.9	117.6
8.	210	2.5	0.280	2027.1	147
9.	210	2.5	0.355	2066.5	186.4
10.	320	1.5	0.224	2375	107.5
11.	320	1.5	0.280	2214.3	134.4
12.	320	1.5	0.355	2187.8	170.4
13.	320	2	0.224	2207.6	143.4
14.	320	2	0.280	2030.4	179.2
15.	320	2	0.355	2043.7	227.2
16.	320	2.5	0.224	2162.5	179.2
17.	320	2.5	0.280	2008.6	224
18.	320	2.5	0.355	1993.2	284
19.	400	1.5	0.224	2297.6	134.4
20.	400	1.5	0.280	2188.1	168
21.	400	1.5	0.355	2157.7	213
22.	400	2	0.224	2192	179.2
23.	400	2	0.280	2028.6	224
24.	400	2	0.355	2035.2	284
25.	400	2.5	0.224	2133.9	224
26.	400	2.5	0.280	1972.9	280
27.	400	2.5	0.355	1969.6	355

3. Artificial bee colomy alogrithm

Artificial bee colony (ABC) algorithm was initially proposed by Karaboga [15]. This algorithm is inspired by the intelligent foraging behavior of honey bees. Similar to the concept of other evolutionary algorithms such as particle swarm optimization (PSO) and ant colony optimization (ACO), this algorithm is capable of tracing good quality of solutions. In the ABC algorithm, there are three types of bees: employed bees, onlooker bees, and scout bees. Each type of bee bears a different task. The employed bees exploit the food source and share this information with onlooker bees. The onlooker bees tend to select good food sources according to the probability proportional to the quality of that food source. Whenever a food source is exploited fully, that food source is called off and all the employed bees corresponding to that food source abandon it and become scout. The scout bee then performs exploration procedure and random exploitation search with purpose to find a new food source.

In the ABC algorithm the initial population is generated by using a random approach. Let $X_i = \{x_{i,1}, x_{i,2}, ..., x_{i,D}\}$ represent the i-th food source in the population, where D is the dimension size. In order to produce a new candidate solution $V_i = \{v_{i,1}, v_{i,2}, ..., v_{i,D}\}$ the ABC uses the following equation:

$$v_{i,j} = x_{i,j} + \phi_{i,j}\left(x_{i,j} - x_{k,j}\right) \quad (2)$$

where $k \in \{1, 2, ..., SN\}$and $j \in \{1, 2, ..., D\}$ are randomly chosen indexes ($k \neq j$), SN is the number of food sources which is equal to the number of employed bees or onlooker bees and $\Phi_{i,j}$ is a random number in the range [-1, 1].

In onlooker bee phase, apply greedy selection between v_i and x_i, and compute the probabilities of winning food sources using the following expression:

$$p_i = \frac{fit_i}{\sum_{n=1}^{SN} fit_n} \quad (3)$$

where fit_i is the fitness value of the i-th solution which is proportional to the nectar amount of the food source in the position i. As seen, the better the solution i, the higher the probability of the i-th food source selected.

If a food source cannot be further improved over a predefined number (limit cycles), then the food source abandoned. Assume that the abandoned source is X_i and $j \in \{1, 2, ..., D\}$,then the scout discovers a new food source to be replaced with X_i. This operation can be defined as in Eq. (4).

$$x_{i,j} = x_{\min,j} + \text{rand}(0,1)\left(x_{\max,j} - x_{\min,j}\right) \quad (4)$$

where rand(0, 1) is a random number within [0, 1] based on a normal distribution and $x_{\min,j}$ and $x_{\max,j}$ are lower and upper boundaries for the dimension j, respectively.

4. Results and discussion

Prior to the optimization process, it is obligatory to determine a relationship between machining parameters and objective functions. In this study response surface methodology was applied to correlate considered machining parameters (cutting speed, depth of cut and feed rate) with *SCE* and *MRR* in form of reduced quadratic model. A variance analysis of the specific cutting energy and material removal rate was made with the objective of analyzing the influence of cutting speed, depth of cut and feed rate on the results. For the case of *SCE* the regression equation of the fitted model is given by Eq. (5), where the most significant parameters have been included from the results obtained from the regression analysis (α = 0.05). The model *F*-value of 184.37 implies the model is significant. There is only a 0.01% chance that a "model *F*-value" this large could occur due to noise. *P*-values smaller than 0.05 indicate model terms that are significant. The *R*-squared statistic indicates that the model as fitted explains 97.77% of the variability in *R*. The adjusted R-squared statistic, which is more suitable for comparing models with different numbers of independent variables, was 97.24%. Signal to noise ratio of developed model was 45.5.

$$Y_u(SCE)=5412.4-0.327\cdot v_c-958.1\cdot a-13350\cdot f+192.5\cdot a^2+20781.2\cdot f^2 \quad (5)$$

The mathematical relationship obtained for analyzing the influences of the various dominant machining parameters on the material removal rate criteria is given by Eq. (6). The model *F*-value of 5275.19 implies the model is significant. *P*-values smaller than 0.05 indicate model terms that are significant. The *R*-squared statistic indicates that the model as fitted explains 99.94% of the variability in *R*. For MRR model, the adjusted R-squared statistic was 99.92%, while signal to noise ratio was 275.59.

$$Y_u(MMR)=177.5-0.573\cdot v_c-88.8\cdot a-620\cdot f+0.286\cdot v_c\cdot a+2\cdot v_c\cdot f+2\cdot a\cdot f \quad (6)$$

The Eqs. (5) and (6) were used to test the accuracy of the developed RSM-based models using the experimental data of full

factorial design. The comparison of the predicted and the experimental values of *SCE* and *MRR* for the experimental data during turning of C45E carbon steel of is shown in Fig. 1.

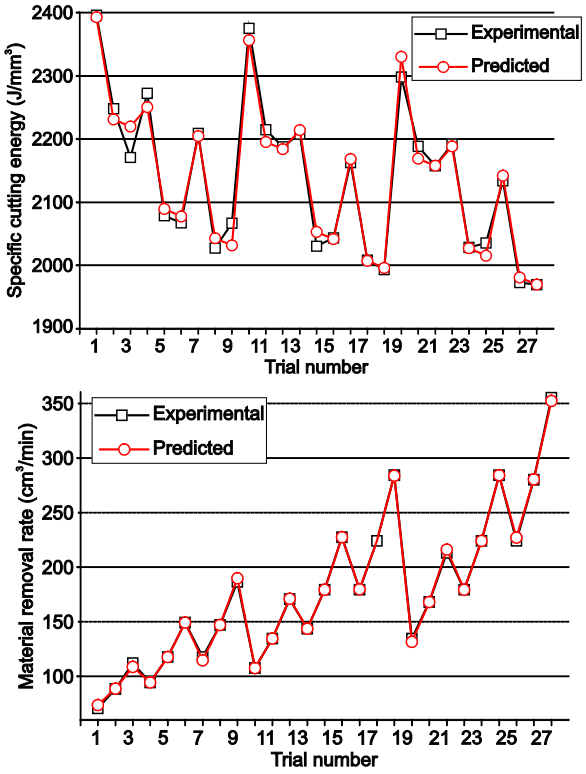


Fig. 1 *Comparison of experimental and predicted values of specific cutting energy (above) and material removal rate (below)*

The optimization problem in this study was solved by coupling the RSM specific cutting energy and material removal rate models with the artificial bee colony (ABC) algorithm. The optimization model can be expressed by the following mathematical problem:

Find: $X = [v_c, a, f]$
Minimize: $F(X)$
Subject to: $v_{cmin} \le v_c \le v_{cmax}$, $a_{min} \le a \le a_{max}$, $f_{min} \le f \le fmax$.

In this research, the turning process required qualities is that specific cutting energy must be kept small whereas the material removal rate have to be maximized as possible. Therefore, these two performance characteristics resulting a two-objective optimization problem, i.e., minimizing specific cutting energy and maximizing material removal rate. For multi-objective optimization of these two responses, the following objective function is developed:

$$Min(X) = \frac{w_1 \cdot Y_u(SCE)}{SCE_{min}} - \frac{w_2 \cdot Y_u(MRR)}{MRR_{max}} \quad (7)$$

where w_1 and w_2 are the weight values assigned to *SCE* and *MRR*, respectively, SCE_{min} is the minimum value of *SCE*, and MRR_{max} is the maximum value of *MRR*. These minimum and maximum values of the responses are obtained from the experimental results. The weight values can be anything provided that $w_1 + w_2 = 1$ and it depends on the priorities of the considered responses as set by the process engineers. Here, equal weights for all the responses are considered, i.e. $w_1 = w_2 = 0.5$. In the ABC optimization process, the commonly used ABC operation parameters were adopted, namely the population number and the maximum evaluation number, were set as 80 and 4000, respectively. Apart from common parameters, the basic ABC algorithm utilized in this paper employs only one control parameter, which is called limit. A food source is assumed to be abandoned when limit is exceeded for the source. In this study, Eq. (8) define the limit value in terms of the population size (*SN*) and dimension of the problem (*D*):

$$limit = SN \cdot D \quad (8)$$

The minimum value of the objective function ($X = 0.0043$) is obtained for ABC algorithm. The ABC optimization approach results show that the best combination process parameters values for simultaneously optimizing specific cutting energy and material removal rate using the proposed fitness function was: 400 m/min, 2.5 mm and 0.355 mm/rev, for cutting speed, depth of cut and feed rate, respectively. This process parameters optimal combination corresponds to: *SCE* = 1969.5 J/mm^3 and *MRR* = 355 cm^3/min.

5. Conclusions

This study concerns an experimental and optimization study of turning of C45E carbon steel (42 HRC) with a carbide cutting tool. In order to economically obtain the quality characteristics, the experiments, based on Taguchi's L_{27} orthogonal array, were carried out to study the effect of various machining parameters, namely, cutting speed, depth of cut and feed rate on specific cutting energy and the material removal rate. A reliable models for these two performance characteristics were developed using response surface methodology. Analysis of variance was used to find out the significance of each cutting parameter. The elaborated RSM models were interfaced with an ABC algorithm to find the optimum process parameter values. The optimum combinations of input parameters, minimum specific cutting energy and maximum material removal rate were obtained.

References

[1] Vijayaraghavan, A., Dornfeld, D., Automated energy monitoring of machine tools. CIRP Annals - Manufacturing Technology, Vol. 59, 2010, pages 21-24.

[2] Zhao, G.Y., Liu, Z.Y., He, Y., Cao, H.J., Guo, Y.B., Energy Consumption in Machining: Classification, Prediction, and Reduction Strategy, Energy, Vol. 133, 2017, pages142-157.

[3] Aggarwal, A., Singh, H., Kumar, P., Singh, M., Optimizing power consumption for CNC turned parts using response surface methodology and Taguchi's technique – A comparative analysis, Journal of Materials Processing Technology, Vol. 200, No. 1-3, 2008, pages 373-384.

[4] Neugebauer, R., Schubert, A., Reichmann, B., Dix, M., Influence Exerted By Tool Properties on the Energy Efficiency during Drilling and Turning Operations, CIRP Journal of Manufacturing Science and Technology, Vol. 4, No. 2, 2011, pages 161-169.

[5] Guo, Y., Loenders, J., Duflou, J., Lauwers, B., Optimization of Energy Consumption and Surface Quality in Finish Turning, Procedia CIRP, Vol. 1, 2012, pages 512-517.

[6] Velchev, S., Kolev, I., Ivanov, K., Gechevski, S., Empirical models for specific energy consumption and optimization of cutting parameters for minimizing energy consumption during turning, Journal of Cleaner Production, Vol. 80, 2014, pages 139-149.

[7] Hanafi, I., Khamlichi, A., Cabrera, F.M., Almansa, E., Jabbouri, A., Optimization of cutting conditions for sustainable machining of PEEK-CF30 using TiN tools, Journal of Cleaner Production, Vol. 33, 2012, pages 1-9.

[8] Rajemi, M., Mativenga, P., Aramcharoen, A., Sustainable machining: selection of optimum turning conditions based on minimum energy considerations, Journal of Cleaner Production, Vol. 18, 2010, pages1059-1065.

[9] Camposeco-Negrete, C., Optimization of cutting parameters for minimizing energy consumption in turning of AISI 6061 T6 using Taguchi methodology and ANOVA, Journal of Cleaner Production, Vol. 53, 2013, pages195-203.

[10] Bagaber, S.A., Yusoff, A.R., Multi-objective optimization of cutting parameters to minimize power consumption in dry turning of stainless steel 316, Journal of Cleaner Production, Vol. 157, 2017, pages 30-45.

[11] Suresh, R., Basavarajappa, S., Samuel, G.L., Some studies on hard turning of AISI 4340 steel using multilayer coated carbide tool, Measurement, Vol. 45, No. 7, 2012, pages 1872-1884.

[12] Bhushan, R.K., Optimization of cutting parameters for minimizing power consumption and maximizing tool life during machining of Al alloy SiC particle composites, Journal of Cleaner Production, Vol. 39, 2013, pages 242-254.

[13] Park, H-S., Nguyen, T-T., Dang, X-P., Multi-Objective Optimization of Turning Process of Hardened Material for Energy Efficiency, International Journal of Precision Engineering and Manufacturing, Vol. 17, No. 2, 2016, pages 1623-1631.

[14] Sarwar, M., Persson, M., Hellbergh, H., Haider, J., Measurement of specific cutting energy for evaluating the efficiency of band sawing different workpiece materials, International Journal of Machine Tools and Manufacture, Vol. 49, No. 12-13, 2009, pages 958-965.

[15] Karaboga, D., An idea based on honey bee swarm for numerical optimization, Technical Report TR06, 2005, Erciyes University, Kayseri, Turkey.

ENERGY HEAT EXCHANGE IN THE ZONE OF CONTACT OF THE PROBE OF AN ATOMIC FORCE MICROSCOPE WITH THE SURFACE UNDER STUDY

ЕНЕРГЕТИЧНИЙ ТЕПЛООБМІН В ЗОНІ КОНТАКТУ ЗОНДА АТОМНО-СИЛОВОГО МІКРОСКОПА З ДОСЛІДЖУВАНОЇ ПОВЕРХНЕЮ

Andriienko O., Ralchenko S., Doctor of Science Bondarenko M., PhD Bondarenko Yu.
Faculty of Electronically Technologies and Robotics
Cherkassy State Technological University, Ukraine

Abstract: *The article studies the mechanisms of energy exchange and transformations, which occur in a measuring instrument (probe) of an atomic force microscope (AFM) in the process of studying solid surfaces of materials. Mathematical modeling of the heating process of individual elements of the measuring unit of the atomic force microscope at the preparatory, final stages and the scanning stage of the surface under study was carried out. At the same time, such energy components of the processes occurring in the AFM control unit were taken into account. By minimizing the factors (heat dissipation due to friction of the probe on the surface), which negatively affect both the results of the monitoring and the condition of the probe and the surface, stable operation modes of the AFM are established. The solution of the equivalent thermal scheme of an atomic force microscope is presented, which confirms the adequacy of the mathematical models obtained.*

KEYWORDS: ATOMIC FORCE MICROSCOPE, ENERGY HEAT EXCHANGE, HEAT LOSSES, MATH MODELING, EQUIVALENT THERMAL SCHEME

1. Introduction

Among the main analytical methods for studying the state of the surface and physico-mechanical properties, method of atomic force microscopy, of course, has significant advantages: high spatial resolution, efficiency, accuracy and objectivity [1-3].

At the same time, despite the obvious advantages of the method, the accuracy and adequacy of the results of the study of some nanostructured coatings and materials by atomic force microscopy (AFM) is questionable. This is due both to the wrong choice of research modes, and to external power and energy factors of interaction of the sensitive AFM element with the surfaces of these materials [4, 5].

Some attempts to carry out calculations and modeling of both power and energy factors were carried out by a number of both domestic and foreign scientists, such as: Suslov A., Garishin O., Konstantinov V., Chizhik S., Sviridova O., Moya S. and other [5-7]. However, the results of such modeling, which are given in the works of these scientists, have low accuracy and, in general, make it impossible to carry out operational calculations directly in the process of experimental research.

At the same time, if the factors of force interaction can be experimentally confirmed, the experimental confirmation of the mechanisms of energy heat exchange taking place in the measuring instrument (probe) of an atomic force microscope in the process of studying solid surfaces of materials is currently impossible.

Therefore, it is relevant to study these phenomena is a mathematical modeling of the heating process of individual elements of the measuring unit of an atomic force microscope.

The purpose of this work is to study the mechanisms of energy heat exchange in the zone of contact of the probe of an atomic force microscope with the surface under investigation by applying mathematical modeling techniques and their subsequent confirmation by the method of equivalent thermal scheme.

2. The modeling results and their discussion

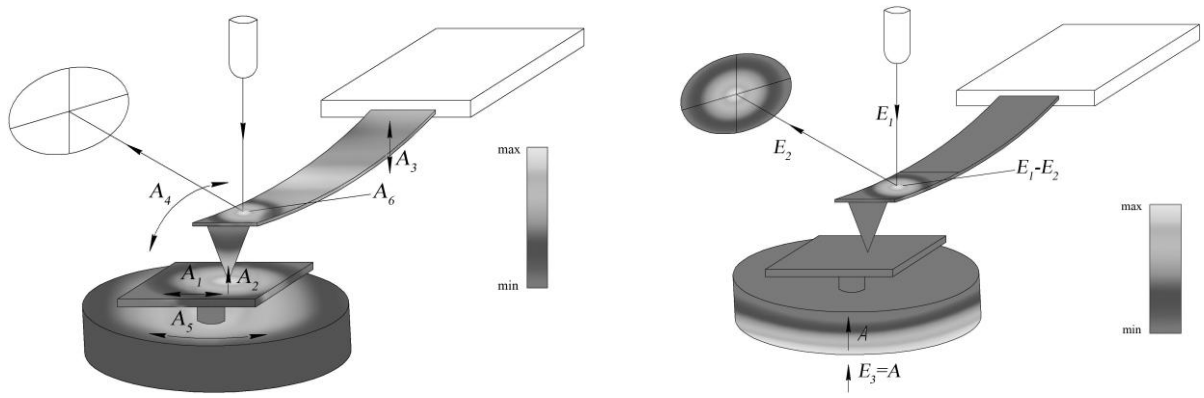
The measuring unit of an atomic force microscope «NT-206» (manufacturer Microtestmachines Co., Belarus) was chosen as an object for modeling energy heat exchange, namely the systems: «cantilever → probe → object under study ← piezo scanner» and «laser positioner → probe → photo detector».

The simulation of the interaction of these systems consisted in the compilation of an adequate energy scheme of the device operation. At the same time, the main energy parameters of the scheme were divided into two groups: heat losses and energy impact.

Among the heat losses, the costs for mechanical friction of the probe over the surface under study, costs for the action of electromagnetic fields and electric charge in the sensor's coverage area, costs for bending and torsion of the cantilever during the scanning process and costs for the piezo scanner result from the device operation should be highlighted.

At the same time, the energy impact in the scanning area of the AFM is divided into: radiation energy, which is generated by the laser positioner and sent to the AFM cantilever, laser energy, which is reflected from the cantilever and sent to the photodetector, the energy that drives the piezoscanner, and also the useful work of the piezoscanner. It should be noted that the difference between the energy of the radiation generated by the laser positioner and the energy that is sent to the photodetector is almost completely converted to heat, which heats the cantilever.

For modeling, the energy scheme of the measuring unit of the AFM was proposed, which allowed determining the mechanism of thermal exchange between the individual elements of the measuring unit of the device (Fig.1).



a. b.

Fig.1. Energy scheme of the measuring unit of the atomic force microscope:

Heat losses (a): A_1 – on the mechanical friction of the probe on the test surface; A_2 – on the action of electromagnetic fields and electric charge; A_3 – on the cantilever bending; A_4 – on the cantilever torsion; A_5 – on the piezo scanner torsion.

Energy impact (b): E_1 – laser positioner radiation energy; E_2 – laser energy incident on a photo detector; E_3 – the energy that drives the piezoscanner; A – useful work piezo scanner

In the process of thermal calculations, a number of mathematical models of the heating process of individual elements of the AFM were compiled and analytically solved using the inverse Fourier transform method. In this case, only heat exchange of heat transfer was taken into account (neither convective nor ray types of heat exchange were considered due to their irrelevance).

The basis of thermal calculations laid the equation of heat balance between the individual elements of the AFM [6]:

$$\begin{cases} (r,t)=\left\{T_0^{\nu+1}+\dfrac{(\nu+1)q_{n0}R}{\lambda_0}\times\left[\dfrac{3a_0^2t}{10R^2}-\sum\limits_{n=1}^{\infty}\dfrac{2R\sin\left(\mu_n\dfrac{r}{R}\right)}{\mu_n^3\cos(\mu_n)R}e^{-\left(\frac{\mu_n a_0}{R}\right)^2 t}\right]\right\} & (1)\\ (z,t)=\left\{T_0^{\nu+1}+\dfrac{(\nu+1)q_{n0}a_0}{\sqrt{\pi}\lambda_0}\int\limits_0^t\dfrac{e^{-\frac{z^2}{4a_0^2(t-\tau)}}}{\sqrt{t-\tau}}d\tau\right\}^{\frac{1}{\nu+1}} & (2)\\ (z,t)=\left\{T_0^{\nu+1}+\dfrac{(\nu+1)q_{n0}}{\lambda_0}\times\left[\dfrac{a_0^2t}{H}+\dfrac{3z^2-H^2}{6H}+\dfrac{2H}{\pi^2}\times\sum\limits_{n=1}^{\infty}(-1)^{n+1}\dfrac{\cos\left(\dfrac{\pi nz}{H}\right)}{n^2}e^{-\left(\frac{\pi a_0 n}{H}\right)^2 t}\right]\right\}^{\frac{1}{\nu+1}} & (3)\\ T(r,z,t)=\left\{T_0^{\nu+1}+\dfrac{(\nu+1)}{4\pi\lambda_0}\int\limits_0^{+\infty}\left(1-\dfrac{r^2\xi^2}{4}+\dfrac{r^4\xi^4}{64}-\dfrac{r^6\xi^6}{2304}\right)\times\right. & \\ \left[p_{01}\left(1-\dfrac{R_1^2\xi^2}{8}+\dfrac{R_1^4\xi^4}{192}-\dfrac{R_1^6\xi^6}{9216}\right)+p_{02}\left(1-\dfrac{\xi^2}{8}\left(R_2^2-R_1^2\right)+\dfrac{\xi^4}{192}\left(R_2^2-R_1^2\right)-\dfrac{\xi^6}{9216}\left(R_2^2-R_1^2\right)\right)\right]\times & (4) \end{cases}$$

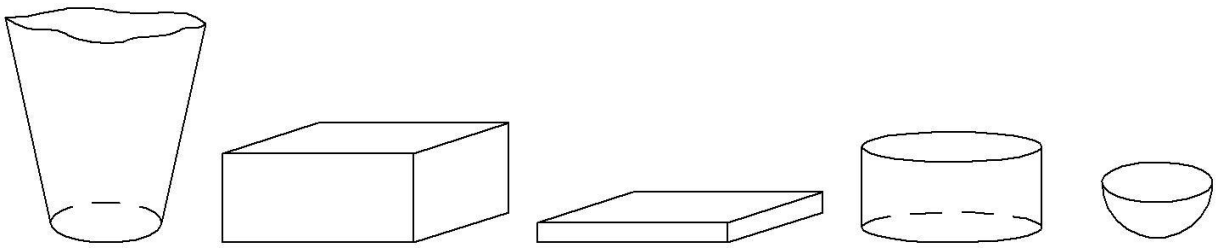
$$\times\left[e^{-z\xi}\left(1-erf\left(\frac{z}{2a_0\sqrt{t}}-\xi a_0\sqrt{t}\right)\right)-e^{-z\xi}\left(1-erf\left(\frac{z}{2a_0\sqrt{t}}+\xi a_0\sqrt{t}\right)\right)\right]d\xi\Bigg\}^{\frac{1}{\nu+1}}$$

$$T(r,t)=\left\{T_0^{\nu+1}+\frac{(\nu+1)q_{n0}R}{\lambda_0}\times\left(\frac{3a_0^2t}{10R^2}-\sum_{n=1}^{\infty}\frac{2R\sin\left(\mu_n\frac{r}{R}\right)}{\mu_n^3\cos(\mu_n)R}e^{-\left(\frac{\mu_n a_0}{R}\right)^2 t}\right)\right\} \quad (5)$$

Here, T_0 – model initial temperature, K; ν - empirical coefficient, q_{n0} – external heat flux, Вт/м2; r, R – радіуси вістря та основи зонда відповідно, м; λ_0 – коефіцієнт теплопровідності, W/m·K; a_0 – coefficient of thermal diffusivity, m^2/s; t – heat exposure time, s; ξ – the variable of layer thickness is heated, m; z – probe penetration depth, m; H – plate thickness, m; p_{01}, p_{02} – power sources of thermal exposure, W.

Each of the equations of the above system (1) - (5) is the heating equation for certain elements of the measuring unit of an atomic force microscope, the computational models of which are shown in Fig. 2:

- heating equation of a cut cone element (probe): Fig. 2 – a, (1);
- heating equation of a plate of small thickness (sample): Fig. 2 – b, (2);
- heating equation of a plate of small thickness (cantilever): Fig. 2 – c, (3);
- heating equation of the end surface of a cylinder (piezoscanner): Fig. 2 – d, (4);
- heating equation of spherical element segment (probe tip): Fig. 2 – e, (5).



a. b. c. d. e.

Fig.2. Calculation models of the main elements of the measuring unit of an atomic force microscope: a – of a cut cone element (probe); b – of a small thickness plate (sample); c – of a small thickness plate (cantilever); d – of the end surface of the cylinder (piezoscanner); e – of a spherical element segment (probe tip).

The coordination of the results of solving this system was carried out according to the heat balance scheme, in which the total thermal contribution was evenly divided between all the elements that took part in the heat exchange (the thermal and physical properties of the materials (heat capacity, thermal conductivity) of which these elements were made were not taken into account).

To confirm the adequacy of the considered models of heat transfer, an equivalent thermal scheme of the AFM was compiled and researched [7, 8].

The method of equivalent thermal circuits is most prevalent because of the simplicity and sufficient accuracy of the calculation. The disadvantage of the method is that it does not provide a complete picture of the temperature field, but only some average values of temperature for individual elements of the instrument or machine.

This method is based on the use of thermal resistances, which are connected to a heating network that simulates the actual paths of heat flow in the device, and suggests an analogy of heat flow with electric current, based on the same form of the basic law of thermal conductivity (Fourier's law): $\Delta P = \Delta\theta / R_T$ and electric current (Ohm's law): $I = \Delta U / R_E$, where $\Delta\theta$ – temperature drop; R_T – thermal resistance of this gap in the heat flow path; ΔU – potential difference at the ends of the conductor; R_E – electrical resistance.

The system of equations for this scheme in the mode that is installed is given below. In this system of equations m – number of nodes equivalent thermal scheme; θ_B – temperature outside the element in question; $\Lambda_{ki}=1/R_{ki}$ – thermal conductivity of the corresponding section of the scheme; P_i – heat losses in the i-th node.

$$\begin{cases} P_1 = \left(\sum_{k=1}^{m} \Lambda_{k1}\right)\cdot(\theta_1 - \theta_{\hat{a}}) - \sum_{k=1}^{m}\left(\Lambda_{k1}\cdot(\theta_k - \theta_{\hat{a}})\right) \\ P_2 = \left(\sum_{k=1}^{m} \Lambda_{k2}\right)\cdot(\theta_2 - \theta_{\hat{a}}) - \sum_{k=1}^{m}\left(\Lambda_{k2}\cdot(\theta_k - \theta_{\hat{a}})\right) \\ \ldots\ldots\ldots\ldots\ldots\ldots\ldots\ldots\ldots\ldots\ldots\ldots \\ P_m = \left(\sum_{k=1}^{m} \Lambda_{km}\right)\cdot(\theta_m - \theta_{\hat{a}}) - \sum_{k=1}^{m}\left(\Lambda_{km}\cdot(\theta_k - \theta_{\hat{a}})\right) \end{cases}$$

To calculate the non-stationary mode, the same thermal scheme is used, but each node is connected through a capacitor. In this case, the electrical capacitance is equivalent to the heat capacity of the body. The system of equations for the non-stationary mode is as follows:

$$\begin{cases} C_1\cdot\frac{d\theta_1}{dt} = \left(-\sum_{k=1}^{m} \Lambda_{k1}\right)\cdot(\theta_1 - \theta_{\hat{a}}) + \sum_{k=1}^{m}\left(\Lambda_{k1}\cdot(\theta_k - \theta_{\hat{a}})\right) + P_1 \\ C_2\cdot\frac{d\theta_2}{dt} = \left(-\sum_{k=1}^{m} \Lambda_{k2}\right)\cdot(\theta_2 - \theta_{\hat{a}}) + \sum_{k=1}^{m}\left(\Lambda_{k2}\cdot(\theta_k - \theta_{\hat{a}})\right) + P_2 \\ \ldots\ldots\ldots\ldots\ldots\ldots\ldots\ldots\ldots\ldots\ldots\ldots \\ C_m\cdot\frac{d\theta_m}{dt} = \left(-\sum_{k=1}^{m} \Lambda_{km}\right)\cdot(\theta_m - \theta_{\hat{a}}) + \sum_{k=1}^{m}\left(\Lambda_{km}\cdot(\theta_k - \theta_{\hat{a}})\right) + P_m \end{cases}$$

where Ci – heat capacity of the corresponding scheme node.

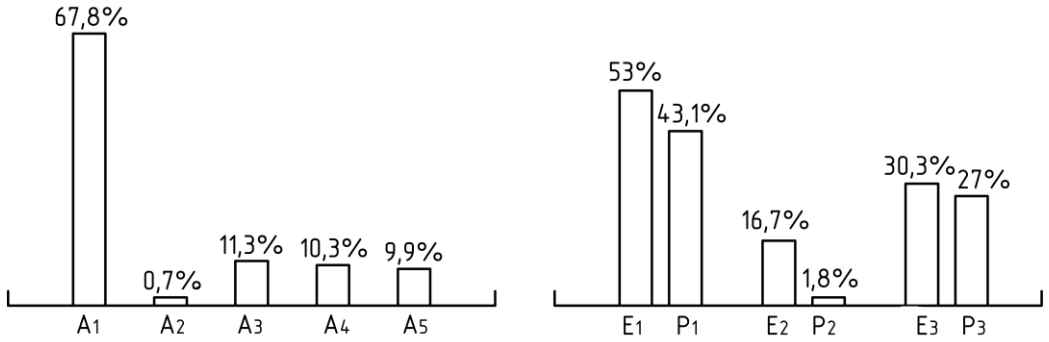
The systems of differential equations given above, in fact, are thermal models of heating individual elements of the measuring unit of an atomic force microscope. The main factors determining the accuracy of the calculation using this equation are:

- accuracy of setting sources of heat, i.e. losses;
- the accuracy of determining thermal conductivities, which in turn depend on:

a) thermal conductivity coefficients λ, which are prone to significant variation for technological reasons, under the influence of the appearance of air gaps, etc.;

b) heat transfer coefficients α, since empirical formulas and graphs available for their definition cannot take into account all factors and conditions affecting.

As a result of the calculations carried out, using both mathematical models using the inverse Fourier transform method and the equivalent thermal circuit method, the energy heat exchange was estimated and the main heat losses in the contact zone of the probe of the atomic force microscope with the surface were determined [9, 10] (Fig.3).



a. b.

Fig.3. Heat emission diagrams (a) and energy heat input (b) in the zone of contact of the probe with the test surface. Heat dissipation: A_1 – on the mechanical friction of the probe on the test surface; A_2 – on the action of electromagnetic fields and electric charge; A_3 – on the bending of cantilever; A_4 – on the torsion of cantilever; A_5 – on the torsion of piezoscanner. Thermal energy contribution: E_1 – the energy that drives the piezoscanner; P_1 – useful work piezoscanner; E_2 – energy that is fed to the cantilever with the probe; P_2 – useful work of the sensing element; E_3 – laser positioner radiation energy; P_3 – laser energy that hits a photo detector.

As can be seen from the diagrams above, more heat generation in the contact zone arises due to friction of the probe on the test surface and is 67,8% (Fig. 3, a), at the same time, the maximum thermal contribution comes from the energy supplied to the piezoscanner (Fig. 3, b).

Thus, the use of the method of equivalent thermal circuits for evaluating mathematical models of the energy interaction of AFM probes with material surfaces, as well as further research on the distribution of thermal fields in the AFM control unit, differs from other numerous and analytical methods by sufficient accuracy and speed of calculations. Today, due to the lack of experimental methods for confirming the adequacy of mathematical models of thermal conductivity in the zone of interaction between the probe and the surface under study, this method is an alternative method for confirming the results obtained during the simulation. At the same time, the discrepancy between the results of mathematical modeling and the results obtained with an equivalent thermal circuit does not exceed 5 – 8%.

3. Conclusion

The modeling of the energy interaction of AFM probes with the surfaces of materials at the preparatory, final stages and the scanning stage of the investigated surface was carried out taking into account the energy components of the processes occurring in the AFM control unit by minimizing factors (heat dissipation due to friction of the probe on the surface Q_1) negatively affecting both the control results and the state of the probe and surface established modes of stable operation of the AFM.

Mathematical modeling of the heating process of individual elements of the AFM measuring unit, confirmed by solving a system of differential equations with an equivalent thermal circuit,

which made it possible to conclude that the main heat losses and energy impact in the zone of contact of the probe with the surface under study. Thus, it was found that the most heat release in the contact zone (about 68%) arises due to probe friction on the surface, while the heat contribution (53%) comes from the energy supplied to the piezoscanner.

4. Literature

1. Mikroskopiya v nanotexnologiyax (Microscopy in nanotechnology) [Tekst]: monohrafiia / V.Antonyuk, G.Tymchyk, E.Vertsanova ta in. // K.: NTUU «KPI», 2014. – 260 s.
2. M. Bondarenko, Yu. Bondarenko, and V.Antonyuk, "Perspektyvy vykorystannya metodu atomno-sylovoyi mikroskopiyi dlya doslidzhennya stanu ta fizyko-mexanichnyx xarakterystyk poverxon vyrobiv precyzijnogo mashynobuduvannya" (Prospects for the use of atomic force microscopy for the study of the condition and physical and mechanical characteristics of surfaces of precision engineering products). Visnyk nacionalnogo universytetu «Lvivska politexnika». Seriya: Optymizaciya vyrobnychyx procesiv i texnichnyj kontrol u mashynobuduvanni ta pryladobuduvanni: nauk. zbir. – Lviv: Vydavnycztvo Lvivskoyi politexniky, 2015. – Iss.822. – pp. 72-77.
3. D. Sarid, Scanning force microscopy with applications to electric, magnetic and atomic forces. New York, NY, USA: Oxford Univ. Press, 1991.
4. E.Dolgova, V.Konstantinov, D.Kurushin, and R.Faizerahmanov, "Kompyuternoe modelyrovanye manypulyrovanyya nanoobektamy pry pomoshhy atomno-sylovogo mykroskopa" (Computer simulation of manipulation of nano-objects with the help of atomic force microscope). Upravlenye, vychyslytelnaya texnyka y ynformatyka. – Vol.15, Iss.2(42). – pp. 45-51.
5. A. Suslov, M. Bondarenko, and O. Andrienko, "Perspectives of development of multiinstrumental atomic-force microscopy under nanometric researches of components of microsystem equipment", in VII International Scientiific Conference "Sensors, devices and systems – 2018", Cherkasy, 2018, pp. 80-82.
6. O.Garyshyn, and S.Lebedev, "Teoretycheskoe modelyrovanye raboty atomno-sylovogo mykroskopa pry yssledovany y poverxnostej so slozhnoj nanostrukturoj" (Theoretical modeling of the work of an atomic force microscope in the study of surfaces with complex nanostructures). Mexanyka, 2013. – Iss. 1. – pp. 68-80.
7. S.Moya, "Thermal Modeling Techniques of Heat Assisted Single Point Incremental Forming in ANSYS Workbench". SC, USA: Clemson University, 2017.
8. Osnovy teploperenesennya v elementax optychnogo pryladobuduvannya (Fundamentals of heat transfer in the elements of optical instrumentation) [Tekst]: monohrafiia / V.Vaschenko ta in. // K.: NTUU «KPI», 2012. – 340 s.
9. M.Bondarenko, Yu.Bondarenko, S.Shelestovskaya, and V.Andriienko, "Energy heat exchange in the area of contact of the probe of the atomic force microscope with the investigated surface", in XII International Scientiific Conference "Methodological aspects of scanning probe microscopy", Minsk, 2016, pp. 235-241.
10. M.Bondarenko, J.Bondarenko, and S.Shelestovskaya, "Research of Influence of the State of Surface of Probes for AFM on Exactness and Quality of the Topograms", in XXXI International Scientiific Conference Electronics and Nanotechnology, Kyiv, 2011, pp. 60.

EXAMPLES OF SOFTWARE CONFIGURATION MANAGEMENT

M.Sc. Ivanova Milka
Faculty of Mechanical Engineering – Technical University of Sofia, Bulgaria
milkachr@tu-sofia.bg

Abstract: *When you build software the changes happens. Because it happens you need to manage it effectively; this is a set of activities designed to manage shanges by identifying the work prodicts that are lakely to change, establishing relationships among them, defining the mechanism for managing work products, controling the changes imposed ang repochanges made. In the report is made the distinction between software support and software configuration managemet ang give the examples of using.*

Keywords*: Software engineering, Software Configuration Management (SCM), Elements of SCM System, SCElements,SCM Layers SCM features*

Introduction

Software configuration management (SCM), also called change management, is a set of activities designed to manage change by identifying the work products that are likely to change, establishing relationships among them, defining mechanisms for managing different versions of these work products, controlling the changes imposed, and auditing and reporting on the changes made.

SCM activities are developed to: identify change, control change, ensure that change is being properly implemented, and report changes to others who may have an interest.

Software configuration management is a set of tracking and control activities that are initiated when a software engineering project begins and terminates only when he software is taken out of operation (in opposite to Support that is a set of software engineering activities that occur after software has been delivered to the customer and put into operation).

Software Configuration Management

A primary goal of software engineering is to improve the ease with which changes can be accommodated and reduce the amount of effort expended when changes must be made.

The output of the software process is information that may be divided into three broad categories: computer programs (both source level and executable forms), work products that describe the computer programs (targeted at various stakeholders), and data or content (contained within the program or external to it). The items that comprise all information produced as part of the software process are collectively called a *software configuration.*

As software engineering work progresses, a hierarchy of *software configuration items* (SCIs) - a named element of information that can be as small as a single UML diagram or as large as the complete design document - is created. If each SCI simply led to other SCIs, little confusion would result. Unfortunately, another variable enters the process - *change.* Change may occur at any time, for any reason. In fact [1,2] states: "No matter where you are in the system life cycle, the system will change, and the desire to change it will persist throughout the full life cycle."

There are 4 sources of changes:

- New business or market conditions dictate changes in product requirements or business rules.
- New stakeholder needs demand modification of data produced by information systems, functionality delivered by products, or services delivered by a computer-based system.
- Reorganization or business growth/downsizing causes changes in project priorities or software engineering team structure.
- Budgetary or scheduling constraints cause a redefinition of the system or product.

Elements of Software Configuration Management System

Software configuration management is a set of activities that have been developed to manage change throughout the life cycle of computer software. SCM can be viewed as a software quality assurance activity that is applied throughout the software process. In the sections that follow.

A typical CM operational scenario involves a project manager who is in charge of a software group, a configuration manager who is in charge of the CM procedures and policies, the software engineers who are responsible for developing and maintaining the software product, and the customer who uses the product.

The goals of the configuration manager are to ensure that procedures and policies for creating, changing, and testing of code are followed, as well as to make information about the project accessible. To implement techniques for maintaining control over code changes, this manager introduces mechanisms for making official requests for changes, for evaluating them and for authorizing changes. The manager creates and disseminates task lists for the engineers and basically creates the project context. Also, the manager collects statistics about components in the software system, such as information determining which components in the system are problematic.

The White paper on software configuration management [3] identifies four important elements that should exist when a configuration management system is developed:

- *Component elements* - a set of tools coupled within a file management system (e.g., a database) that enables access to and management of each software configuration item.
- *Process elements* - a collection of actions and tasks that define an effective approach to change management (and related activities) for all constituencies involved in the management, engineering, and use of computer software.
- *Construction elements* - a set of tools that automate the construction of software by ensuring that the proper set of validated components (i.e. the correct version) have been assembled.
- *Human elements* - a set of tools and process features (encompassing other CM elements) used by the software team to implement effective SCM.

In the context of software engineering, a baseline is a milestone in the development of software. A baseline is marked by the delivery of one or more software configuration items that have been approved as a consequence of a technical review. For example, the elements of a design model have been documented and reviewed. Errors are found

and corrected. Once all parts of the model have been reviewed, corrected, and then approved, the design model becomes a baseline. Further changes to the program architecture (documented in the design model) can be made only after each has been evaluated and approved. Although baselines can be defined at any level of detail, the most common software baselines

The software configuration item are defined as information that is created as part of the software engineering process. In the extreme, a SCI could be considered to be a single section of a large specification or one test case in a large suite of tests. More realistically, an SCI is all or part of a work product (e.g., a document, an entire suite of test cases, or a named program component).

In addition to the SCIs that are derived from software work products, many software engineering organizations also place software tools under configuration control. That is, specific versions of editors, compilers, browsers, and other automated tools are "frozen" as part of the software configuration. Because these tools were used to produce documenttation, source code, and data, they must be available when changes to the software configuration are to be made. Although problems are rare, it is possible that a new version of a tool (e.g. a compiler) might produce different results than the original version. For this reason, tools, like the software that they help to produce, can be baselined as part of a comprehensive configuration management process.

In reality, SCIs are organized to form configuration objects that may be cataloged in the project database with a single name. A *configuration object* has a name, attributes, and is "connected" to other objects by relationships. Referring to Figure 1, the configuration objects, **DesignSpecification, DataModel, ComponentN, SourceCode,** and **TestSpecification** are each defined separately. However, each of the objects is related to the others as shown by the arrows. A curved arrow indicates a compositional relation. That is, **DataModel** and **ComponentN** are part of the object **DesignSpecification.** A double-headed straight arrow indicates an interrelationship. If a change were made to the **SourceCode** object, the interrelationships enable you to determine what other objects (and SCIs) might be affected

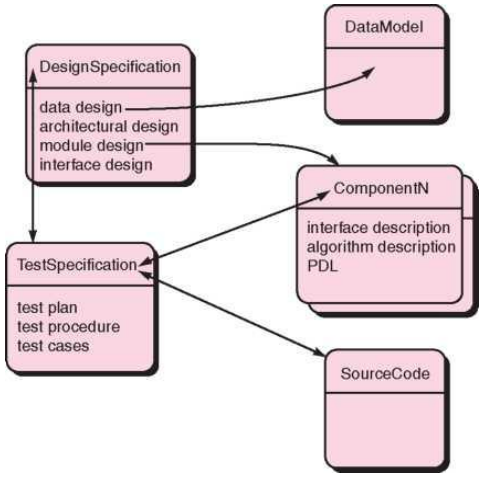


Fig. 1

Today, SCIs are maintained in a project database or repository. *Webster's Dictionary* defines the word *repository* as "any thing or person thought of as a center of accumulation or storage." During the early history of software engineering, the repository was indeed a person - the programmer who had to remember the location of all information relevant to a software project, who had to recall information that was never written down and reconstruct information that had been lost. Sadly, using a person as "the center for accumulation and storage" (although it conforms to Webster's definetion) does not work very well. Today, the repository is a "thing" - a database that acts as the center for both accumulation and storage of software engineering information. The role of the person (the software engineer) is to interact with the repository using tools that are integrated with it.

Software Configuration Management Features

To support SCM, the repository must have a tool set that provides support for the following features:

Versioning As a project progresses, many versions of individual work products will be created. The repository must be able to save all of these versions to enable effective management of product releases and to permit developers to go back to previous versions during testing and debugging.

The repository must be able to control a wide variety of object types, including text, graphics, bit maps, complex documents, and unique objects like screen and report definetions, object files, test data, and results. A mature repository tracks versions of objects with arbitrary levels of granularity; for example, a single data definition or a cluster of modules can be tracked.

Dependency tracking and change management The repository manages a wide variety of relationships among the data elements stored in it. These include relationships between enterprise entities and processes, among the parts of an application design, between design components and the enterprise information architecture, between design elements and deliverables, and so on. Some of these relationships are merely associations, and some are dependencies or mandatory relationships.

The ability to keep track of all of these relationships is crucial to the integrity of the information stored in the repository and to the generation of deliverables based on it, and it is one of the most important contributions of the repository concept to the improvement of the software process. For example, if a UML class diagram is modified, the repository can detect whether related classes, interface descriptions, and code components also require modification and can bring affected SCIs to the developer's attention.

Requirements tracing This special function depends on link management and provides the ability to track all the design and construction components and deliverables that result from a specific requirements specification (forward tracing). In addition, it provides the ability to identify which requirement generated any given work product (backward tracing).

Configuration management. A configuration management facility keeps track of a series of configurations representing specific project milestones or production releases.

Audit trails. An audit trail establishes additional information about when, why, and by whom changes are made. Information about the source of changes can be entered as attributes of specific objects in the repository. A repository trigger mechanism is helpful for prompting the developer or the tool that is being used to initiate entry of audit information (such as the reason for a change) whenever a design element is modified.

The software configuration management process defines a series of tasks that have four primary objectives: to identify

all items that collectively define the software configuration, to manage changes to one or more of these items, to facilitate the construction of different versions of an application, and to ensure that software quality is maintained as the configuration evolves over time.

A process that achieves these objectives need not be bureaucratic or ponderous, but it must be characterized in a manner that enables a software team to develop answers to a set of complex questions:

- How does a software team identify the discrete elements of a software configuration?
- How does an organization manage the many existing versions of a program (and its documentation) in a manner that will enable change to be accommodated efficiently?
- How does an organization control changes before and after software is released to a customer?
- Who has responsibility for approving and ranking requested changes?
- How can we ensure that changes have been made properly?
- What mechanism is used to apprise others of changes that are made?

These questions lead to the definition of five SCM tasks—identification, version control, change control, configuration auditing, and reporting—illustrated in Figure 2.

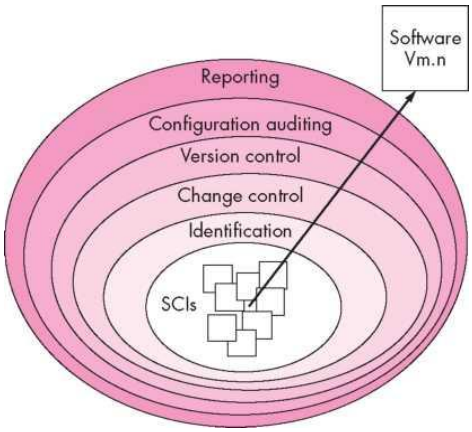


Figure 2

Referring to the figure, SCM tasks can viewed as concentric layers. SCIs flow outward through these layers throughout their useful life, ultimately becoming part of the software configuration of one or more versions of an application or system. As an SCI moves through a layer, the actions implyed by each SCM task may or may not be applicable. For example, when a new SCI is created, it must be identified. However, if no changes are requested for the SCI, the change control layer does not apply. The SCI is assigned to a specific version of the software (version control mechanisms come into play). A record of the SCI (its name, creation date, version designation, etc.) is maintained for configuration auditing purposes and reported to those with a need to know. In the sections that follow, we examine each of these SCM process layers in more detail.

Software Configuration Management Layers

To control and manage SCI is need to used object-orientated approach. Two types of objects can be identified [4]: basic objects and aggregate objects. A *basic object* is a unit of information that you create during analysis, design, code, or test. For example, a basic object might be a section of a requirements specification, part of a design model, source code for a component, or a suite of test cases that are used to exercise the code. An *aggregate object* is a collection of basic objects and other aggregate objects. For example, a **DesignSpecification** is an aggregate object. Conceptually, it can be viewed as a named (identified) list of pointers that specify aggregate objects such as **ArchitecturalModel** and **DataModel,** and *basic objects* such as **Compo- nentN** and **UMLClassDiagramN** (Fig. 1)**.**

Configuration object identification can also consider the relationships that exist between named objects.
For example:

Class diagram <part-of> requirements model;

Requirements model <part-of> requirements

in SCIs hierarchy:

DataModel <interrelated> DataFlowModel

DataModel <interrelated> TestCaseClassM

The identification scheme for software objects must recognize that objects evolve throughout the software process. Before an object is baselined, it may change many times, and even after a baseline has been established, changes may be quite frequent.

Version control combines procedures and tools to manage different versions of configuration objects that are created during the software process. A version control system implements or is directly integrated with four major capabilities: a project database (repository) that stores all relevant configuration objects, a *version management* capability that stores all versions of a configuration object (or enables any version to be constructed using differences from past versions), a *make facility* that enables you to collect all relevant configuration objects and construct a specific version of the software. In addition, version control and change control systems often implement an *issues tracking* (also called *bug tracking)* capability that enables the team to record and track the status of all outstanding issues associated with each configuration object.

A number of different automated approaches to version control have been proposed over the last few decades. The primary difference in approaches is the sophistication of the attributes that are used to construct specific versions and variants of a system and mechanics of construction's process.

For a large software project, uncontrolled change rapidly leads to chaos. For such projects, change control combines human procedures and automated tools to provide a mechanism for the control of change. The change control process is illustrated schematically in Figure 3. A *change request* is submitted and evaluated to assess technical merit, potential side effects, overall impact on other configuration objects and system functions, and the projected cost of the change. The results of the evaluation are presented as a *change report*, which is used by a *change control authority* (CCA) - a person or group that makes a final decision on the status and priority of the change. An *engineering change order* (ECO) is generated for each approved change. The ECO describes the change to be made, the constraints that must be respected, and the criteria for review and audit.

Prior to an SCI becoming a baseline, only *informal change control* need be applied. The developer of the configuration object (SCI) in question may make whatever changes are justified by project and technical requirements (as long as changes do not affect broader system requirements that lie

outside the developer's scope of work). Once the object has undergone technical review and has been approved, a baseline can be created. Once an SCI becomes a baseline, *project level change control* is implemented. Now, to make a change, the developer must gain approval from the project manager (if the change is "local") or from the CCA if the change affects other SCIs. In some cases, formal generation of change requests, change reports, and ECOs is dispensed with. However, assessment of each change is conducted and all changes are tracked and reviewed.

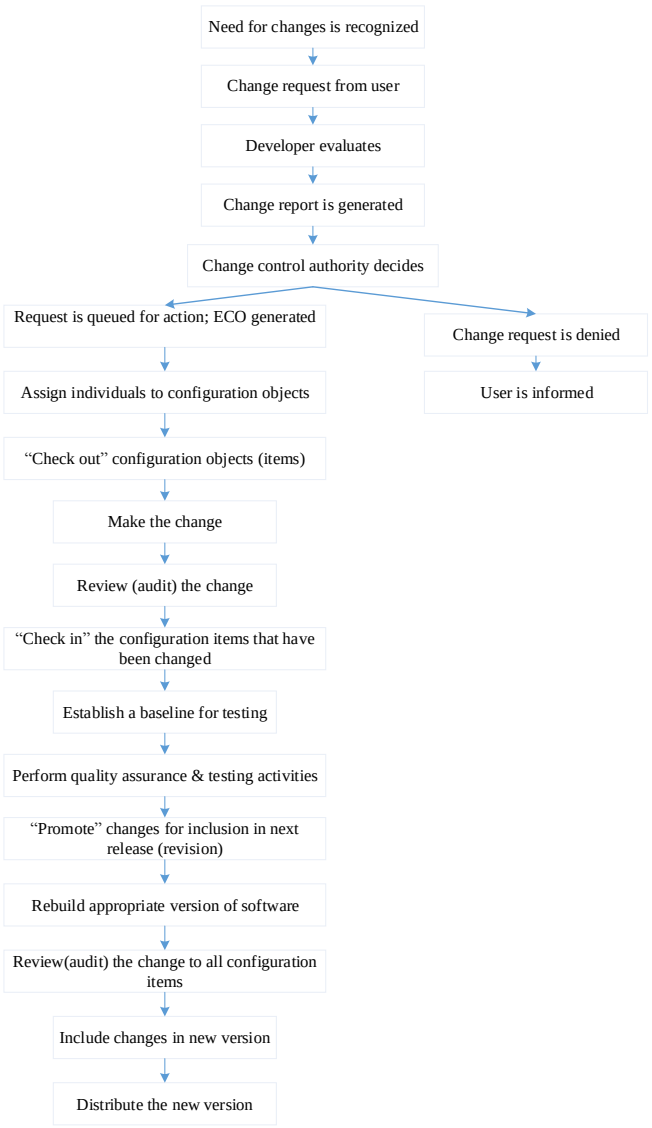


Figure 3

When the software product is released to customers, *formal change control* is instituted. The formal change control procedure has been outlined in Figure 3.

The change control authority plays an active role in the second and third layers of control. Depending on the size and character of a software project, the CCA may be composed of one person - the project manager - or a number of people (e.g., representatives from software, hardware, database engineering, support, marketing). The role of the CCA is to take a global view, that is, to assess the impact of change beyond the SCI in question. How will the change affect hardware? How will the change affect performance? How will the change modify customers' perception of the product? How will the change affect product quality and reliability? These and many other questions are addressed by the CCA.

A *software configuration audit* complements the technical review by assessing a configuration object for characteristics that are generally not considered during review. The audit asks and answers the following questions:

1. Has the change specified in the ECO been made? Have any additional modifications been incorporated?
2. Has a technical review been conducted to assess technical correctness?
3. Has the software process been followed and have software engineering standards been properly applied?
4. Has the change been "highlighted" in the SCI? Have the change date and change author been specified? Do the attributes of the configuration object reflect the change
5. Have SCM procedures for noting the change, recording it, and reporting it been followed
6. Have all related SCIs been properly updated?

Configuration status reporting (sometimes called *status accounting)* is an SCM task that answers the following questions: What happened? Who did it? When did it happen? What else will be affected?

The flow of information for configuration status reporting (CSR) is illustrated in Figure 3. Each time an SCI is assigned new or updated identification, a CSR entry is made. Each time a change is approved by the CCA (i.e., an ECO is issued), a CSR entry is made. Each time a configuration audit is conducted, the results are reported as part of the CSR task. Output from CSR may be placed in an online database or website, so that software developers or support staff can access change information by keyword category. In addition, a CSR report is generated on a regular basis and is intended to keep management and practitioners appraised of important changes.

Summary

SCM is an umbrella activity that is applied throughout the software process: identifies, controls, audits, and reports modifications that invariably occur while software is being developed and after it has been released to a customer. All work products created as part of software engineering become part of a software configuration. The configuration is organized in a manner that enables orderly control of change. The SCIs are produced as a result of some software engineering activity. In addition to documents, programs, and data, the development environment that is used to create software can also be placed under configuration control. All SCIs are stored within a repository that implements a set of mechanisms and data structures to ensure data integrity, provide integration support for other software tools, support information sharing among all members of the software team, and implement functions in support of version and change control. The evolution of a program can be tracked by examining the revision history of all configuration objects.

Bibliography:

1. Pressman, R. Software Engineering , A Practitioner's Approach, McGrawHill Higher Education, Seventh Edition, 2010

2. Bersoff, E. H., V. D. Henderson, and S. G. Siegel, Software Configuration Management, Prentice Hall, 2010

3. Boehm, B., "Making a Difference in the Software Century," *IEEE Computer*, vol. 41, no. 3, March 2008,

MICROSTRUCTURE AND MECHANICAL PROPERTIES OF A HYPEREUTECTIC ALLOY AlSi18, MODIFIED BY A NANODIAMOND AND PHOSPHORUS

Assistant Dochev B.[1] eng., Head Assistant Velikov A.[2] PhD, Head Assistant Panov Iv. [1] PhD, Head Assistant Diakova V. [2] PhD, Head Assistant Kuzmanov P. [2] PhD, Associate Professor Manolov V. [2] PhD

[1] Sofia Technical University, Plovdiv Branch, Bulgaria
[2]Bulgarian Academy of Sciences, Institute of metal science, equipment and technologies with hydro- and aerodynamic center "Acad.A. Balevski" – Sofia, Bulgaria

pawel_71@abv.bg

Abstract: *A study of a hypereutectic aluminum-silicon alloy AlSi18, modified by a conventional modifier - phosphorus (P) and a nanosized powder of a nanodiamond (ND) has been carried out. Refinement by 40.8% of the primary Si crystals and by 51% of the Si crystals in the composition of the eutectic has been obtained for the phosphorus-modified alloy in result of the modification. The refinement of the above values for the alloy modified by ND is 41.5% and 94% respectively. The phosphorus-modified alloy AlSi18 has an increased tensile strength (R_m) by 18.5%, relative elongation (A_5) by 14.3% and hardness by 1.5%. The alloy, modiified by ND has an increased by 20.4% tensile strength (R_m), increased relative elongation (A_5) by 7.15% and hardness decreases by 6.2%.*

Key words: *NANODIAMOND, MODIFICATION, CRYSTALLIZATION*

1. Introduction

Experiments with new types of nanomodifiers (NM) have been carried out in the recent years. Nanomodifiers are ultrafine nanopowders with particles sizing 4-100 nm, with a high melting phoint (~ 2273 - 3273 K depending on the composition), obtained either by self-propagating high-temperature synthesis (SPHTS) [1] or by plasma-chemical synthesis (PCS) and used for producing nitrides, carbides, oxides, oxi-carbides, etc. [1-3]. Nanosized diamonds or nanodiamonds (NDs) are also used. The production of nanosized diamond particles is carried out by blasting. When blasting explosives with a negative oxygen balance, the released carbon is transformed into a diamond at the corresponding pressure values P and temperature T [4]. After proper processing, the nanoscale diamond can be used for aluminum alloys modifying.

Most of the existing studies have been performed on hypoeutectic aluminum-silicon alloys, eutectic aluminum-silicon alloys and other types of alloys [5-9]. The influence of ND on the structure and mechanical properties of A356 alloy was investigated in [10]. In the present work, a study was conducted on the modifying effect of a standard modifier (P), on the one hand, and a nanomodifier - nanodiamond (ND), on the other hand, on both the structure and the mechanical properties of the hypereutectic aluminum-silicon AlSi18 alloy.

2. Experimental Studies

Table 1. Chemical composition of AlSi18 alloy, wt.%

Si	Fe	Cu	Mn	Mg	Cr	Ni	Zn	Pb	Al
17.55	0.120	0.025	0.047	0.001	0.001	0.005	0.102	0.01	Ост.

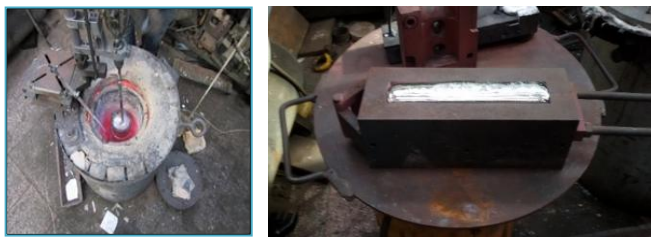
The chemical composition of the alloy is shown in Table 1.

The alloy is modified by a standard modifier - phosphorus, which is introduced in the form of a ligature CuP10 - copper phosphorus alloy. The nanosized nanodiamond powder is manufactured by Nanostructured & Amorphous Materials, Inc. and has an average particle size of 3-5nm. To improve the wetting of the ND particles in the melt, cladding by Ni was performed, using a currentless method [3].

For the purpose of the study, experiments were carried out with an unmodified, modified by a standard modifier and modified by a nanomodifier ND AlSi18 alloy. The melting of the alloy is carried out in a graphite electric resistance laboratory furnace by using preliminary cleaned and dry stock materials. The melting process takes place under a layer of roof-refining flux in an amount of 0.5 wt% from the amount of the stock material. The resulting melt is stirred vigorously for removing non-metallic inclusions and then the slag is removed. This is followed by degassing the alloy at 760 °C by purging with argon for 3 minutes and removing the metal mirror from the slag. Unmodified samples are casted after that. Similarly to the above the alloy is melted and prepared for the introduction of a copper-phosphorus modifier or a nanomodifier ND.

The introduction of a standard modifier (P) into the melt in the amount of 0.4 wt% of the alloy quantity is carried out at a temperature of 770°C. After introducing the modifier into the melt, it is stirred vigorously until the modifier is fully absorbed and degassed at 760°C - 770°C by purging with argon for 3 min.

In the case of alloy nanomodification after refining and degassing the melt, it is modified by a ND modifier, with a concentration in the melt equal to 0.1 wt% at a temperature of 760°C. For this purpose, the calculated amount of ND corresponding to this concentration is packed in an aluminum container, which is attached to the impeller and the impeller is introduced into the melt. Mechanical stirring is then performed in order to melt the container and homogenize the melt for 3-5 min at revolutions of about 120 - 130 min^{-1}.



a) *b)*

Figure 1 a) Melting furnace with a homogenization unit, (1b) a mold with a "Wedge"-type casting,

Figure 1a) shows the moment of homogenization by using an impeller. Prior to casting, the mold – a steel mold with a vertical dividing surface (Fig. 1b) - is heated up to 200 ° C and coated with a fire-resistant coating. "Wedge"-type castings are produced by removing the crucible from the furnace by means of a special device

and pouring into the mold. Figure 1b) shows a mold with an AlSi18 casting. All experiments were performed at near temperatures of the melt. To meet these conditions, the temperature of the mold is measured by a contact thermocouple.

The "wedge"- type casting weighs ~ 0.850 kg. The trapezoidal part of the casting is designed as a feeder to provide good nutrition for of the working part during crystallization. After removing the feeder, the cylindrical sample from the casting with sizes of Ø20 x 230 mm is used for taking samples for examination. cylindrical sample marked with (1) respectively, while the samples

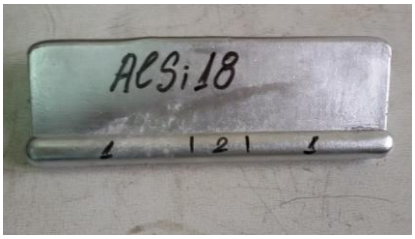


Figure 2. A "Wedge"-type casting with marked sampling points

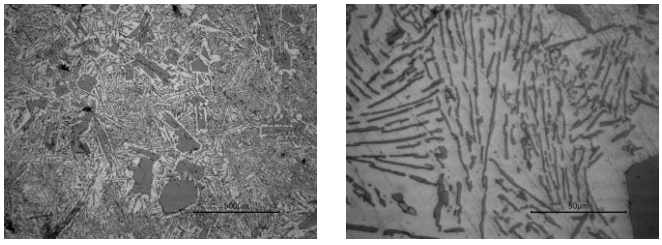
for structural analysis are produced from the part (2) (Fig. 2). The samples for macro and microstructure analysis are wet grinded by using sandpaper numbers 240, 320, 400 and 600, 800 and 1000. They are then mechanically polished with a diamond paste and a lubricant. The macrostructure of the alloys is etched by a Poulmont reagent (60 p. HCl (conc), 30 p. HNO3 (conc), 5 p. HF, 5 p. H2O). The microstructure of the samples is etched expressed by a Keller reagent (1 p. HF, 1.5 p. HCl, 2.5 p. HNO3, 95 p. H2O). The structures are qualitatively characterized with the help of Zeiss metallographic JENAVERT microscopes. Top View image processing software is used for the quantitative metallographic analysis.

The average size of the primary silicon crystals as well as the size of the silicon particles in the eutectic were determined. The influence of both the standard P modifier and the ND nanomodifier on the structure of the investigated hypereutectic aluminum - silicon alloy AlSi18 was established.

The mechanical tests of the samples, produced in accordance with the standard, were carried out on a Zwick/Roell Z 250 tensile test machine. The average values of the mechanical properties tensile strength Rm and relative elongation A5 were determined for the cases of modification by ND and by a combination of a standard modifier P and ND.

3. Results and discussions

3.1. Microstructural studies

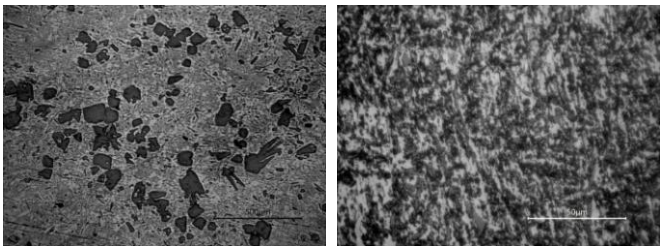


a) *b)*

Figure 3. Microstructure of unmodified AlSi18 alloy: a) primary Si crystals, b) Si crystals in the composition of the eutectic

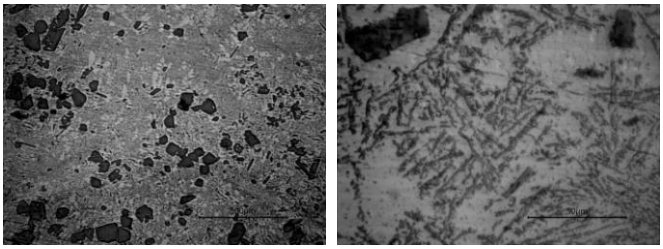
The microstructure of the unmodified AlSi18 alloy samples consists of eutectic and separated primary silicon crystals (Fig. 3a). The shape of the primary silicon crystals is different: straight-walled polygons, well-shaped plates, which in the plane of microscopic observation resemble needles or irregularly shaped plate-type crystals. The arbitrary average diameter of the primary silicon crystals in the unmodified AlSi18 alloy is within the range 87.2-97.6 μm.

Several types of zones are observed in the eutectic of an unmodified AlSi18 alloy (Fig. 3b). The first type is with well-shaped elongated needle-type plates, measuring up to 250-260 μm in length. In the second type small silicon crystals of several microns in size are observed, which form groups or are adjacent to each other and, at small microscopic magnifications, resemble a broken needle. In the third zone type, fine silicon crystals resembling "fish bone" are observed.



a) *b)*

Figure 4. Microstructure of AlSi18 alloy modified by P: a) primary Si crystals, b) Si crystals in the composition of the eutectic



a) *b)*

Figure 5. Microstructure of AlSi18 alloy modified by ND: a) primary Si crystals, b) Si crystals in the composition of the eutectic

The microstructure of the alloy AlSi18 samples, modified by phosphorus and modified by ND, consists of eutectic and separated primary silicon crystals. The shape of the primary silicon crystals in the two alloys is different from the one of the unmodified alloy. Primary silicon crystals in the form of polygons predominate in both the phosphorus modified alloy (Fig. 4a) as well as in the samples, modified by ND (Fig. 5a), and the amount of primary irregularly shaped crystals is negligible. The size of the primary silicon crystals in the two samples is similar: for the AlSi18 alloy modified by phosphorus - 55.7 μm and for the AlSi18 alloy modified by a nanomodifier ND - 54 μm.

The eutectic of the AlSi18 alloy modified by a phosphorus is made up of well-shaped needles around which small silicon crystals adhere (Fig. 4b). The average maximum needle length is in the range of 115-135 μm. In the AlSi18 alloy modified by ND nanomodifier, the amount and the average length of the eutectic needles decreases - their average maximum length is about 15–16 μm, but the fraction of small equi-axed silicon compartments increases (Fig. 5b).

Table 2. Microstructure parameters of the initial and modified AlSi18 alloy

Alloy	Modifier	Arbitrary average diameter of the primary Si crystals D [μm]	Refinement, %	Average maximum needle length of the Si crystals in the composition of the eutectic [μm]	Refinement, %
AlSi18		92,4		250-260	
AlSi18	P	55.7	40.8	115-135	51
AlSi18	ND	54	41,5	15-16	94

The results obtained from the quantitative metallographic analysis are shown in Table 2.

The table shows that, as a result of the modification of AlSi18 alloy by standard modifier (phosphorus) the arbitrary average diameter of the primary Si crystals decreases by 40.8% and the size of the Si crystals in the composition of the eutectic - by 93.2%.

The modification of the alloy by ND nanomodifier results in a reduction of 41.5% in the arbitrary average diameter of the primary Si crystals and of 94% in the size of the Si crystals in the composition of the eutectic.

3.2. Mechanical tests

Table 3. Results from mechanical tests of AlSi18 alloy

Alloy	Modifier	Rm/Mpa	Re/Mpa	A_5 /%/	HB2,5/62,5/30
AlSi18		108		1.4	65
AlSi18	P	128		1.6	66
Change, %		+18.5		+14.3	+1.5
AlSi18	ND	130	85	1.5	61
Change, %		+20.3		+7.1	-6.2

The results from the mechanical tests carried out on an unmodified, modified by standard modifier P and modified by ND nanomodifier alloy AlSi18 are shown in Table 3.

It can be seen from the table that the phosphorus-nanomodified AlSi18 alloy has an increased tensile strength (Rm) by 18.5% and increased elongation (A5) by 14.3% compared to the unmodified alloy. Hardness increases by 1.5%.

The alloy modified by ND-modifier has an increased tensile strength (Rm) by 20.4% and increased elongation (A5) by 7.1% compared to the unmodified alloy. Hardness decreases by 6.2%.

4. Conclusions

As a result of the conducted studies of the modification of the hypereutectic aluminum-silicon alloy AlSi18, modified both by a standard modifier (P) and by a nanomodifier - ND, identical refinement of the primary Si crystals was observed, while the refinement of the sizes of the silicon crystals in the eutectic composition differ significantly. For the alloy modified by phosphorus the refinement of the Si crystals in the composition of the eutectic is 51% and for the ND- modified alloy the refinement is 94% compared to the unmodified alloy. The formation of such a finely dispersed structure is probably due to the modifying influence of the nanodiamonds on the eutectic of the alloy.

The tensile strength (Rm) of a phosphorus modified and a ND modified hypereutectic AlSi18 aluminum-silicon alloy, as well as the relative elongation (plasticity) increase respectively with 18.5% and 14.3% for the phosphorus - modified and with 20.3% and 7.1% for the ND - modified alloy. This is due to the reduced notch effect exerted by the modified primary silicon crystals on the alloy structure, as well as to the finely dispersed structure of the modified eutectic in which the primary Si crystals are located. The macro-hardness of the alloy modified by phosphorus increases by 1.5% while the same value decreases by 6.2% for the ND - modified alloy.

The obtained results show that the modification of AlSi18 alloy by a nanomodifier ND can successfully replace its modification by a standard phosphorus (P) modifier. This will have an ecological effect and will improve the hygienic working conditions in foundries, using this alloy.

5. References

1. Cherepanov A.N., managing editor Fomin V.M., 1995, Plasma-chemical synthesis of ultradisperse powders and their application in metal and alloy modification, Low-temperature plasma, volume 12, Novosibirsk, Science, Syberian Publishing Company RAS, 1995, p.344;
2. Bojanova N., V. Kovachev, I. Panov, V. Manolov, R. Lazarova. "The effect of nanodisized powders on the electrochemical parameters of a protecting aluminum alloy." Collection of reports from the Third National Conference with international participation "Metal Science, Hydro and Aerodynamics, National Safety' 2013 ", ISSN 1313-8308, No. 1.30, pp. 151-157;
3. J. Kaleicheva, V. Mishev, G. Avdeev, Z. Karaguiozova, B. Dineva, Influence of nanoadditives on the structure and properties of austempered ductile irons, Proceedings in European Conference on Heat Treatment and 21st IFHTSE Congress, 12 -15 May 2014, Munich, Germany.
4. V. Yu. Dolmatov, On the mechanism of detonation nanodiamond synthesis Journal of Superhard Materials, August 2008, Volume 30, Issue 4, pp 233–240
5. Kalinina A.P., A.N. Cherepanov, V.A. Poluboyarov, Z.A. Korotaeva, Mathematical model of nucleation in liquid metals on ultrafine ceramic particles. - Journal of Physical Chemistry, 2001, v. 75, No. 2, 283-289 .; 0.088;
6. Kalinina N.E., Kalinin V.T., Nanomaterials and nanotechnologies: production, structure, application, Monography, Dnepropetrovsk, Makovetskij Y. V. Publishing House, 2012, p. 188;
7. Bozhanova N.M., I.T. Panov, V.K. Manolov, A.N. Cherepanov, R.L. Lazarova Thermophysics and Aeromechanics, 2018, Volume 25, No. 5, UDC 541.13 (076.5), Modification of the properties of aluminum protecting anodes by nanopowder materials;
8. Lazarova R., N. Bojanova, R. Dimitrova, I. Panov & V. Manolov, „Influence of Nanoparticles Introducing in the Melt of Aluminum Alloys on Castings Microstructure and Properties", International Journal of Metalcasting, 2016, Vol. 10, Issue 4, 466-476;
9. Manolov V., Cherepanov, A., Lazarova R., Konstantinova S., Effect of nanopowder inoculars on the structure and properties of AlSi7Mg alloy, Foundry - M., 2011, No. 11, 11-14, ISSN: 0024-449X, IF
10. Marina Khmeleva, Anton Khrustalev and Alexander Vorozhtsov, Structure and mechanical properties of A356-C alloy, MATEC Web of Conferences 243, 000 (2018), https://doi.org/10.1051/matecconf/201824300024

The work is supported by a Project under Contract Agreement No DN07/20/15.12.2016, funded by the Bulgarian Scientific Research Fund.

AN ALLOY FOR ACCUMULATION OF HYDROGEN WITH STRUCTURE OF LAVES PHASE AND BCC SOLID SOLUTION FOR THE NEEDS OF ALTERNATIVE ENERGY

СПЛАВ АККУМУЛЯТОР ВОДОРОДА СО СТРУКТУРОЙ ФАЗЫ ЛАВЕСА И ОЦК-ТВЕРДОГО РАСТВОРА ДЛЯ НУЖД АЛЬТЕРНАТИВНОЙ ЭНЕРГЕТИКИ

PhD Dekhtyarenko V.*, PhD Pryadko T., PhD Bondarchuk V., PhD Mogylnyy G., PhD. Khranovskaya E.
G. V. Kurdyumov Institute for Metal Physics of the N.A.S. of Ukraine - Kyiv, Ukraine
*E-mail: Devova@i.ua

Abstract: *The microstructure and phase composition of $Ti_{47,5}Zr_{30,2}Mn_{15,5}V_5Ho_2$ multiphase alloy and the phase composition of the hydrogenation product were investigated by scanning electron microscopy and X-ray phase analysis. It was established that holmium introduced into the alloy not only dissolves in the phase components of the eutectic, but also forms a new phase (oxide). The formation and further growth of crystals of holmium oxide occurs only on the surface of the crystallites of Laves phase. During the first hydrogenation the active absorption of hydrogen by the alloy occurred only when it was heated up to 520 °C, with hydrogen capacity of 2.62 wt.%. The hydrogenation product obtained after the saturation of the alloy with hydrogen contained a new phase, in addition to the hydrides based on the initial phases. After the sorption-desorption cycle, the alloy was already in the activated state and able to absorb hydrogen at room temperature and low pressure (0.21 MPa) starting from the first seconds of contact with the hydrogen medium.*

KEYWORDS: LAVES PHASE, BCC SOLID SOLUTION, MULTIPHASE ALLOY, OXIDE, SORPTION / DESORPTION, HYDROGEN CAPACITY.

1. Introduction

Currently, due to the rapid development of hydrogen energy and the active use of hydrogen in the automotive industry, the search for new materials for safe storage and transport of hydrogen in a bound state (hydrides) is promising [1]. Particular attention is paid to the alloys based on the Laves phase $TiMn_2$, since the alloys of this system have a fairly high sorption capacity H/Me ≈ 1 [2] and are easily activated [3].

The effect of vanadium on the structure, phase composition and hydrogen capacity of Ti-Mn alloys with the structure based on BCC solid solution and Laves phase was investigated in [4]. It was found that introduction of vanadium into the alloys led to an increase of the fraction of BCC solid solution, and consequently an increase in the amount of absorbed hydrogen.

In [5], the alloys $TiMn_{(100-x,\ Ti\ /\ Mn\ =\ 5/8)}V_x$ where (x = 25, 30, 35, 40, 45 and 50) with the structure of BCC solid solution and Laves phase were studied, as in work [4] It was shown that an increase in the content of vanadium led to an increase of volume fraction of BCC solid solution. The lower volume of Laves phase led to an increase in the number of sorption-desorption cycles required to achieve the maximum possible hydrogen capacity. The authors explained this by the fact that the Laves phase, due to its increased brittleness, facilitates saturation of the BCC solid solution.

In [6], the alloys $Ti_{0.7}Zr_{0.3}(Mn_{1-x}V_x)_2$ alloys where (x = 0.1, 0.2, 0.3, 0.4, 0.5) were investigated. It was found that up to vanadium content x = 0.2 the alloys were in a single-phase state with Laves phase structure, whereas at $x \geq 0.3$ BCC solid solution appeared. The increment of concentration of vanadium led to an increase in the amount of absorbed hydrogen and an increase in the resistance to oxygen poisoning.

We have previously investigated how the replacement of non-hydride-forming manganese by 5 at. % of vanadium in the eutectic alloy of the Ti-Zr-Mn system with the structure of Laves phase and BCC solid solution influenced its structure and hydrogen capacity [7]. It was shown that the introduction of vanadium into the alloy changed its structure from eutectic to pre-eutectic, and primary crystallites of BCC solid solution appeared, which in turn led to an increase in hydrogen capacity.

The authors [8] investigated the hydrogen adsorption properties of $Ti_{1.02}Cr_{1.1}Mn_{0.3}Fe_{0.6}REM_{0.03}$ alloy (REM – La, Ce, Ho) which can be used as a hydrogen storage material. It was found that in the initial state the alloy was in a single-phase condition with the structure of Laves phase, and after adding REM a second phase (REM-based oxide) appeared. The REM additions led to an increase in the volume of the unit cell, and consequently to an increase in the amount of hydrogen absorbed as well as improvement in the sorption and desorption processes. The authors claimed that after alloying with REM the material was able to absorb hydrogen at room temperature and hydrogen pressure of 34-43 MPa to a capacity of 1.715 wt.%.

The goal of the present work was to establish the effect of the introduction of REM on the structure, phase composition and hydrogen sorption properties of the pre-eutectic alloys of Ti-Zr-Mn-V system. To establish this effect, a previously investigated pre-eutectic $Ti_{47.5}Zr_{30}Mn_{17.5}V_5$ alloy was selected with the structure of primary crystallites of BCC solid solution and eutectic component, in which the non-hydride-forming manganese was replaced by 2 at. % REM (Holmium). Holmium was selected as an alloying element for the following reasons: it is a hydride-forming element; it has a much larger atom size than manganese (atomic radii 0.179 and 0.127 nm, respectively) [9]; finally, holmium is used as a deoxidizer.

2. Materials and methods

The alloy was produced by electric arc melting in a laboratory furnace with a non-consumable tungsten electrode in atmosphere of purified argon. Iodide Ti (99.9%), iodide Zr (99.975%), electrolytic Mn (99.9%), electrolytic V (99.9%), and Ho (99.9%) were used as initial components. The deviation of chemical composition of the alloy from the nominal one was determined by XRF (VRA-30 unit). It coincided with the nominal one within the measurement error (0.03%).

Metallographic examinations were performed with a scanning electron microscope VEGA3 TESCAN equipped with EDX detector XFlash610M (Bruker).

The phase composition and lattice parameters were determined by X-ray phase analysis at a Dron-3M diffractometer with a standard GUR-8 goniometer at monochromatic Cu-K_α.

The hydrogen adsorption properties were studied on the alloy in a cast solid state. The interaction of the alloy with hydrogen was studied by the Sieverts method at IVGM-2M unit [10] at room temperature and upon heating at a rate of 0.125 °C/s and isothermal holding at T = 550 °C and absolute pressure ~ 0.6 MPa, as for the previously studied alloy. The amount of hydrogen absorbed was calculated from the change in pressure in a closed volume and was determined by weighing on the VLR 20 scales with an accuracy of 1.5×10^{-5} g. The tunnel crucibles were used to prevent loss of sample mass during the reactor evacuation to carry out the desorption process.

3. Results and discussion

The microstructures of initial alloy and alloy with Ho are shown in Fig. 1. As seen, the partial replacement of manganese with holmium changed the structure of the investigated $Ti_{47.5}Zr_{30}Mn_{15.5}V_5Ho_5$ alloy from pre-eutectic to multiphase one.

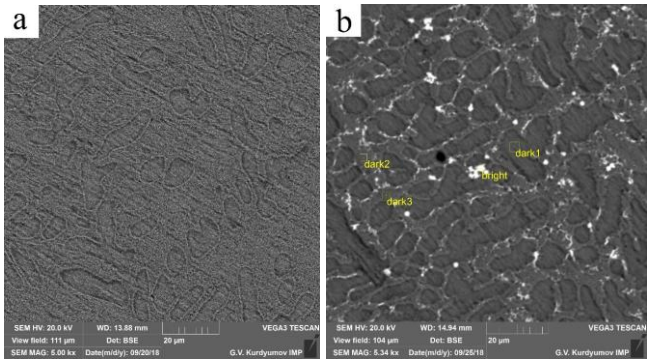


Fig. 1. *Microstructure of cast alloy: a – initial, b – alloyed with Ho.*

In the alloy with Ho three phases can be clearly distinguished (Fig. 1.b). For the identification of the phases, their chemical composition was determined by EDX method. Dark gray crystallites (dark 1) had the following composition: 63.31Ti-29.5Zr-4.49Mn-1.96V-0.74Ho (at.%). Taking into account the previous studies [11] and the determined chemical composition, it can be concluded that this is BCC solid solution. The chemical composition of light gray crystallites (dark 2 and dark 3) was 45.84Ti-27.57Zr-20.98Mn-5.29V-0.32Ho (at.%) which corresponds to the intermetallic phase. In the white (bright) zones the composition was 62.49Ho-2.55Ni-34.96O (at.%) which corresponds to holmium oxide.

The volume fraction of the phases was calculated by means of ImageJ program. It was found that the alloy contained 7.74% of holmium oxide, 45.45% of the Laves phase, and 46.81% of the BCC solid solution.

As seen from the microstructure (Fig. 1.b), the particles of holmium oxide are located only on the surface of intermetallic crystallites. This can be explained by the fact that the crystallites of Laves phase have a higher solidus as compared to the BCC solid solution [11], and therefore they act as sites of solidification for holmium oxide.

X-ray phase analysis confirmed the data of scanning electron microscopy about the phase composition of the alloy (Fig. 2). The alloy comprised hexagonal Laves phase of C14 type of space group *$P6_3/mmc$* (structural type $MgZn_2$) with unit cell parameters a = 0.5194 ± 0.0009 (nm), c = 0.8533 ± 0.0009 (nm) (in previous study a = 0.5186 ± 0.0009 (nm), c = 0.8519 ± 0.0009 (nm), see [7]), and BCC solid solution of *1m-3m* space group (structural type W) with unit cell parameter a = 0.3375 ± 0.0009 (nm) (in previous study a = 0.3366 ± 0.0009 (nm), [7]). The SEM data on the presence in the alloy of holmium oxide with unit cell parameter a = 1.0274 ± 0.0009 (nm) were confirmed, and traces of holmium and HoF_3 were detected. It can be assumed that the presence of the HoF_3 phase in the alloy is related to the residues left after the production process, as holmium is obtained by the reduction of HoF_3 by calcium.

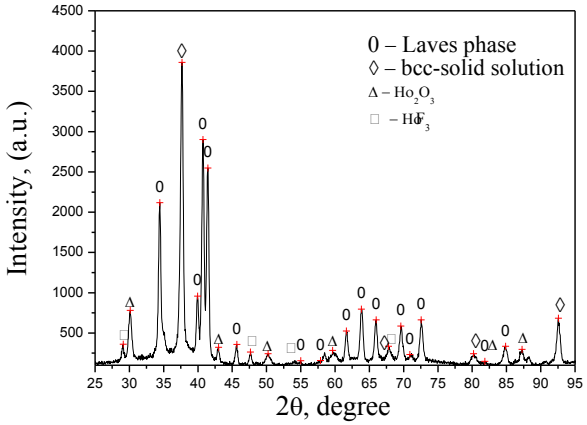


Fig. 2. *Diffraction pattern of cast $Ti_{47,5}Zr_{30}Mn_{15,5}V_5Ho_2$ alloy.*

A comparison of the lattice parameters of the Laves phase and the BCC solid solution for the alloyed and unalloyed alloy allows to conclude that alloying with holmium does not lead to a significant increase in the crystal lattice parameter and accordingly the size of tetrahedral voids which accommodate hydrogen atoms, as the major portion of holmium is contained in the new phase.

According to the JCPDS (International Center for Diffraction Data), the lattice parameter of holmium oxide of stoichiometric composition Ho_2O_3 equals 1.0606 nm. Given the chemical composition and the resulting lattice parameter for Ho_2O_3, as well as the presence of some amount of holmium outside oxide, one can assume that all the available oxygen was bound upon processing of the alloy, and it was insufficient to produce stoichiometric oxide.

The test alloy was maintained at room temperature and an absolute hydrogen pressure of 0.6 MPa for 24 hours, but these hydrogenation conditions did not lead to activation of surface and noticeable absorption. Previously we have shown that upon annealing the intermetallic crystallites grew, and the active area for the dissociation of hydrogen molecules increased, which led to a decrease in the temperature of active absorption of hydrogen by $Ti_{47.5}Zr_{30}Mn_{17.5}V_5$ alloy from 450 °C to room temperature [12]. The test alloy had a much larger average size of crystallites of the Laves phase than the alloy without Ho (Fig. 1.); nevertheless, noticeable hydrogen absorption at room temperature did not occur. The absence of absorption at room temperature can be explained by the presence on the surface of intermetallic phase, natural oxide film, and particles of holmium oxide Ho_2O_3, which reduced the catalytic ability of the surface and formed a barrier layer for hydrogen penetration.

The active absorption of hydrogen was recorded only after heating up to 550 °C. By the deviation of the dependence of change in pressure on temperature from the linear line it was found that the temperature of onset of intense hydrogen absorption by the ties

alloy upon the first hydrogenation equaled ~ 470 °C, whereas for the previously studied alloy it was ~ 450 °C (Fig. 3). The increase in the temperature of active hydrogen absorption by the test alloy is explained by the presence of holmium oxide which covered the surface of other phase components, thereby reducing the active area for dissociation of hydrogen molecules. At a temperature of 520 ± 10 °C the major amount of hydrogen was absorbed by $Ti_{47.5}Zr_{30}Mn_{15.5}V_5Ho_2$ alloy in ~ 15 min, whereas for $Ti_{47.5}Zr_{30}Mn_{17.5}V_5$ alloy this time equaled ~ 40 min [7].

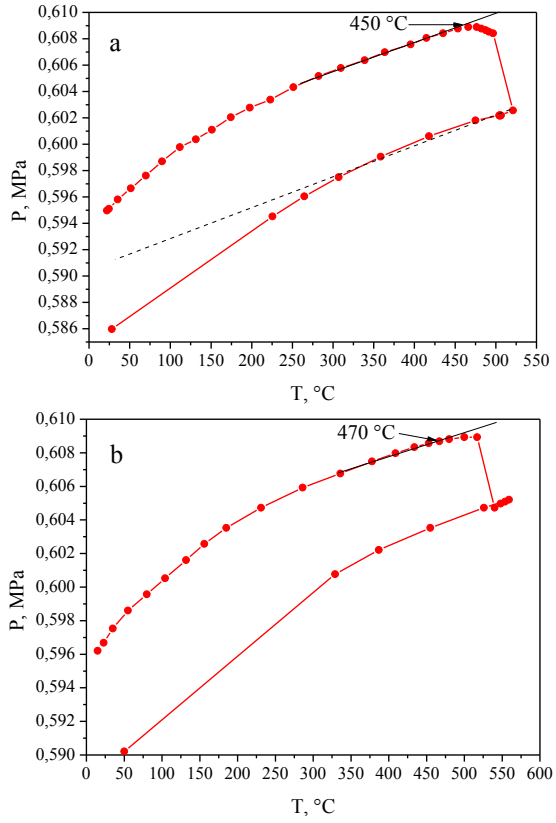


Fig. 3. *Dependence of hydrogen pressure on temperature upon first hydrogenation: a – initial alloy, b – alloy with Ho.*

The reduction in the time to reach the maximum possible hydrogen capacity in $Ti_{47.5}Zr_{30}Mn_{15.5}V_5Ho_2$ alloy can be explained by the different size of the BCC solid solution crystallites. Previously we have shown [7] that the active absorption of hydrogen upon heating starts in the crystallites BCC solid solution. As can be seen from Fig. 1, the test alloy had coarser crystallites of BCC solid solution, and correspondingly higher catalytic ability on the surface.

The total hydrogen capacity of $Ti_{47.5}Zr_{30}Mn_{15.5}V_5Ho_2$ alloy was 2.62 wt.% (H/Me = 1.72), whereas for the previously studied alloy it equaled 2.85 wt.% (H/Me = 1.81) [7]. Recalculation of the measured hydrogen capacities only for the Laves phase and the BCC solid solution allows to suppose that their hydrogen capacities remained unchanged. The decrease in the total amount of hydrogen absorbed by the test alloy is due to the presence of oxide Ho_2O_3 which does not interact with hydrogen, and at the same time makes a significant contribution to the mass of the alloy.

According to the X-ray phase analysis (Fig. 4), the saturation of $Ti_{47.5}Zr_{30}Mn_{15.5}V_5Ho_2$ alloy with hydrogen led to formation of δ-hydride with lattice parameter a = 0.4585 ± 0.0009 (nm), a hydride based on the Laves phase of C14 type with a = 0.5575 ± 0.0009 (nm) and c = 0.9157 ± 0.0009 (nm), and holmium HoH_3 hydride with a = 0.6307 ± 0.0009 (nm) and c = 0.6569 ± 0.0009 (nm). Beside these hydrides, there was holmium oxide with a significantly larger lattice parameter a = 1.0571 ± 0.0009 (nm), as well as reflexes (2θ = 30.65 and 36) which did not correspond to any of the phases indicated (Fig. 4). At present, it is not possible to unambiguously interpret and explain the mechanisms and reasons for the formation of a new phase during saturation of the alloy with hydrogen.

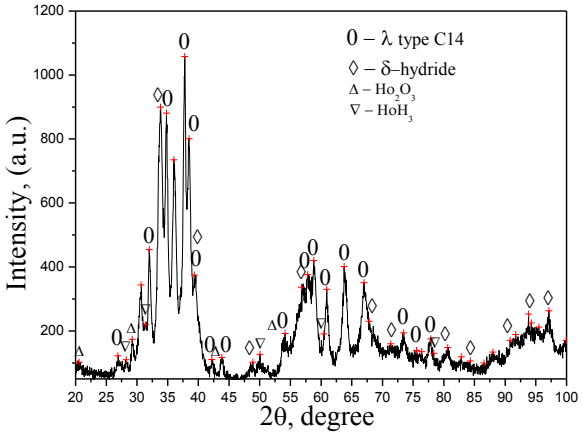


Fig. 4. *Diffraction pattern of hydrogenated $Ti_{47.5}Zr_{30}Mn_{15.5}V_5Ho_2$ alloy.*

The X-ray phase analysis showed that after heating in vacuum to a temperature of 500 °C it was possible to obtain 100% reverse capacity (Fig. 5). After hydrogen desorption, the diffraction patterns contained the reflexes of the following phases: the BCC solid solution with lattice parameter a = 0.3378 ± 0.0009 (nm), the Laves phase of C14 type a = 0.5216 ± 0.0009 (nm) and c = 0.8568 ± 0.0009 (nm), the holmium with a = 0.3601 ± 0.0009 (nm) and c = 0.5689 ± 0.0009 (nm), and the new phase (2θ = 32.8 and 38.8), as well as Ho_2O_3 with a = 1.0599 ± 0.0009 (nm).

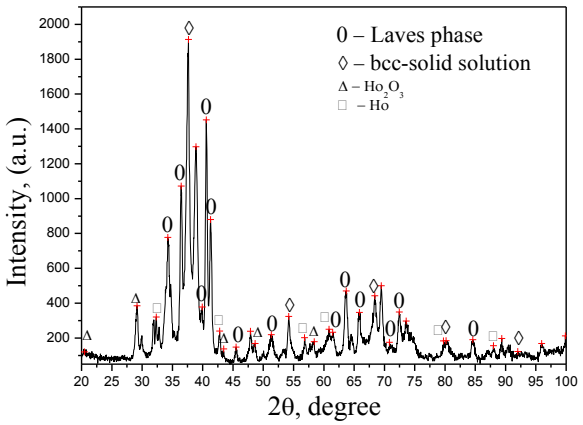


Fig. 5. *Diffraction pattern of $Ti_{47.5}Zr_{30}Mn_{15.5}V_5Ho_2$ alloy after hydrogen desorption.*

It is clear from Fig. 5 that after hydrogen desorption the reflexes of the new phase remained (2θ = 32.8 and 38.8), but their intensity significantly decreased. These data allow to assume that hydrogen desorption resulted in a re-dissolution of the new phase. A comparison of the angles 2θ for the new phase after hydrogenation (2θ = 30.65 and 36) and dehydrogenation (2θ = 32.8 and 38.8) shows that the new phase was also a hydride. It can be assumed that the complete dissolution of the new phase during hydrogen desorption did not occur due to insufficient holding time upon heating.

The investigation of the effect of sorption/desorption/sorption cycling on the hydrogen sorption properties of the alloy under study showed that the hydrogenation at the second and subsequent cycles occurred already at room temperature and hydrogen pressure of 0.21 MPa starting from the very first seconds of contact of the sample with the hydrogen medium. Based on the hydrogenation temperature, it can be assumed that in this case the absorption of hydrogen already begins in the Laves phase [13]. This improvement of the hydrogen sorption properties of the alloy can be explained by the transformation of a bulk sample into powder, as well as by the decrease of oxygen concentration on the surface of the particles as a result of its interaction with released atomic hydrogen, and by additional precipitation of Ho_2O_3.

According to the X-ray data (Fig. 6), after the sorption-desorption cycles the phase composition of the hydrogenation product remained the same as upon the first hydrogenation.

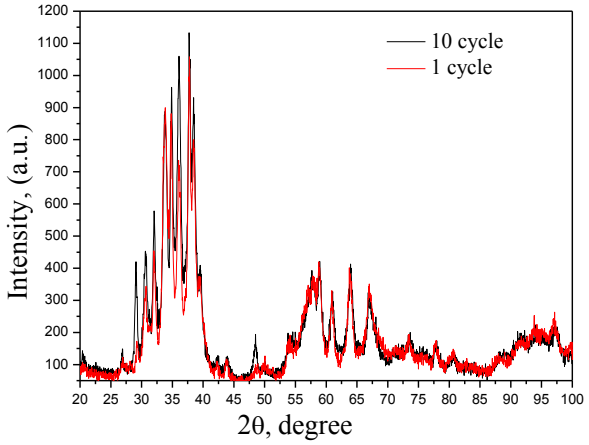


Fig. 6. *Diffraction pattern of $Ti_{47.5}Zr_{30}Mn_{15.5}V_5Ho_2$ alloy after ten cycles of hydrogen sorption-desorption.*

After ten cycles of hydrogen sorption-desorption the diffraction pattern comprised the reflexes of the following phases: δ-hydride with lattice parameter a = 0.4585 ± 0.0009 (nm), the Laves phase of C14 type with a = 0.5571 ± 0.0009 (nm) and c = 0.9151 ± 0.0009 (nm), the new phase (2θ = 30.64 and 36.08), holmium hydride with a = 0.6338 ± 0.0009 (nm) and c = 0.6591 ± 0.0009 (nm), and Ho_2O_3 with a = 1.0635 ± 0.0009 (nm).

A comparison of the diffraction patterns after one hydrogenation and ten cycles of hydrogen sorption-desorption (Figs. 4 and 6) showed that after 10 cycles the intensity of the reflexes of the Laves phase C14, the new phase (2θ = 30.64 and 36.08), and the oxide significantly increased; at the same time, the intensity of δ-hydride reduced. Considering the lattice parameter of holmium oxide after one hydrogenation and ten cycles, one can assume that during the sorption-desorption cycles the sample was further purified from previously dissolved oxygen.

4. Conclusions

1. The holmium introduced into the pre-eutectic alloy of the Ti-Zr-Mn-V system not only dissolves in the phase components of the eutectic, but also forms a new phase and thereby changes the phase composition and structure of the initial alloy.

2. The cycles of hydrogen sorption-desorption allow to reduce the active absorption temperature from 520°C to room temperature, and the hydrogen pressure from 0.6 to 0.21 MPa.

3. After saturation with hydrogen, the hydrides on the basis of initial phases, as well as a new phase formed.

5. References

1. Fundamental aspects of renewable-hydrogen energy and fuel cell technologies / general edited by Yu.M. Solonin - K.: "KIM", 2018 260 p (in Ukrainian).

2. H. Taizhong, W. Zhu, Y. Xuebin, C. Jinzhou, X. BaoJia, H. Tiesheng, X. Naixin, Hydrogen absorption–desorption behavior of zirconium-substituting Ti–Mn based hydrogen storage alloys *Intermetallics*, **12**, No.2: 2004, p. 91-96. https://doi.org/10.1016/j.intermet.2003.08.005

3. X. Yu, B. Xia, Z. Wu, N. Xu**,** Phase structure and hydrogen sorption performance of Ti–Mn-based alloys *Materials Science and Engineering A*, **373**, No. 1-2: 2004, p. 303-308. https://doi.org/10.1016/j.msea.2004.02.008

4. H. Taizhong, W. Zhu, S. Guoxin, X. Naixin, Microstructure and hydrogen storage characteristics of $TiMn_{2-X}V_X$ alloys *Intermetallics*, **15**: 2007, p. 593-598. https://doi.org/10.1016/j.intermet.2006.10.035

5. X. Y. Chen, R. R. Chen, X. Ding, H. Z. Fang, J. J. Guo, H. S. Ding, Y. Q. Su, H. Z. Fu, Crystal structure and hydrogen storage properties of Ti-V-Mn alloys *Int. J. Hydrogen Energy*, **43**, No.12: 2018, p. 6210-6218. https://doi.org/10.1016/j.ijhydene.2018.02.009

6. M. Ping, W. Erdong, L. Wuhui, Hydrogen storage properties and microstructures of $Ti_{0.7}Zr_{0.3}(Mn_{1-x}V_x)_2$ (x = 0.1, 0.2, 0.3, 0.4, 0.5) alloys *Int. J. Hydrogen Energy*, **39**, No.25: 2014, p. 13569-13575. https://doi.org/10.1016/j.ijhydene.2014.03.178

7. V. G. Ivanchenko, V. A. Dekhtyarenko, T. V. Pryadko, Hydrogen Sorption Properties of $Ti_{0.475}Zr_{0.3}Mn_{0.225}$ Eutectic Alloy Alloyed with 2 at.% and 5 at.% of Vanadium, *Metallofiz. Noveishie Tekhnol.*, **37**, No. 4: 2015, p. 521-530. https://doi.org/10.15407/mfint.37.04.0521

8. Z. Yao, L. Liu, X. Xiao, C. Wang, L. Jiang, L. Chen, Effect of rare earth doping on the hydrogen storage performance of $Ti_{1.02}Cr_{1.1}Mn_{0.3}Fe_{0.6}$ alloy for hybrid hydrogen storage application *J. Alloys Compd.*, **731**: 2018, p. 524-530. https://doi.org/10.1016/j.jallcom.2017.10.075

9. A. V. Manujlov, V. I. Rodionov, *Osnovi khimii*, I-vo "Centrpoligraf", 2016 (in Russian).

10. G. F. Kobzenko, A. A. Shkola, Reactor for the studying of metal-gas reaction *Materials diagnostics*, **56**: 1990 p. 41-45 (in Russian).

11. V. G. Ivanchenko, V. A. Dekhtyarenko, T. V. Pryadko, and V. I. Nychyporenko, Influence of V on the Structure and Phase Composition of Eutectic $Ti_{0.475}Zr_{0.3}Mn_{0.225}$ Alloy, *Metallofiz. Noveishie Tekhnol.*, **36**, No.6: 2014 p. 803—813 (in Russian). https://doi.org/10.15407/mfint.36.06.0803

12. V. G. Ivanchenko, V. A. Dekhtyarenko, T. V. Pryadko, D. G. Savvakin, I. K. Evlash, Influence of Heat Treatment on the Hydrogen-Sorption Properties of $Ti_{0.475}Zr_{0.3}Mn_{0.225}$ Eutectic Alloy Doped with Vanadium, *Materials Science*, **51**, No. 4 2016, p. 492-499. https://doi.org/10.1007/s11003-016-9867-7

13. V. G. Ivanchenko, V. A. Dekhtyarenko, T. V. Pryadko, Sorption properties of heterophase alloys β(Ti,Zr,Mn)+(Ti,Zr)Mn_{2-x}, *Metallofiz. Noveishie Tekhnol.,* **33**, spets. vyp.: 2011 p. 479-484 (in Russian).

ON THE EFFECT OF INTERMEDIATE PRESSING OF PREFORMS ON THE FORMATION OF A DEFECT-FREE STRUCTURE OF FINISHED PRODUCTS FROM CARBON FIBER-FILLED POLYTETRAFLUOROETHYLENE

Assoc. Prof. Voropaev V.V. PhD[1], Assoc. Prof. Skaskevich A.A. PhD[1], Senior lecturer Lesun A.N.[1],
Assoc. Prof. Sarokin V.G.[1], PhD Yankov E.[2]
Yanka Kupala State University of Grodno, Belarus[1]
E-mail: voropaev_vv@grsu.by, askas@grsu.by, lesun_an@grsu.by, sorvg63@mail.ru
University of Ruse 3 – Bulgaria[2]
E-mail: eyankov@uni-ruse.bg

Abstract: *This article describes a method for producing composite materials based on polytetrafluoroethylene with high performance properties. One of the obstacles to achieve this result had been the accumulation of moisture in the semi-finished product, which subsequently led to the appearance of defects in products made of fluorine composites. It is proposed to produce semi-finished preforms under reduced specific pressure, in which the moisture content is easier, cheaper and more efficient to control than with the current technological regulations. It is shown that the use of these semi-finished preforms allows getting almost defect-free products with high performance characteristics.*

Keywords: *INTERMEDIATE PRESSING, POLYTETRAFLUOROETHYLENE, CARBON FIBER, PREFORM, APPARENT DENSITY, MOISTURE, PORES*

1. Introduction

Gas compressors operating without the use of lubricant are applied in all industries where according to the requirements of the technology pure gas without lubricant impurities is required. In the vast majority of cases such compressors have an expensive, complex and material-intensive design, in which the seals occupy only a small part. Despite the relatively small specific gravity of the sealing elements in the cost of compressors, the resource, uninterrupted and safety operation of the whole mechanism largely depend on their properties.

The desire to obtain a sealing material with high strength and tribotechnical characteristics has led to widespread use of composite materials based on polytetrafluoroethylene (PTFE) with carbon fiber fillers in the design of compressor assemblies without lubricants.

2. Prerequisites and means for solving the problem

The foundations of the manufacturing technology of composite materials based on PTFE were developed in the 1960s, and the production of fluorocomposites with carbon fiber fillers has been actively developing since the 1980s. Among the post-Soviet countries the most wide known antifriction material with the commercial name is “Flubon”. Sirenko [1] has defined it as a polymer composite material based on polytetrafluoroethylene, copolymers of ethylene and tetrafluoroethylene and other fluorinated polymers, modified carbon fibers and other fibrous and dispersed fillers [1]. Since practically all currently known composite materials based on polytetrafluoroethylene with carbon fiber fillers fall under this description, regardless of the technology of their production and the exact composition, then in the future for the purposes of this article we will talk about Flubon and its analogues.

According to [2], the production technology of composite materials like “Flubon” consists of the following stages:

1) preparation of a semi-finished composite material, including operations of shredding of a carbon tape to a powder state with regulated apparent density and mixing the obtained product with other components of the composite;

2) disposal of moisture from the semi-finished composite material;

3) pressing of workpieces;

4) heat treatment of workpieces by volumetric heating in an electric furnace.

Changing the parameters of the technological process’ stages we can affect the performance characteristics of PTFE-based composite materials. There are several methods that improve the performance characteristics of materials like "Flubon", which can be used at the stage of preparation of the semi-finished composite material: mechanical activation of a semi-finished product on rubber-processing rollers [3], mixing the ingredients in a bladed mixer with modernized blades (choppers) [4], plasma-chemical modification of the carbon filler in order to form on its surface a layer of fluoropolymer some dozens of nanometers thick [5].

The authors [6] submit that at least two principally different approaches are possible at the heat treatment stage: free sintering, which is traditional, and sintering under conditions of limitation the volume of thermal expansion at the stage of transition of PTFE into a viscous-flow state.

At the same time researchers pay relatively little attention to the development of pressing methods that can effectively influence the performance characteristics of manufactured PTFE-based composite materials, although this operation is one of the most capital-intensive and has a significant impact on the performance characteristics of future products. The authors [7] have proposed a pressing method assuming the combination of this operation with the impact of ultrasonic on the semi-finished composite, however, the obtained values of strength and tribotechnical characteristics are inferior to materials that are already available on the market. Thus, the task to modernize the pressing operation in the manufacturing process of composite materials like “Flubon” remains urgent.

The complexity of the task is that the semi-finished PTFE-based composite material with carbon fiber fillers is hard to press due to poor adhesion between particles of polymer and filler. Moreover, compressibility worsens with the rise of the filler content in the composition and the size of its particles. In addition, the carbon fiber is a hygroscopic filler and is capable to adsorb up to 7 massive percent of moisture from the air, which must be removed from the semi-finished composite material through a drying operation in the technological process. At the same time, the discrete nature of the technological process often makes senseless the energy-intensive drying operation, since the prepared semi-finished composite material often waits pressing from several hours to several days, accumulating moisture from the air again. As a result, in the future the absorbed water is stored in the volume of a workpiece during pressing operation, creating additional obstacles for obtaining the defect-free composite. Thus, favorable conditions are created for appearance of pores or even cracks in the workpieces at high temperatures of heat treatment due to evaporation of the moisture contained in the workpiece. Naturally, this adversely affects the performance characteristics of the composite material. Billets of products are obtained with low density and insufficient strength characteristics.

Attempts to use non-hygroscopic trademarks of carbon filler also led to poor strength characteristics of products. The reason is that as non-hygroscopic carbon filler graphitized carbon fibers with a high class of heat treatment (1900–2200 Cº) were used. This type of carbon fiber has a dominating fraction size of less

than 50 microns after shredding (more than 90 massive percent of filler), therefore filler has not a reinforcing effect.

3. Solution of the examined problem

The possibility to modernize the pressing operation in the technological process of composite materials based on PTFE filled with discrete carbon fibers was studied. During the study a method was developed that involved an operation of preliminary pressing of semi-finished preforms at specific pressure of 5-20 MPa, which later allowed to produce low-porous workpieces with a percentage of fillers of 20–35 massive percent.

The proposed options for the pressing operation are as follows (Fig. 1):

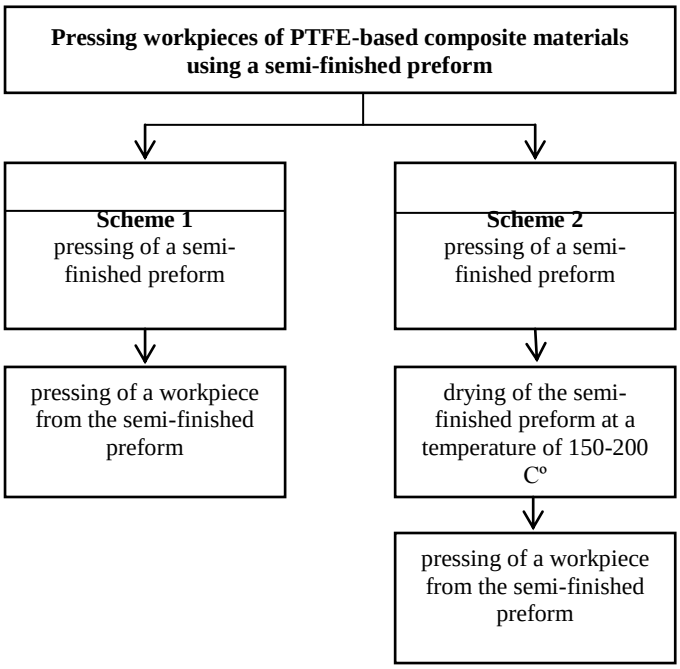


Fig. 1 *– Schemes for pressing workpieces of PTFE-based composite materials using the step of obtaining a semi-finished preform*

The semi-finished product obtained as a result of the intermediate pressing operation is a highly porous semi-finished preform. The semi-finished preform is also much lighter and larger than a workpiece of similar mass obtained by traditional pressing mode (see Fig. 2).



a b

Fig. 2 *– The appearance of the preforms of products from PTFE-based composite materials: a) semi-finished preform; b) finished workpiece*

The high porosity of the semi-finished preform allows the moisture enclosed in the volume of the workpiece to get out in the external environment during due to evaporation when storing. But it is much faster and more reliable to remove moisture from the semi-finished preform by drying the workpiece at a temperature of 150–200 Cº. This is due to the fact that at the drying temperature a guaranteed removal of moisture from the semi-finished preform occurs via intensive vaporization. Unlike this, removal of moisture is difficult at sintering of workpieces, pressed at specific pressure of 60-80 MPa in accordance with the requirements of the existing technical regulations of the manufacturers of composite materials based on PTFE filled with discrete carbon fibers, due to isolation of carbon fibers in polymer matrix.

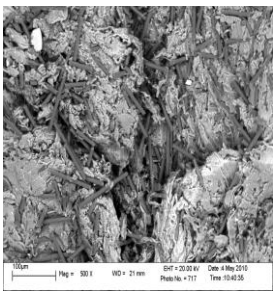
The moisture absorption measurements of the semi-finished preforms show that the semi-finished preform absorbs more than 99% all possible moisture from the air during the first 5 hours after drying. At the same time, the increase in the specific pressure of pressing semi-finished products from 5 to 20 MPa slows down the rate of moisture absorption after drying by only 0.2%, and the absolute humidity of the semi-finished preform 24 hours after drying in both cases was 1.79%, which corresponds to the initial level. Such results mean that it is necessary to perform the operation of finishing pressing the preform at specific pressure of 60-80 MPa immediately after drying of the semi-finished preforms, or repeat drying when the semi-finished preforms wait finishing pressing more than 1-2 hours.

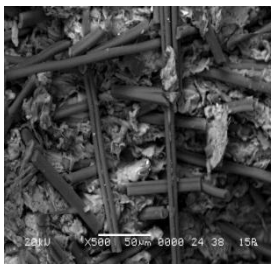
To make possible longer breaks in the technological process, the following operation was proposed. After drying, the semi-finished preforms were dipped in industrial oil to obtain a moisture-proof film that prevents re-absorption of moisture. It has been proven that treating the semi-finished preforms with industrial oil after drying reduces moisture absorption, since their absolute humidity 24 hours after drying was only 0.3%. Moreover, it turned out that at the same absolute humidity the oil consumption for semi-finished preforms obtained at specific pressure of 20 MPa is two times lower than for semi-finished preforms obtained at specific pressure of 5 MPa. It follows from this that it is desirable to obtain semi-finished preforms at a lower pressure without using an operation of treatment in industrial oil, and at a higher pressure – using such an operation, since this will lead to a reduction in energy costs in the first case and oil costs decrease – in the second case.

Thus, the introduction of an intermediate pressing of semi-finished preforms followed by drying and processing in industrial oil can significantly increase the interoperational storage period in the technological process and reduce the negative effect of absorbed moisture on the performance characteristics of PTFE-based composite materials.

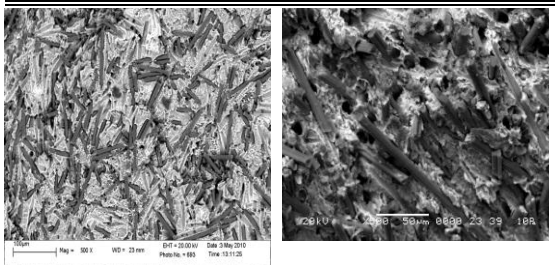
4. Results and discussion

The effect of intermediate pressing on the internal structure of preforms and finished PTFE-based composite materials was evaluated by SEM images of the surface of fragments, which had been obtained through chipping of samples after liquid nitrogen exposure (Fig. 3):





workpiece before sintering (scale x500)



Workpiece without pressing operation — obtained Workpiece after intermediate pressing operation — obtained from the semi-finished preforms sintering (scale x500)

Fig. 3 *– Surface morphology of samples' fragments of PTFE-based composite materials with various pressing methods*

Analyzing the results of scanning electron microscopy we can conclude that, when using intermediate pressing, the number of regions with an uneven distribution of filler particles in the polymer matrix is significantly reduced. We can also observe an increase of the contact area between the polymer and individual filler particles. Thus, the introduction of intermediate pressing operation into the technological process of obtaining PTFE-based composite materials leads to the formation of a more homogeneous structure in comparison with existing technical regulations of the manufacturers of composite materials based on PTFE filled with discrete carbon fibers.

The influence of intermediate pressing on obtaining the defect-free PTFE-based composite materials also was determined by the apparent density according to existing standards.

Fig. 4 presents a comparison of the apparent density of the semi-finished preforms for PTFE-based composite materials with different contents of carbon fiber filler and different pressing schemes.

As can be seen from Fig. 4, the apparent density of workpieces of PTFE-based composite materials obtained by the traditional method is less and decreases faster as the filler content increases in comparison with the proposed workpieces' pressing schemes. Despite the continued decrease in density with increasing filler content, schemes of pressing using the semi-finished preform allow material characteristics to be more predictable, without drastic changes in apparent density with the increase of filler content from 20 to 30% of the mass.

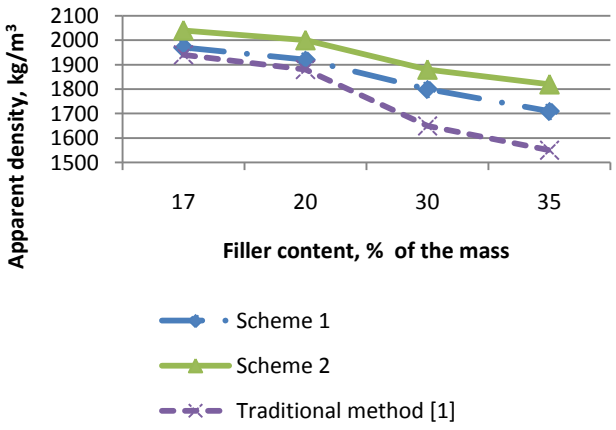


Fig. 4 *- Dependence of the apparent density of workpieces of PTFE-based composite materials on the pressing method and the filler content*

We've also considered the effect of the proposed pressing schemes on the apparent density of PTFE-based composite materials after heat treatment. Fig. 5 shows that the apparent density of the finished PTFE-based composite materials is less than the apparent density of the workpieces they were made from. However, the number of pores in products obtained using the intermediate pressing operation is still less than when using pressing technology in accordance with the requirements of the existing technical regulations. Moreover, with an increase in the filler content in the composite over 20% of the mass. the operation has an even greater positive effect on the creation of a defect-free internal structure of products than with a small amount of filler.

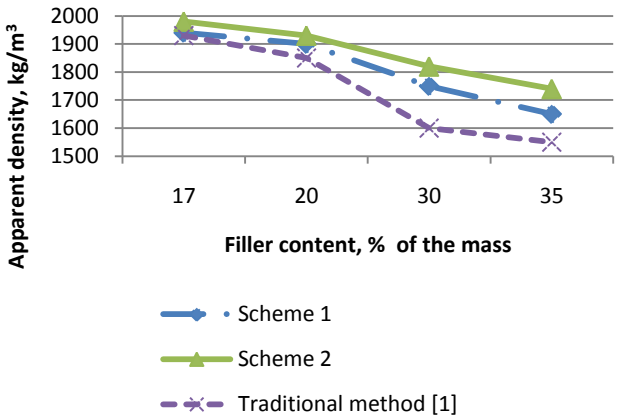


Fig. 5 *- Dependence of the apparent density of finished PTFE-based composite materials on the pressing method and filler content*

It is also curious to note that the dependence of the apparent density of workpieces of PTFE-based composite materials on the pressing method and the filler content (Fig. 4) is practically equal the graphs presented in Fig. 5.

5. Cunclusion

Summarizing, we can conclude that pressing workpieces of PTFE-based composite materials using a semi-finished preform (Fig. 1) allow us to obtain products with a higher apparent density in comparison with the traditional method of pressing. This indicates a decrease in the number of pores and, as a consequence, defectiveness in products made of composite materials based on PTFE when using the intermediate pressing operation.

The developed pressing methods lead to the increase of the contact area between the polymer and individual filler particles and thereby enable the use of coarse fraction carbon fiber as a filler. Consequently it becomes possible to realize a high tensile strength innate to carbon fiber. At the same time, preliminary tests show that the tensile strength of the PTFE-based composite materials filled with discrete carbon fibers demonstrates the potential to achieve the tensile strength of the matrix material even with a filler content of 30% by weight, which is impossible under existing technical regulations. The compressive strength at 10% deformation of such materials reaches values from 45 to 50 MPa. The wear rate of PTFE-based composite materials obtained by pressing through the use of a semi-finished preform is also relatively low and ranges from 1.0 to 2.5 × 10^{-7} mm^3 / N×m.

In addition, the proposed pressing scheme (scheme 2 in Fig. 1) is energy-saving, since drying is not required during the heat treatment of preforms, and the exposure time of the semi-finished preform at a temperature of 150-200 C° is significantly less than the duration of the drying stage in the traditional scheme of sintering workpieces.

Pressing schemes (Fig. 1) are easy to implement and do not require special equipment or expensive additional tooling. Their implementation the by enterprises engaged in the manufacturing of PTFE-based composite materials can be carried out without significant costs and give tangible competitive advantages to both the enterprises themselves and their consumers as well.

6. References

1. Sirenko G.A. Anfrictional carboplastics, Kiev, Tekhnika, 1985 (Sirenko, G.A.).
2. Avdeychik S.V. Engineering fluorocomposites: structure, technology, application, Grodno, GrSU, 2012, (Avdeychik S.V., V.V. Voropaev, A.A. Skaskevich, V.A. Struk).

3. Voropaev V.V. Technology of high filled fluorocomposites – Science and Innovations, Vol. 5, 2009, pp. 48-49.
4. Voropaev V.V. Development of compositions and technology of nanocomposite tribotechnical materials based on polymer-oligomeric fluorine-containing matrixes: Synopsis of Doctoral (candidate of tech sciences) dissertation research, Minsk, BelSTU, 2014 (Voropaev, V.V.).
5. Shelestova V.A., in: International conference on low-temperature plasma physics PLTP-2001, Petrozavodsk, July 1-7, 2001, pp. 226-230 (Shelestova, V.A., P.N. Grakovich, V.V. Serafimovich, K.J. Choy).
6. Voropaev V.V. A technology of high wear- and stress-resistant PTFE-based composites production – Proceedings of the National Academy of Sciences of Belarus (Physical-Technical Series), Vol. 1, 2014, pp. 51-59 (Voropaev, V.V., S.V. Avdeychik, V.A. Struk).
7. Mashkov Y.K. The influence of the energy of ultrasonic vibrations on the structure and properties of polymer composite materials – Material Science, Vol. 3, 2013, pp. 42-45 (Mashkov, Y.K., E.N. Eryomin, D.A. Negrov).

QUALITY MANAGEMENT OF NEW CERAMIC MATERIALS BY USING STATISTICAL EXPERIMENTAL DATA PROCESSING PROGRAMS

Sadenova M. Ph.D., M.Ec. Utegenova M., Anuarbekov T.
Priority Department Centre «Veritas», D. Serikbayev East Kazakhstan State Technical University, Ust-Kamenogorsk, Kazakhstan
MSadenova@ektu.kz

Abstract: *In this paper, we consider the theoretical foundations of the synthesis of ceramic materials from natural aluminosilicates with the addition of technogenic materials (lead and copper slag) using powder metallurgy methods. The characteristics of the feedstock, properties are presented, the geographical deposits of natural components are shown. The possibility of obtaining pelletized, granular, and block ceramic materials based on natural and technogenic sorbents of Kazakhstan is shown by powder metallurgy methods.*

Keywords: CERAMICS, SYNTHESIS, WASTE, ALUMINOSILICATES, STRENGTH

1. Premises and Means of Solving the Problem

Currently, high-quality ceramic materials for various purposes based on unconventional substandard and / or technogenic raw materials are produced in a limited assortment. The fundamental limitations of the widespread use of natural raw materials and industrial materials for the synthesis of various new materials are attributed by specialists to their heterogeneous chemical and phase composition, the presence of impurities (compounds of iron, manganese, chromium, titanium, gold, silver, etc.) and the absence of an economic processing strategy.

Technogenic waste also has a complex composition, depending on the nature of the production process during which it is generated, and is mainly used in the construction or road industries as fillers in the form of dry mixes or as a binder and others [1,2]. Work on the secondary involvement of technogenic materials over the past 15 years has been carried out worldwide. At present, in some CIS countries, the production of ceramic products from natural clays and metallurgical waste in the form of facing slabs is mainly [3]. The joint use of these types of raw materials for the production of ceramic products based on them is practically not studied.

Kazakhstan has explored more than 100 different deposits of natural materials suitable for the synthesis of ceramic materials. The largest are presented in Figure 1. Their geographical location in the country is shown. These are 6 zeolite deposits - Taizuzgen, Chankanai, Sary-Ozek, Yuzhnoye, Daubabinskoye, Kyzyl-Adyr. Deposits of bentonite clays: Chardarya, Karagiye Depressions, Kushmurunskoe, Verkhne-Ubaganskoe, Andreevskoe, Taganskoe.



Fig.1 *Map of Kazakhstan's zeolite and bentonite deposits*

Many industrial industrial wastes (metallurgical slag) are close in their composition and properties to natural raw materials, so the use of industrial waste can cover up to 40% of the construction needs for raw materials. The use of industrial waste can reduce the cost of manufacturing building materials by 10-30% compared with their production from natural raw materials.

Recently, the unique chemical properties of metallurgical slag [4] have attracted attention to the production of materials for use in the environment for use as adsorbents, catalysts, or a source of active substances in environmental engineering.

2. Solution to the Problem

The development of new ceramic materials is material-intensive; therefore, the use of statistical programs for processing experimental data is an important tool for quality management. The use of software products allows us to reduce the number of practical experiments on the synthesis of ceramics and determine the optimal parameters for the synthesis of ceramics of their natural and technogenic raw materials to obtain materials with desired properties.

In this work, natural aluminosilicates in the form of zeolites and bentonite, industrial materials of metallurgical enterprises of Kazakhstan (slag of lead and copper production) were used as objects of study.

The involvement of natural and man-made raw materials should be preceded by studies of the composition of the material, structure and properties. A physical and chemical study made it possible to obtain information on the material filling of the samples, to trace the sequence of thermal degradations and to determine the composition of volatile components. It was established that the matrix of synthesized materials is formed from clay, and the aggregate from finely dispersed technogenic raw materials. Such a matrix structure has high strength. Based on the data of X-RAY phase and differential thermal analyzes, the stability regions of the studied samples during heat treatment are determined, which made it possible to synthesize materials with desired characteristics.

The production of ceramic products from natural and man-made raw materials is possible subject to preliminary fine grinding [5]. Therefore, the synthesis of ceramic materials was performed on the basis of the classical methods of powder metallurgy, in which molding compounds were prepared from the starting substances in the form of powders, which were then extruded and / or pressed with thermal training at each stage.

A technological scheme has been developed that reflects the logical sequence of work (Figure 2), starting with the preparation of the starting materials and ending with the receipt of new materials from natural and man-made materials.

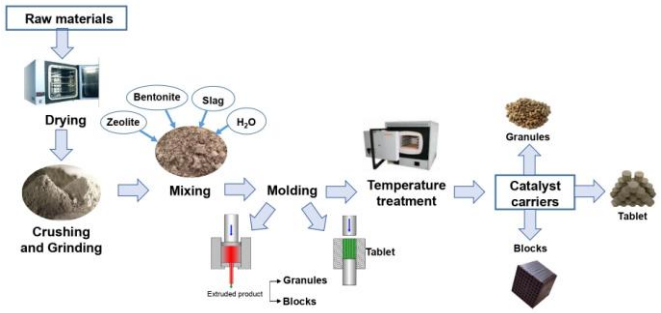


Fig.2 *The technological scheme of the synthesis of ceramic catalyst supports*

In the process of ceramic synthesis, to obtain products with desired properties, it is necessary to select the composition of the molding mixture. Such work involves the implementation of a large volume of experiments with obtaining a significant amount of experimental data requiring systematization. An important tool for managing the quality of synthesized new ceramic materials is the use of statistical programs for processing experimental data, for example, Statistica, Statgraphics, and others [6]. The use of software products allows us to reduce the number of practical experiments on the synthesis of ceramics and determine the optimal parameters for the synthesis of ceramics of their natural and technogenic raw materials to obtain materials with desired properties.

Statistical programs evaluate simultaneously the impact of several factors on the final required function. In our case, the controlled factor was the value of the mechanical strength of the synthesized ceramic samples. Influencing factors are the composition of the mixture, the dispersion of the components of the mixture, humidity, calcination temperature, the magnitude of the load during pressing, the design of technological equipment and others.

3. Results and discussion

In ceramic technology, three methods of forming products are used: from plastic masses, semi-dry pressing, and slip casting. The method of mass preparation also depends on this: for plastic molding, plastic masses with a moisture content of 18-22% are prepared, for semi-dry pressing masses with a moisture content of 6-9% are prepared, and for slip molding, with a humidity of 45-55%.

The masses are selected according to the mineralogical composition, setting the required ratio of clay, quartz, feldspars and other additives. Mass preparation is carried out more often by the weighted dosage of the components according to the approved recipe. It gives a more accurate ratio than volumetric.

The synthesis and heat treatment conditions of the contacts were maintained the same; only the composition varied. The natural zeolites of the Chankanai (Ch), Sary-Ozek (C) and Taizhuzgen (T) deposits, as well as the bentonite of the Tagansky deposit, were selected as natural raw materials. Zeolites and bentonite clays have a similar chemical composition, are represented by aluminosilicates containing oxides of alkali and alkaline earth metals. Bentonite was used as a binder component. When varying the composition of the experimental batch of natural and technogenic raw materials, the following markings were used: when copper slag was added, the "Cu" index was assigned, for example, T_{Cu}, Ch_{Cu} and S_{Cu}, and when the lead slag was added, the "Pb" index (Table 1).

Table 1: *Marking of samples from natural and technogenic materials*

1	Taizhuzgen zeolite + bentonite + lead slag	T_{Pb}
2	Taizhuzgen zeolite + bentonite + copper slag	T_{Cu}
3	Sary Ozek zeolite + bentonite + lead slag	C_{Pb}
4	Sary Ozek zeolite + bentonite + copper slag	C_{Cu}
5	Chankanai zeolite + bentonite + lead slag	$Ч_{Pb}$
6	Chankanai zeolite + bentonite + copper slag	$Ч_{Cu}$

The manufacture of granular materials includes the stages of preparation of the initial mixture, its extrusion in the form of granules and sintering. A plastic mass suitable for this method must have certain structural and mechanical properties, due to which it becomes less viscous, acquires plasticity and can be forced through a matrix. Under the influence of mechanical stresses, the plastic strength decreases, and after the release and release of stress, its thixotropic recovery occurs. The mixture was prepared of various composition and wetin the range up to 20 mass. % (wet = 15 wt.%; 17.5 wt.% and 20 wt.%). The prepared mass, satisfying the plasticity requirements, was pressed through the matrix with the formation of extrudates with a diameter of 2.5, 4, 6 mm, depending on the size of the matrix used. The obtained granules were dried and calcined in a muffle furnace at a temperature from room temperature to 500 °C, 750 °C and 1000 °C.

Statistical processing of experimental data on the influence of the composition of the molding material on the mechanical strength of the synthesized ceramic was performed. The results of the study, obtained by varying the nature of the zeolite, humidity in the composition of the press mass and the calcination temperature of the finished samples, processed using the Statistica program, are graphically presented in Figures 3-5.

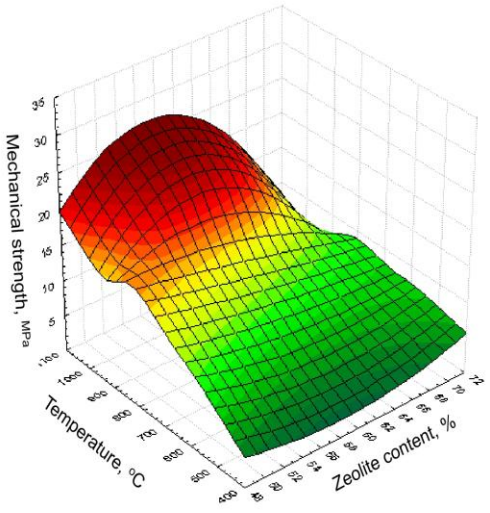


Fig.3 *The dependence of the mechanical strength of the catalyst carrier on the zeolite content and temperature treatment (Wet = 15 %)*

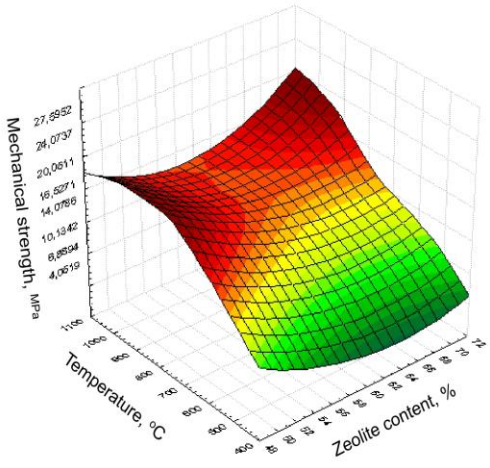


Fig.4 *The dependence of the mechanical strength of the catalyst carrier on the zeolite content and temperature treatment (Wet = 17.5 %)*

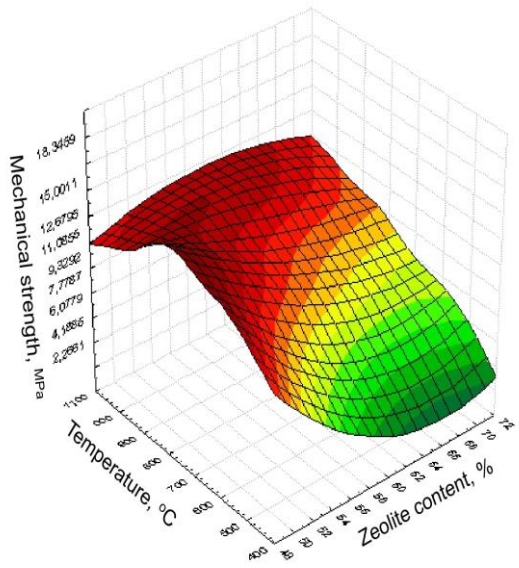


Fig.5 *The dependence of the mechanical strength of the catalyst carrier on the zeolite content and temperature treatment (Wet = 20 %)*

According to the data obtained, the optimum moisture content of the press powders was determined. It was found that an increase in pressing pressure and annealing temperature lead to an increase in the value of mechanical strength. Wet, providing the necessary strength, should be within 17.5%. At low temperatures, shrinkage of poorly calcined particles occurs, due to which the strength properties deteriorate. An increase in the temperature treatment from 500 to 750 °C in the manufacture of a catalyst carrier contributes to an increase in its strength.

Using the Statgraphics graphical editor (Figure 6), we studied the effect of pressing pressure on the mechanical strength of the samples.

As can be seen in Figure 6, with a change in wet from 15% to 17.5%, an increase in the mechanical strength index with an increase in temperature is observed for a composition containing 60% zeolite. With a further increase wet up to 20% in samples containing 60 and 70% zeolite with an increase in sintering temperature, an increase in mechanical strength is observed. While at a zeolite content of about 50%, a decrease in strength occurs. Thus, ceramics containing 60% zeolite with the addition of 40% bentonite clay are recommended as the material for the catalyst carrier. The results are explained by the fact that zeolite particles, having a porous structure and surface, contacting each other in the bulk of the material form a rigid reinforcing structure, and bentonite, possessing astringent properties, increases the strength of the product. A change in this structure leads to a decrease in the strength of the material.

It is impossible to assess the prospects for using natural aluminosilicates and metallurgical slags for the manufacture of gas purification catalyst carriers without a preliminary study of the structural and mechanical properties. Therefore, according to the results of experimental studies, the optimal charge compositions based on a zeolite-bentonite mixture with the addition of technogenic raw materials to obtain ceramic materials with a matrix structure (wt.%) With a ratio of components of 60:20:20, respectively, were determined.

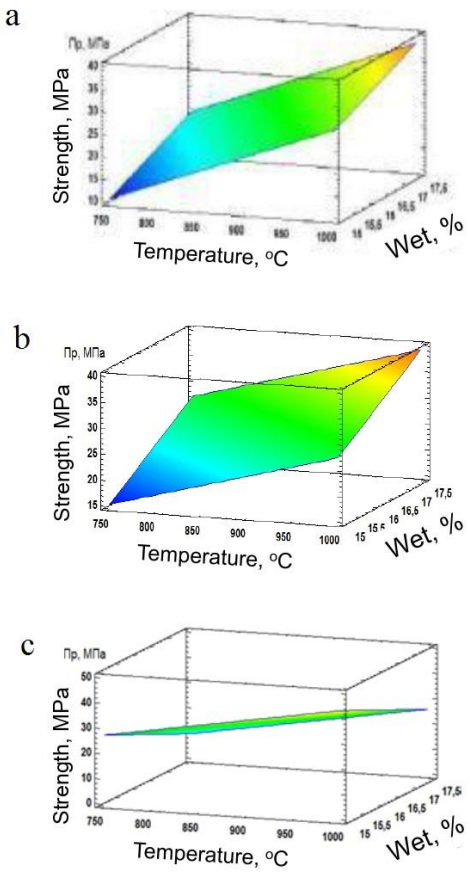


Fig.6 *The effect of temperature treatment and wet on the mechanical strength of the catalyst carrier depending on the zeolite content:*
а – Zeolite:Bentonote = 50:50; б – Zeolite:Bentonote = 60 : 40;
в – Zeolite:Bentonote = 70 : 30

Figures 7-9 show the research data on the strength of ceramic catalyst carrier depending on the composition of the charge and the calcination temperature. To determine the mechanical strength, a batch of samples was prepared from zeolite: bentonite: slag mixture in a ratio of 60:20:20 (Z: B: S (Cu) and Z: B: S (Pb)).

Among the series of samples with the addition of copper slag with various zeolites, the composition based on Taizuzgen zeolite has the highest strength. It should be noted that at a heating temperature of 500 °C the strength of the sample with the Taizhuzgen zeolite is the same with Sary-Ozek and Chankanai (15-17 MPa). At an annealing temperature of 750 °C, the indicator for all three samples increased. An increase in temperature to 1,000 °C led to a twofold increase in the strength value for the sample with Taizuzgen zeolite (T_{Cu}) and amounted to 54 MPa, while for Ch_{Cu} and S_{Cu}, the strengths were 25.4 and 28, respectively. The smallest strength after heat treatment was observed for a sample of the Chankanai deposit synthesized with zeolite.

The introduction of a lead plant slag instead of a copper plant slag into the composition of the charge significantly affected the properties of the synthesized materials. In this case, the maximum value of mechanical strength at 1000 °C is also observed for samples based on the Sary-Ozek zeolite (S_{Pb} = 55.4 MPa), and for T_{Pb} and Ch_{Pb} 32.4 and 49.7, respectively.

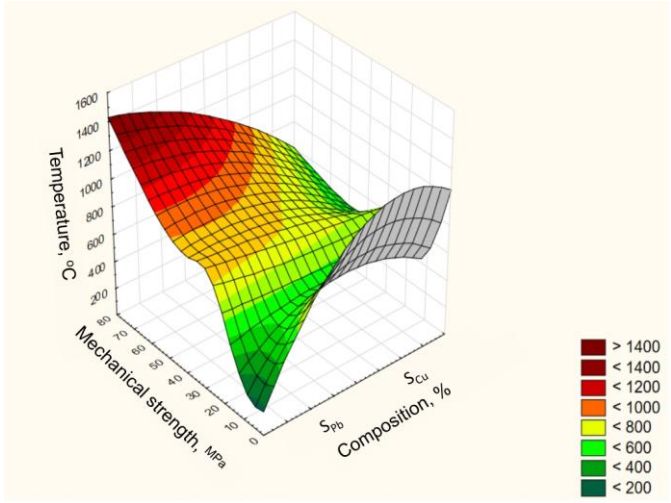


Fig.7 *The dependence of the mechanical strength of the catalyst carrier on the composition and sintering temperature (composition of the Sary-Ozek Zeolite + Bentonite + Slag)*

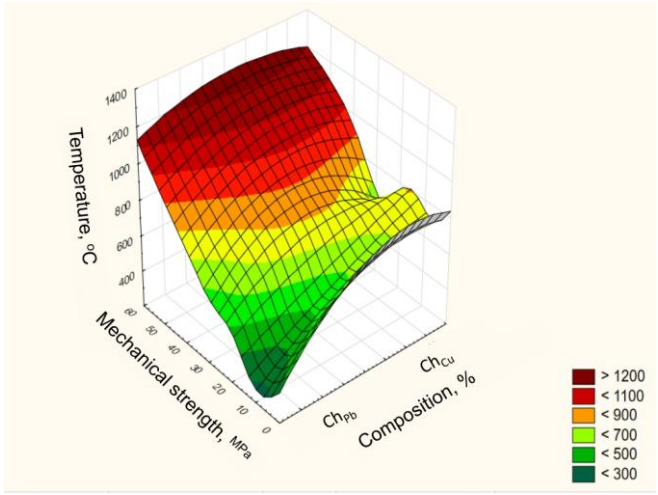


Fig.8 *The dependence of the mechanical strength of the catalyst carrier on the composition and sintering temperature (composition of the Chankanai Zeolite + Bentonite + Slag)*

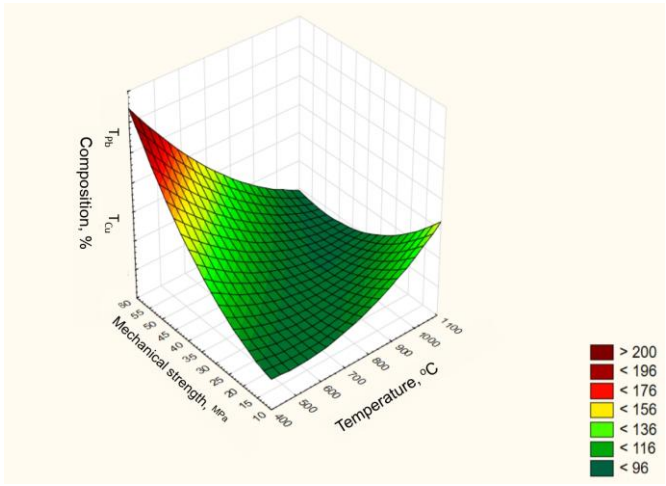


Fig.9 *The dependence of the mechanical strength of the catalyst carrier on the composition and sintering temperature (composition of the Taizhuzgen Zeolite + Bentonite + Slag)*

It is shown that the mechanical strength of the samples synthesized under the same conditions by varying the nature of the zeolite and slag is quite high. It should be noted that high-temperature training of samples up to 1000 °C contributes to an increase in strength. According to the data obtained, it was determined that the optimum value of mechanical strength is observed for the sample obtained by mixing bentonite slag with the zeolite of the Taizhuzgen deposit and is more than 30 MPa, which corresponds to the requirements for catalyst supports.

4. Conclusion

The synthesis of ceramic materials was performed on the basis of the classical methods of powder metallurgy, in which molding compounds were prepared from the starting substances in the form of powders, which were then extruded and / or pressed with thermal training at each stage. Previously, the components of the mixture were subjected to fine grinding to a fraction of 0.01 mm to obtain a homogeneous mixture. The initial charge components — natural zeolite and bentonite - were mixed with technogenic products represented by slag or dust in proportions of 60:20:20, respectively.

An important characteristic of the charge is the moisture capacity of the starting components and the resulting mixture. The moisture content was varied in the range of 15 ÷ 20% to ensure the required molding moisture and satisfactory ductility. After mixing, the prepared mixture was sent to molding by compression in the form of tablets or by extrusion in the form of granules. The resulting materials were kept in air, and then subjected to heat treatment in a muffle electric furnace in the temperature range 500–1000 °C.

The compositions and properties of the feedstock and ceramic materials synthesized based on them were studied. The results obtained are a prerequisite for creating a technology for the synthesis of new ceramic materials from a mixture of natural and technogenic raw materials.

A batch of synthesized samples was tested in catalytic oxidation reactions of methane and / or carbon monoxide. It was found that all synthesized contacts provide catalytic activity in the reactions of oxidative catalysis of carbon-containing toxic components and can become basic models for which, by improving the preparation method, it is possible to develop a technology for the synthesis of ceramic materials for use in environmental catalysis.

References

1. Makarov D.V., Melkonyan R.G., Suvorova O.V., Kumarova V.A., Prospects for Using Industrial Waste in Production of Ceramic Building Materials, Gornyy informatsionno-analiticheskiy byulleten, 2016, N. 5, 254–281 (In Russian).

2. Gurieva V.A., Magnesium-Containing Technogenic Raw Material in The Production of Structural Ceramic Materials, Bulletin of the South Ural State University, Series “Construction Engineering and Architecture”, 2013, V. 13, N.1, 45-48 (In Russian).

3. Kauchur A., Sheleh V., Kauchur S., Hrachanikau1 A., Manak P., Zakharenka A. Development of terracot ceramic tiles manufacturing technology with use of technogenic products of energy complex, Chemical Technology and Ecology, 2017, V.2, 86-94 (In Russian).

4. Montoya-Bautista C.V., Avella E., Ramírez-Zamora R.M., Schouwenaars R., MetallurgicalWastes Employed as Catalysts and Photocatalysts for Water Treatment: A Review. Sustainability, 2019, V.11, 1-16.

5. Naito M., Shinohara N., Uematsu K., Handbook of Advanced Ceramics, V.1: Materials Science, Chapter 2.1 Raw Materials, 2003, Elsevier Inc.

6. StatSoft Russia, 2018, STATISTICA Base <http://www.dataanalysis.ru/products/STATISTICA_Base/> accessed 10.02.2019 (in Russian).